Development of a Blast and Fire-Resistant Structural Tunnel Liner

FINAL PROJECT REPORT

By
Clay Naito
Email: cjn3@lehigh.edu
Lehigh University

Fengtao Bai, Spencer Quiel, Zheda Zhu, Aerik Carlton, Qi Guo

Lehigh University

April 2020

Disclaimer

The contents of this report reflect the views of the authors, who are responsible for the facts and the accuracy of the information presented herein. This document is disseminated in the interest of information exchange. The report is funded, partially or entirely, by a grant from the U.S. Department of Transportation's University Transportation Centers Program. However, the U.S. Government assumes no liability for the contents or use thereof.

1. Report No.	2. Government Accession No.	3. Recipient's Catalog No.	
4. Title and Subtitle Development of a Blast and Fire-Resistant Structural Tunnel Liner		5. Report Date April 2020	
		6. Performing Organization Code	
7. Author(s) Clay Naito https://orcid.org/0000-0003-3835-8131, Fengtao Bai https://orcid.org/0000-0003-1453-3417, Spencer Quiel https://orcid.org/0000-0002-1316-7059, Zheda Zhu https://orcid.org/0000-0001-5408-3110, Aerik Carlton https://orcid.org/0000-0002-7806-6099, Qi Guo https://orcid.org/0000-0003-2713-9478		8. Performing Organization Report No.	
9. Performing Organization Name and Address University Transportation Center for Underground Transportation Infrastructure (UTC-UTI) Tier 1 University Transportation Center Colorado School of Mines Coolbaugh 308, 1012 14th St., Golden, CO 80401		10. Work Unit No. (TRAIS)	
		11. Contract or Grant No.	
12. Sponsoring Agency Name and Address United States of America Department of Transportation Research and Innovative Technology Administration		13. Type of Report and Period Covered Final Report (Sept. 2016 to Oct. 2018)	
		14. Sponsoring Agency Code	

16. Abstract
A comprehensive study was conducted on the design and performance of concrete tunnel liners subjected to blast and fire events. The effort initiated with a study to assess the impact of fire and blast events on the structural performance of the concrete liner. The effort is divided into three phases. The first phase focuses on the implications of blast events on the tunnel liner. The second phase examines the implications of fire events on the tunnel liner. The third phase consists of a preliminary study on the performance of the concrete liner subject to fire demands. In a contact or near filed blast event, the reflected tensile wave near boundaries is the primary reason for concrete spallation damage. Appropriate concrete model (RHT model) can be selected in finite element software LS-DYNA to simulate the behavior of concrete slab as well as concrete tunnel lining subjected to blast. The spalling of supported tunnel model is alleviated via changing the property of backfill. By increasing the backfill impedance, the tensile stress in concrete will gradually become compression thus reducing the amount of damage to the concrete substrate. The numerical study shows that the damage to tunnel liners will be localized and do not represent a significant threat to concrete lined tunnels. Experimental testing would be of use to validate the numerical results. Due to the fact that the benefits gained through modification of the substrate are minimal, the cost implications of substrate modification are high, and that minimal performance improvements will be achieved for a low likelihood threat, the blast testing is not recommended. The numerical tool for fire evaluation is discussed. The model consists of a confined discretized solid flame and is verified in comparison to computational fluid dynamic numerical results which were calibrated from experimental tests. The model indicates significant thermal exposure of the tunnel surface due to fire events. To address this threat a fire testing simulation fixture was developed. The experimental setup for the fire effects is presented and preliminary test results are provided showing spall and fire induced damage to tunnel liners.

17. Key Words Explosion, Blast, Concrete, Fire, Tunnel, Design		18. Distribution Statement No restrictions.	
19. Security Classification (of this report) Unclassified	20. Security Classification (of this page) Unclassified	21. No of Pages 99	22. Price NA

Table of Contents

List of Figures

List of Tables

List of Abbreviations

CHPP: Center of Highway Pavement Preservation

MDOT: Michigan Department of Transportation

CDSF: Confined Discretized Solid Flame

Executive Summary

A comprehensive study was conducted on the design and performance of concrete tunnel liners subjected to blast and fire events. The effort initiated with a study to assess the impact of fire and blast events on the structural performance of the concrete liner. The effort is divided into three phases. The first phase focuses on the implications of blast events on the tunnel liner. The second phase examines the implications of fire events on the tunnel liner. The third phase consists of a preliminary study on the performance of the concrete liner subject to fire demands.

Safety of tunnels is critical to an area and this study focus on predicting, analyzing and mitigating the tunnel lining damage from blast events. The tunnel lining blast damage is firstly categorized into flexural damage and near field spall damage. The damage specifically encountered in tunnel linings, concrete on subgrades at near field, is studied through both analytical solutions and high-fidelity numerical modeling. Numerical models are compared with analytical solutions and validated against representative blast testing results. It is finally concluded that tunnel lining damage shares some common features with other concrete structures however it is unique in the shock propagation properties. If the backfill properties are properly engineered, lining damage can be significantly reduced.

Other than concrete damage caused by blast hazard in tunnels, spall damage on concrete tunnel linings due to severe fire needs to be evaluated accurately and rapidly for comprehensive and stochastic examination of the resilience of underground transportation infrastructure to extreme loads. The damage evaluation should be based on the determination of the heat exposure on the tunnel linings caused by vehicle fires. An intermediate model that is capable of rapid and reliable heat flux assessment for vehicular fires in road tunnels is developed and compared to design fire curves and numerical models. The developed model consists of a confined discretized solid flame (CDSF) which accounts for both radiation and convection based on semi-empirical and first principles relationships as well as calibration with high-fidelity models. The CDSF approach shows strong agreement with computational solutions performed with NIST's Fire Dynamics Simulator (FDS) for three magnitudes of fire scenarios in a prototype tunnel. The potential for fire-induced concrete spalling of the tunnel liner is predicted based on the thermal exposure calculated from the CDSF model, which is spatially mapped to the exposed face of the liner with a time history that realistically represents the duration of the design fire scenarios.

The performance of the concrete to fire demands was examined through the development of a fire exposure test setup. The design of the setup and preliminary results are provided.

Findings

In a contact or near filed blast event, the reflected tensile wave near boundaries is the primary reason for concrete spallation damage. Appropriate concrete model (RHT model) can be selected in finite element software LS-DYNA to simulate the behavior of concrete slab as well as concrete tunnel lining subjected to blast. The spalling of supported tunnel model is alleviated via changing the property of backfill. By increasing the backfill impedance, the tensile stress in concrete will gradually become compression thus reducing the amount of damage to the concrete substrate.

The accuracy of the CDSF model is verified in comparison to CFD results which were calibrated from experimental tests. The model indicates significant thermal exposure of the tunnel surface due to fire events. The experimental setup for the fire effects has been developed and preliminary testing has been completed.

Chapter 1: Project Scope

The Lehigh University task 1 research effort was conducted in year 1 and 2 of the University Transportation Center on Underground Transportation Infrastructure. The focus of Task 1 is to examine the design and performance of concrete tunnel liners subject to fire and blast demands. The study consists of a literature review of blast and fire-resistant tunnel systems and examination of the existing case studies on past events. The scope of demands to be considered are determined through preliminary analytical evaluations of a set of tunnel types subject to a range of demands (i.e., small/large Improvised explosive device, vehicle fire / fuel transport vehicle fire). Preliminary designs developed based on first principles and current state of the art is numerically evaluated under the range of load expected. Numerical models are verified using case study data. The performance is examined using parametric evaluations. Preliminary experimental investigation of the prototype liner is conducted to verify resistance to close in fire exposure. A testing setup is developed and experiments are carried out at Lehigh University.

Chapter 2: Tunnel Damage Due to Blast and Fire Events

Tunnel Lining Damage Caused by Blast Hazards

Tunnels as critical infrastructures face catastrophic threats such as blast. Blast in tunnels has been recognized as a reoccurring event. Blast events may either be intentional or accidental. No matter the nature of the blast events, the consequences is devastating and infrastructure and local economy can be heavily jeopardized. This is especially true for tunnels since it is unlikely that there is an alternative route nearby. In addition, the repair and retrofit of a blast damaged tunnel might be very difficult since the damage is hard to detect and repair (spallation typically occurs on the back of the tunnel linings where they are invisible from the front). As a result, the resistance and resilience of tunnels is a very important topic.

Intentional blasts target tunnels where human traffic is heavy, mostly subway tunnels, to cause maximum personnel loss whereas unintentional blast events are more likely to occur on the road tunnels where vehicle traffic is heavy or tunnels that are under construction. Flammable substances trapped in tunnels during heavy traffic considerably increase the risk of explosion, because under these conditions accidents that can easily trigger explosion such as collisions and vehicles overheating are more likely to happen. Similarly, the tunnels under construction are also more vulnerable since explosives for rock blasting and natural gas inside of underground pockets may be present. In case of unintentional blast events, the amount of explosives can be considerably large and might be carried by heavy vehicles. For example, in Niigata, Japan a tunnel under construction exploded and killed four construction workers in May 24 of 2012 (The Japan Times NEWS 2012). Also, the Ba-Mian-Shan (Eight Face Mountain) tunnel accident in Hunan Province, China on May 19, 2012 where a construction truck loaded with 12 cases (24 kilogram each) of explosives for rock blasting was accidentally ignited during unloading. Twenty workers were killed and four more were injured. On October 2015, a truck that was loaded with flammable paint exploded after hitting the curb inside the Sangju tunnel at South Korean Central Inland Expressway near Changwon, South Korea. This accident injured 21 people and set other 11 vehicles on fire (Yonhap News Agency 2017). Most recently, the Fu-tu-yu no. 5 tunnel explosion in He Bei Province, China was triggered by a semi-truck loaded with unstable chemical trapped in heavy traffic in May 23rd of 2017. This catastrophic explosion killed 12 people and injured three more (Bjnews 2017). The intentional tunnel blast events target on people and the carriers, and the explosives are often carried by people. As a result, the amount of explosive is limited and the damage can rarely reach the major structural components. On the other hand, the intentional blast attacks are also devastating. On July 7th of 2005, the London subway bombing attack killed 52 and injured more than 700 by a homemade organic peroxide based explosive device hided in the backpack (Jr and Sciolino 2005). On March 29th 2010, two stations of Moscow Metro system were attacked by bombs and at least 40 people were killed and over 100 were injured (Aydar 2010). More recently, on April 3rd 2017, Saint Petersburg Metro was attacked by an explosive (reported between 200 grams to 300 grams) packed in a briefcase, and 15 people were killed and more than 45 were injured(Jansen 2017).

The accidental blast events in road tunnels are catastrophic, the lining may suffer from substantial damage. Figure 1 shows the tunnel lining damage after the Fu-tu-yu explosion. As seen in Figure 1, the tunnel lining has a clear breach area of 0.25 m^2 on the roof. The cracks indicating structural

integrity loss are clearly shown. This paper will analyze the cause of those damage areas as well as making suggestions on the retrofit measures.

Figure 1: Tunnel lining blast damage(Bjnews 2017)
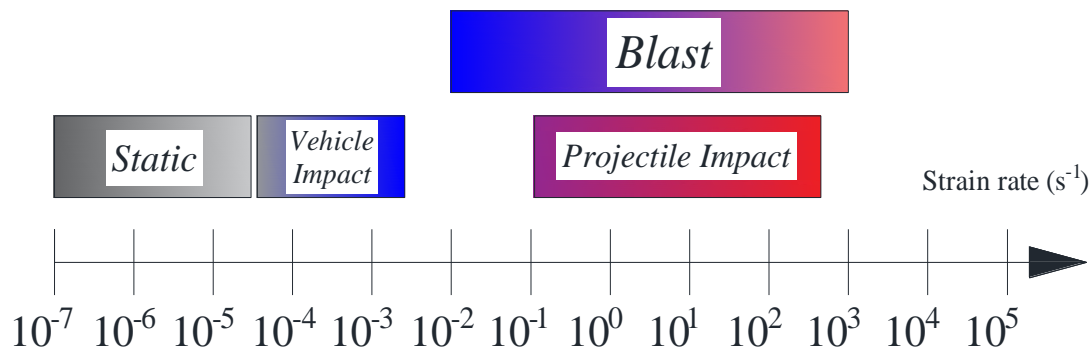
Figure 2: Loading rate range (Ekström 2015)

Tunnel construction is very expensive with cost increase as the tunnel diameter increases. Therefore, space in tunnels is often limited due to the high cost of tunneling construction. In the limited space, blast events are likely to be categorized as near field and local spallation and breach damage on the tunnel linings may be dominant instead of flexural damage.

Concrete spallation damage under blast loads requires knowledge in different fields. First, the localized spall and breach damage is caused by stress waves that propagate and reflect within concrete at a very high speed. Blast waves directly load concrete linings with compressive stress waves. However, some of the compressive waves can be reflected at the boundary of the tunnel linings and the reflected waves can become tensile depending on the wave impedance of the backfill materials.

The first portion of this study focuses on the damage of tunnel linings from blast loading and investigates the key role of backfill properties from stress wave propagation perspective. The spalling mechanism concrete slab subjected to blast is first studied with finite element method. The influence of a vital parameter, wave impedance, is identified and quantified. Then, the tunnel

model is constructed to study specific tunnel lining behavior in blast with varying backfill properties.

Tunnel Lining Damage Caused by Fire Hazards

Tunnels are vitally important to the transportation of goods and people by providing efficient passage through difficult terrain and under waterways and urban areas. According to the *Tunnel Operation, Maintenance, Inspection, and Evaluation (TOMIE) Manual* (Bergeson and Ernst 2015), an initial tunnel inventory has been conducted by both the Federal Highway Administration (FHWA) and the Federal Transit Administration (FTA). The inventory identified more than 350 highway tunnels in the United States, in which 40% of them exceed 50 years of service. While a tunnel is generally not the preferred form of transportation structure due to high economic costs and construction time, it several advantages over above ground transportation structures such as improved earthquake resistance (Kolymbas 2005), shorter routes under topography or waterways, and benefits to urban planning by passing under dense urban environments. With the continued improvements in tunnel boring technology, further expansion of U.S. tunnel networks is expected.

The large amount of traffic going through a tunnel with combustible materials such as vehicle fuel and flammable cargo poses threats to the fire safety of the tunnel structures. Flame energy and hot gases generated from the vehicle fires in the confined tunnel environment can induce severe damage to the tunnel, which will ultimately lead to significant economic losses due to repair and disruption of tunnel functionality. Currently the most common material for tunnel liners is reinforced concrete, which could be in the form of precast concrete segments, cast-in-place concrete, or shotcrete. Concrete has been long regarded for its inherent fire resistance due to its low thermal conductivity, high thermal capacity, and high cross-sectional mass. However, exposure to elevated temperature will result in concrete strength reduction both during heating and in its residual post-fire condition. Fire-induced spalling is also a major concern because of concrete's sensitivity to changes in moisture and the magnitude of internal stress developed in the hydrated material because of pore pressure increases and variations in thermal expansion (Figure 3).
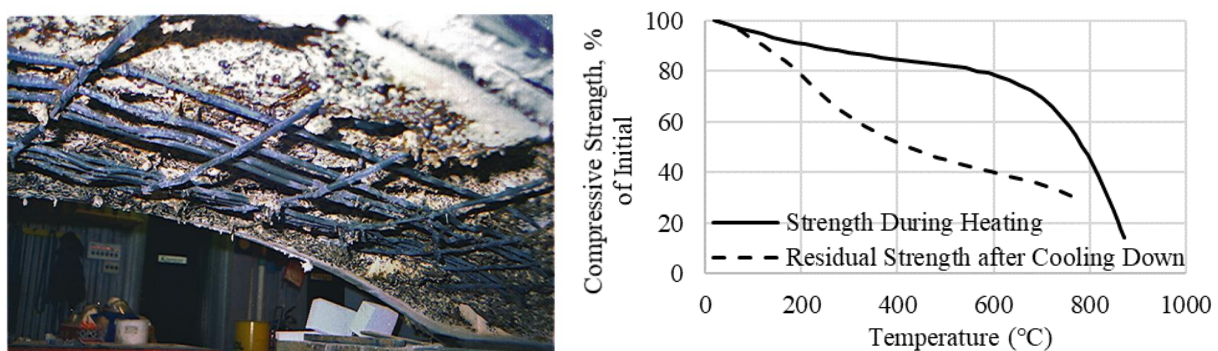
Figure 3: Typical concrete damage after heat exposure: spalling (Jansson 2013) (left) and strength reduction (ACI 2014) (right)

Roadway tunnels have an extensive history of fire events that have resulted in damage of structural components and significant repair costs. For example, a severe fire from a 2008 cargo train accident inside the Channel Tunnel between the UK and France inflicted damage over a 750-m length of the concrete tunnel lining (Branch 2010). According to the technical investigation of that

event, the concrete liner spalled to various depths and breached through the section at some locations. This ultimately led to a reduction of the structure's load bearing capacity and increased the risk of progressive collapse. The fire event was followed by 5 months of repair at an estimated cost of $70 million (in 2008 US dollars). Also, a 1991 heavy goods vehicle (HGV) fire within the Mont Blanc Tunnel connecting France and Italy (Duffe and Marec 1999) and a tanker truck fire in the Caldecott Tunnel between Oakland and Orinda in California, USA (Egilsrud 1984) resulted in multiple casualties and structural damage that required several months of repair.

To evaluate the resilience of tunnel liners to damage resulting from fire events, engineers must first calculate the fire-induced heat exposure and then determine the structural effects due to heat transfer. There are generally three types of fire models for thermal exposure evaluation: parametric standard fire curves, computational fluid dynamics (CFD) models, and semi-empirical models of varying complexity. In practice, a parametric fire curve is often used for its simplicity. A great deal of experimental work has been done to obtain temperature time histories for potential types and sizes of fire in tunnels, among which the Rijkswaterstaat (RWS) time-temperature curve is one of the most widely adopted standards worldwide. In the US, the National Fire Protection Association (NFPA) defines fire protection performance criteria for tunnels based on the RWS curve (Association 2011). The fire event is represented as an upper-bound temperature time history caused by combustion of a 50-m^3 fuel tanker with a heat release rate (HRR) of 300 MW and duration of 120 min. The temperature rapidly increases to 1200°C in 10 minutes from ignition and remains above 1200°C for 2 hours (Association 2011). While the RWS curve is relatively easy to apply to the tunnel liner as a worst case, it does not consider spatial distribution of heat exposure, which potentially results in overly conservative and inefficient designs. The use of a specified temperature time history circumvents the calculation of realistic heat transfer from the fire to the liner via flame radiation and convection from smoke and hot gases resulting from combustion.

CFD analyses provide high-resolution, data-rich calculations of fire demands within enclosures. However, these models require extensive computing time and a large amount of input, most of which must be assumed if experimental data or design guidance are not available. Such an approach is not feasible for rapid assessment of an inventory of tunnels and/or for a wide range of fire scenarios, nor is it practical for a stochastic assessment of structural resilience with realistically varying material and geotechnical characteristics of the tunnel. As an alternative, zone modeling packages (such as OZone (Cadorin et al. 2002)) and empirical relationships (Hurley 2016) have been developed for compartment fires in buildings and can conservatively account for smoke buildup as well as corner and wall effects inside an enclosed room. For bridges, open-air vehicle-based fires can be represented primarily as sources of intense flame radiation for which a solid flame or other radiation emitting models can be deployed. For example, the authors previously developed a modified discretized solid flame model for open-air fires and the resulting heat transfer calculations for steel-supported bridges (Quiel et al. 2015). These alternative approaches to CFD or standard fire curves represent a so-called "intermediate" complexity class of models, which can offer conservative calculations of spatial distribution with moderate computational effort.

To appropriately model a severe fire in a tunnel environment, the solid flame and zone model concepts can be merged into a single approach that appropriately accounts for flame radiation, smoke effects, and convection from gaseous combustion byproducts. In this paper, an intermediate fire model called the confined discretized solid flame (CDSF) model is used to account for radiative and convective heat flux. The CDSF can provide rapid and reliable predictions of the total heat flux received by tunnel liners from a range of typical vehicle design fires. Calibration of

the CDSF model is performed via comparison to experimentally validated CFD solutions developed via the publicly available Fire Dynamics Simulator (FDS) (McGrattan et al. 2013). The computational efficiency of the CDSF model versus its CFD counterpart enables stochastic assessment of numerous input parameters over an inventory of tunnels. A commercial 3D computer-aided design software, Rhino (Robert McNeel & Associates 2017), and its accompanied visual programming language, Grasshopper (Robert McNeel & Associates 2014), were chosen to implement the CDSF model for their extended capabilities in complex, parametric geometric analysis and visualization.

Summary of Fire and Blast Demands on Concrete Tunnel Liners

Based on the discussion provided in this chapter, two efforts were conducted. A numerical model was developed to examine the response of concrete liners subjected to blast demands. A secondary study was conducted to develop a tool to determine fire demands on tunnel liners. These studies are summarized in the subsequent chapters.

Chapter 3: Literature Review of Concrete Spall Due to Blast and Fire Hazards

Background on Numerical Modeling of Concrete Subject to Blast Effects

This study focuses on the blast performance of concrete slabs, walls and other relatively 'thin' concrete components through a series of tests and corresponding numerical analyses. Note that herein 'thin' represents the structural thickness relative to the blast wave length. Thin is defined in this particular study as a concrete element with thickness to blast wave length less than 0.5. Majority of concrete slabs subjected to near field blast falls into the thin category. For example, in this study, one of the tested cases that will be discussed has a 2.56 lbs TNT equivalent charge and 9 in. standoff. This blast scenario has a scaled distance of 0.55 ft/lb$^{1/3}$ that is largest in the three tested cases (in general, larger scaled distance corresponds to shorter duration) and the resulted blast wave duration is only about 200 μs. Even for this short duration test case, by assuming stress wave speed of 11500 ft/s, the wave length is about 30 inches. For blast events consisting of luggage or small vehicle size charges, the duration is typically in microseconds and the corresponding wave length in concrete is hundreds of inches. The typical slabs like wall panels are just a few inches thick and for example in this study the tested slab is 6 in. thick. Therefore, most structural components can be regarded as thin.

Typical failure modes under blast loads are spalling (ejection of target material on the opposite side of detonation), and breaching (perforation / full penetration). To be consistent with popular literature in blast engineering, spall is defined herein as the fragmentation damage occurs at the opposite side of detonation. Blast regimes can be divided into contact ($Z < 0.053$ m/kg$^{1/3}$ or 0.134 ft/lb$^{1/3}$), near field ($0.053 < Z < 0.4$ m/kg$^{1/3}$ or 1.0 ft/lb$^{1/3}$), medium field ($0.4 < Z < 4.0$ m/kg$^{1/3}$ or 10 ft/lb$^{1/3}$) and far field ($4.0 < Z < 40$ m/kg$^{1/3}$ or 100 ft/lb$^{1/3}$) according to the scaled distance Z. For the medium and far field blast, flexural deformation is the dominant mode of structural component response whereas near field and contact blast will induce localized damage modes such as spalling, breaching and cratering damage.

Concrete blast spalling and breaching damage was primarily studied in the military sector in the United States until last several decades due to increasing concerns from intentional and accidental blast events. A lot of civil structures like schools, office buildings, prisons and government agencies require blast resistant design and analysis. One of the early studies that explored spall damage in blast was composed by McVay. In McVay's report (McVay 1988), reflected tensile wave at the free boundary was identified as the reason for spalling damage and it was stated that once the tensile stress exceeds the dynamic tensile strength spalling occurs. McVay's development was a simplified method based on 1D axial wave propagation and uniaxial tensile strength at the wave propagation direction.

For the past several decades, many studies in concrete blast damage focus both on the experimental studies and numerical modeling. There have been comprehensive experimental studies targeting concrete spallation damage at small scaled distance. Among those studies, Wu (C. Wu, Nurwidayati, and Oehlers 2009) analyzed the fragmentation from concrete spalling damage though testing and concluded that the size and shape of the fragments obey Weibull and Lognormal distributions respectively. Wu (C. Wu et al. 2010) also investigated the influence of charge shape and orientation on the reflected blast pressure and impulse on concrete slabs, and concluded that

UFC pressure and impulse prediction approach (Sudeep and Rao 2019) may not capture the influence of charge shape. Li (Jun Li et al. 2016; Jun Li, Wu, and Hao 2015) studied the blast resistance of Ultra High Performance Concrete slabs for contact blast and compared the performance of Ultra High Performance Concrete slabs with conventional concrete slabs. Mao (Mao et al. 2015) studied ultra high-performance fiber reinforced concrete slabs under blast loading. The test specimens are only 2.5 cm thick and reinforced with steel fibers but showed satisfying performance against blast loads. Yi (N. H. Yi et al. 2012) also studied the use of ultra high-performance concrete and the influence of the addition of reactive powder concrete on the performance, and reported better blast resistant performance of those two types of concrete. Tabatabei (Tabatabaei et al. 2013) also investigated the effectiveness of fibers reinforced concrete but the fibers are made of carbon. Luccioni (Luccioni et al. 2017) used long steel fibers with hooked ends on both static and blast tests. Castedo (Castedo et al. 2015) carried out field tests on different material compositions and a steel plate in front of concrete slab as protection layer. Yamaguchi (Yamaguchi et al. 2011) studied the resistance of doubled layered concrete slabs. Another testing technique is to use a concrete cylinder in Split Hopkinson Bar Tests, and L. Zhang (L. Zhang et al. 2009) and S. Zhang (S. Zhang et al. 2016) studied spallation and strength of concrete through this test apparatus.

Numerical studies of concrete blast damage involve efforts from many aspects, for example accurate representation of blast loads, reliable and efficient blast-structure interaction scheme and advanced high strain rate concrete constitutive models. As the computational technology advances and rapid development of Hydrocodes (Zukas 2004), three dimensional problems and the complex tri-axial behavior, plasticity either associated or non-associated, strain rate effect and realistic Equation of State could all be included. However, numerical studies (Jun Li, Wu, and Hao 2015; Xu and Lu 2006; X. Q. Zhou et al. 2008; Kandil et al. 2014; Jun Li and Hao 2014) tend to focus on the constitutive modeling but detailed failure mechanism of concrete blast damage may have been overlooked. A number of concrete models that dealt with high strain rate impulsive loading are developed. Holmquist-Johnson-Cook (HJC) model (Holmquist, Johnson, and Gerlach 2017) is one of the pioneer works that dealt with concrete impulsive loading and its development can be traced back to their early works on ductile metal materials (Holmquist and Johnson 2011; Johnson 1983). Broadhouse (Broadhouse 1995; Broadhouse, B.J. and Neilson 1987) developed the Winfrith model. Malvar (Malvar et al. 1997) developed the Karagozian & Case Concrete (KCC) model which is enhanced from a prior Pseudo Tensor model in DYNA3D from Lawrence Livermore National Laboratories. Schwer and Murray (L. E. Schwer and Murray 1994; Murray, Abu-Odeh, and Bligh 2007; Murray 2007) developed the Continuous Surface Cap Model (CSCM). Riedel developed the Riedel-Hiermaier-Thoma (RHT) model and applied it to a number of cases with success (Riedel W. 2000; Riedel, Kawai, and Kondo 2009; Grunwald et al. 2017; Riedel, Wicklein, and Thoma 2008). A survey report of popular concrete models are available by Brannon (Brannon and Leelavanichkul 2009) and other reports focusing on comparison of different models are also helpful (L. Schwer 2010); (Y. Wu, Crawford, and Magallanes 2012). Following the original models, there have also been some proposals for modifications of popular existing concrete models such as ones by Tu (Tu and Lu 2010; 2009), Kong (Kong et al. 2017) and Jiang (H. Jiang and Zhao 2015). These concrete models have been validated against comprehensive testing results from both blast and impact loading. This study uses the RHT model.

Backfill of Tunnel Linings and Blast Demands

The influence of backfill properties on the tunnel linings with internal blast events is the focus of this study. Tunnel linings under blast loads have been investigated, however, most existing studies focused on the flexural response of the liner due to an explosion on the ground surface above the tunnel and not within the tunnel bore itself. Koneshwaran (Olmati, Petrini, and Gkoumas 2014) used a coupled Finite Element (FE) - Smooth Particle Hydrodynamics (SPH) approach to study the influence of an external explosion to a segmented bored tunnel and identified possible connection failures between lining segments. Buonsanti (Buonsanti and Leonardi 2013) included a thermal field into the blast analysis through applying temperature and thermal stress to the lining first and then continues with the blast analysis upon the thermal stress field in a consequential order. Yang (Yang, Xie, and Wang 2010) also studied the outcome of an external explosion and associated ground shock to a subway tunnel.

Colombo (Colombo, Martinelli, and di Prisco 2016) investigated the influence of soil and possible gap between tunnel linings and backfill layer, and emphasized on the high-performance fiber reinforced concrete in flexural regime. De (De, Morgante, and Zimmie 2016) experimentally studied the effects of an explosion as well as the effectiveness of a novel foam protection barrier for tunnel explosion but the explosion of concern is also external. Mobaraki (Mobaraki and Vaghefi 2015) compared different cross-sectional shapes of tunnel under external surface explosion. Feldgun (Feldgun et al. 2008; Feldgun, Karinski, and Yankelevsky 2014) looked at an internal blast but the focus is the resulted loads within the tunnel system instead of the strength and failure. There are also studies (Yu et al. 2014; N. Jiang and Zhou 2012; Soheyli, Akhaveissy, and Mirhosseini 2016) that investigate the effects of nearby rock blasting operation but the vibration is not large enough to induce noticeable localized damage such as spallation. Kutter (Kutter, B. L., O'Leary, L. M., Thompson, P. Y., & Lather 1988) and Liu (H. Liu 2009) investigated tunnel blast problems with consideration of tunnel-soil interaction in flexural regime as well.

The concrete damage from blast induced loading has been investigated extensively. It has been well recognized that in a contact or near field blast event, the reflected tensile wave near boundaries is the primary reason for concrete spallation damage. There have been comprehensive studies targeting concrete spallation damage at high strain rate, for example, projectile impact and blast loading. Specifically for concrete under blast loading, Zhou (X. Q. Zhou et al. 2008) Wu (C. Wu, Nurwidayati, and Oehlers 2009), Kandil (Kandil et al. 2014), and Li (Jun Li and Hao 2014; Jun Li, Wu, and Hao 2015; L. Zhang et al. 2009), Zhao (Zhao and Chen 2013) studied the response of reinforced concrete structures experimentally by actual charge as well as numerically. L. Zhang (L. Zhang et al. 2009) and S. Zhang (S. Zhang et al. 2016) studied spallation and strength of concrete through Hopkinson bars tests.

Tunnel Lining Spall Caused by Fire

Concrete is the most common material being used for tunnel liners. Due to its non-combustibility, low conductivity and high thermal capacity, concrete has been long regarded for its fire performance. However, concrete will experience damage due to reduction in strength, non-uniform thermal strain and accumulated pore pressure when it is subject to heat exposure.

Spalling is a typical damage form for heat-exposed concrete which has the potential to lead to further structural consequence in concrete tunnel liners, as the net section is reduced from material loss on the fire-exposed face and reinforcement becomes increasingly exposed to heating (Figure 3). While broad theories have been proposed for fire-induced spalling, the exact mechanism for concrete spalling under high temperature remains a complex phenomenon for which consensus has not been reached (Kodur 2000). One of the most popular theory which induces a concept of "moisture clog" considers the build-up pressure of heated and vaporized moisture as well as the restrained thermal dilation as the main reason for concrete spall (Jansson 2013; Shorter and Harmathy 1961; Kalifa, Menneteau, and Quenard 2000; J.-C. Liu, Tan, and Yao 2018). The "moisture clog" theory was firstly proposed by Shorter and Harmathy (Shorter and Harmathy 1961) in 1961. When a concrete specimen is heated on the surface, the moisture in the layer closest to the surface will first start to expand due to the elevated temperature. The expansion of the moisture within limited volume of the concrete results in higher pressure within that layer, which drives the moisture not only out of the specimen but also towards the inner (cooler) part of the concrete specimen. When the vaporized moisture reaches a colder layer, it will condense. As the heat drives the condensed layer of moisture further into the depth of the concrete, a saturated layer will be formed (i.e. the moisture clog) as the migration of water towards the inside of the concrete becomes restricted. When the fast-growing pressure and energy accumulated within the layer exceeds the tensile strength of the concrete, part of the surface concrete will spall off. Figure 4 illustrates the temperature gradient through the thickness of the concrete specimen and the build-up of pore pressure which reaches its peak at the saturated layer.
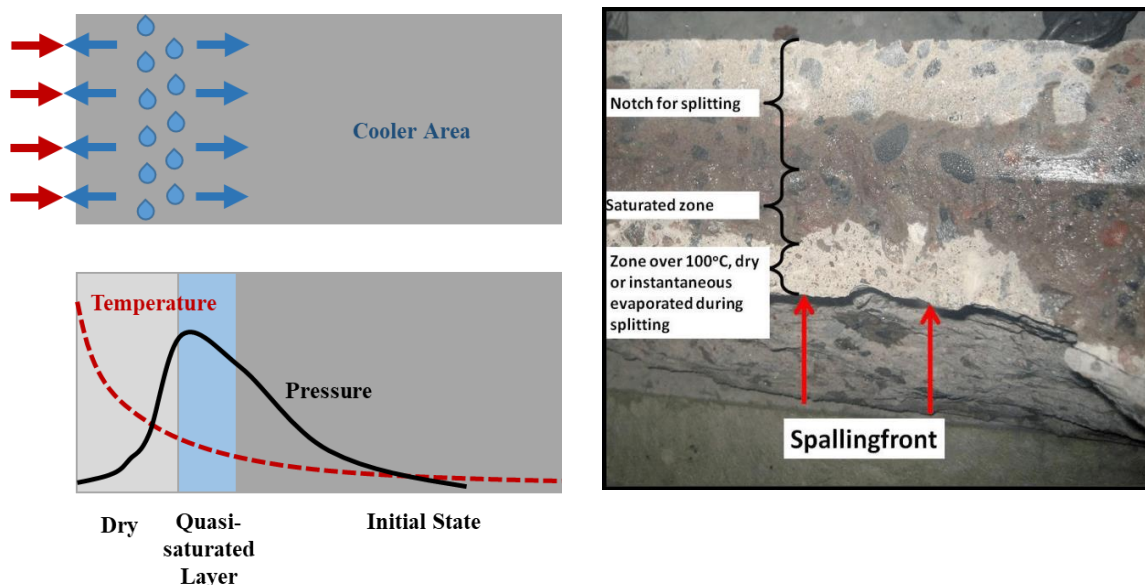
Figure 4: Formation of moisture clog (left) and a picture of split concrete slab during a fire test by Jansson (Jansson 2013) (right)

The Moisture Clog Theory considers concrete spalling under elevated temperature as a thermo-hydro process that includes interaction between the heating rate, the microstructure of the concrete (permeability) and moisture content of the concrete. There has been a significant amount of previous research to verify and further investigate this theory. Kalifa et al. (Kalifa, Menneteau, and Quenard 2000) conducted an experimental study for normal strength concrete (4.5 ksi) and high strength concrete (14.5 ksi) at high temperatures by applying the heat on one face of the

concrete panel up to 800℃. The time history of the thru-thickness pressure and temperature was recorded as well as the mass of the specimen. The temperature results for the two types of concrete showed similar behaviors because of the similar thermal properties such as thermal conductivity and specific heat. The pressure measurement showed a migrating peak from the heated side to the unheated side. A slight plateau in the temperature time history for each depth into the specimen could be observed around 200℃, which happened at the same of the pressure peak. This observation verified the hypothesis of a saturated layer where the moisture is switching phases between liquid and steam. However, there was no discussion about the relationship between the pore pressure and the tensile strength of the concrete under high temperature. Additionally, there has been research studying the influencing factors for concrete spall such as temperature of the heating source (Khoury 2000), concrete moisture content (Vorechovská 2019), concrete permeability (Dwaikat and Kodur 2009) and thickness of the specimen (Le et al. 2016). A reliable and quantified criterion for concrete spall still requires more research work to achieve.

Chapter 4: Concrete Behavior Due to Blast Events

Blast events can be categorized as contact, near field and far field events. In tunnels, because of the tight space combined with the possible large carrier size blast events are more than likely to fall into the near field. In near field blast events, the primary damage mode is local spallation and breach instead of flexural damage that often occurs in far field blast events, and the cause for the localized damage has been recognized as stress waves.

Stress Wave Propagation

It has been well recognized that in the near field blast events, localized breaching and spalling is dominant as opposed to flexural damage of wall or slab components in far field blast events. The load leading to localized damage modes is stress waves and stress waves can be categorized into compressive primary wave (P-wave), shear wave (S-wave), and surface waves, Love wave and Rayleigh surface wave. For near field structural analysis, due to relatively large shear resistance and low tensile strength of concrete, the primary wave plays the major role in damaging concrete and therefore is of interest in this study. The wave transmission and reflection are governed by Wave Equation which has been introduced in the previous section.

To explicitly illustrate the wave reflection, three typical waves (triangle, rectangular and reverse triangle) are analyzed graphically in Figure 5. A triangle wave that has a vertical front is analyzed since it is most representative of a perfect blast load wave without the negative phase. The negative phase can be neglected because it only reduces the total amount of impulse input on the structure resulting in non-conservative analyses. The vertical red lines at the center represent the free boundary of the 1 D bar, and dotted portions at the right side of the free boundary in Figure 5 are virtual reflections that travel in the opposite direction, and they are plotted to facilitate understanding of the reflection phenomenon. The shaded parts represent the final wave shape after superimposing both incoming and reflected waves. As demonstrated in Figure 5, only the positions at least a half wave length away from the free surface starts to undergo the peak of the reflected tensile wave. Within the half wave length, the reflected tensile wave becomes smaller as it is closer to the free surface. At the free surface, the incident and reflected always cancel out each other resulting in zero stress in the axial direction. However, due to concrete yielding, the actual blast waves can vary in shapes, for example flat wave with a plateau instead of sharp triangle shape is possible. The pattern of reflection depends on the shape of waves and other realistic wave shapes are also shown in Figure 5.
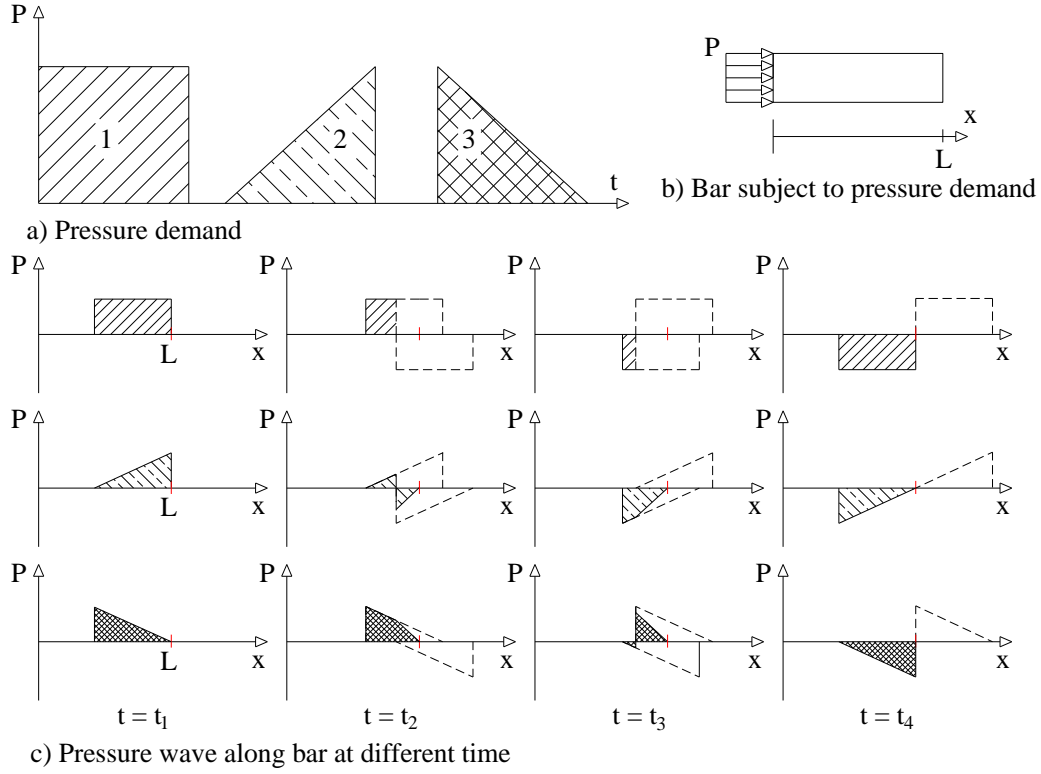
Figure 5: Reverse triangle wave.

Concrete Behavior

Concrete in quasi-static state is a brittle material however at high strain rate impulsive loading condition it shows significant ductile behavior (D.L. Grote, S.W. Park 2001; Vu et al. 2009; Piotrowska, Forquin, and Malecot 2016). In some concrete models, for example the CSCM (Livermore Software Technology Corporation 2014), damage is categorized into brittle damage and ductile damage. Brittle damage is defined as damage that occurs under tensile pressure and the ductile damage is defined as the damage that occurs at compressive pressure. Thus, at high strain rate concrete strength surface has dependency not only on effective stress (Von-Mises stress) but also pressure. The strain rates of typical events are shown in Figure 2.

As computer capacity and computational methods developed rapidly during the last several decades, numerical models have gained popularity. Since 1950s, a series of computer programs that are specifically tailored to accommodate wave propagation problems has emerged. These programs are referred to as hydrocodes. A detailed introduction and history of hydrocodes by Zukas can be found (Zukas 2004). Unlike conventional finite element codes, hydrocodes decompose the stress into pressure component and deviatoric stress component as in Eqs. (1) and (2). The pressure component results in volumetric deformation whereas the deviatoric stress component results in shear deformation.

$$\sigma_p = \frac{\sigma_{11} + \sigma_{22} + \sigma_{33}}{3} = \frac{I_1}{3} \tag{1}$$

$$\sigma_s = \sigma - \sigma_p \tag{2}$$

Where σ_{ii} = principal stresses; I_1 = first stress invariant. The concrete models for high strain rate impulsive loading have been developed for hydrocodes. To name a few, Karagozian and Case (K&C) model, Riedel-Hiermaier-Thoma (RHT) model, Surface Cap Model (CSCM) and Winfrith model are all frequently used. A detailed survey of popular concrete models are available by Brannon (Brannon and Leelavanichkul 2009). This study utilizes the RHT model. The RHT concrete model was developed as early as in 1997 and appeared later in Riedel's dissertation at Ernst-Mach-Institute (Riedel W. 2000). The RHT model has been successful in a comprehensive number of applications (G. Hu, Wu, and Li 2016; Grunwald et al. 2017; Tu and Lu 2009; 2010; Riedel, Kawai, and Kondo 2009). Following the original models, there have also been some proposals for modifications to improve the strain softening behavior after fractures such as ones by Tu (Tu and Lu 2009; 2010).

Another important aspect of high strain rate concrete model in hydrocodes is the Equation of State. Especially for this study of wave reflection and transmission. Concrete is a porous and multi-phase (cement paste, water and aggregates) material and the stress wave propagation within concrete is a complex topic. Riedel used mesoscale modeling technique and consider concrete as cement, aggregates and water. By testing individual components of the three phases in concrete, Riedel presented the equation of state for the concrete materials (Riedel, Wicklein, and Thoma 2008).

Chapter 5: Blast Analysis Validation

Linear and Elastic Wave Propagation

Three tests were done on three identical concrete slabs that have strength of 5559 psi at the testing time (78 days) and 28 days strength is 5818 psi to study behavior of concrete slab subject to blast. The slabs are 42 inches by 42 inches with 6 inches thickness and a minimum reinforcement of WWR 6×6 inches W $4.0 \times$ W 4.0 was used in the middle details are shown in Figure 6. The same amount of charge, 2 lbs of C4, was used in all three tests and the standoff distances are 2.5 inches, 5.0 inches and 9.0 inches respectively. The slabs are supported on timber beams with contact width of 2.5 inches on all four edges.
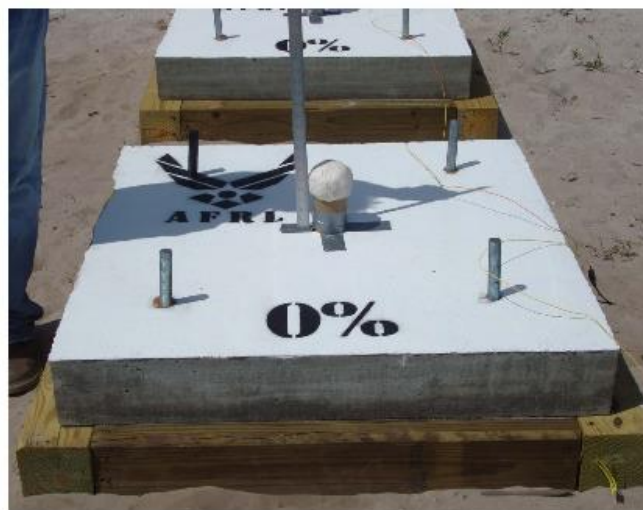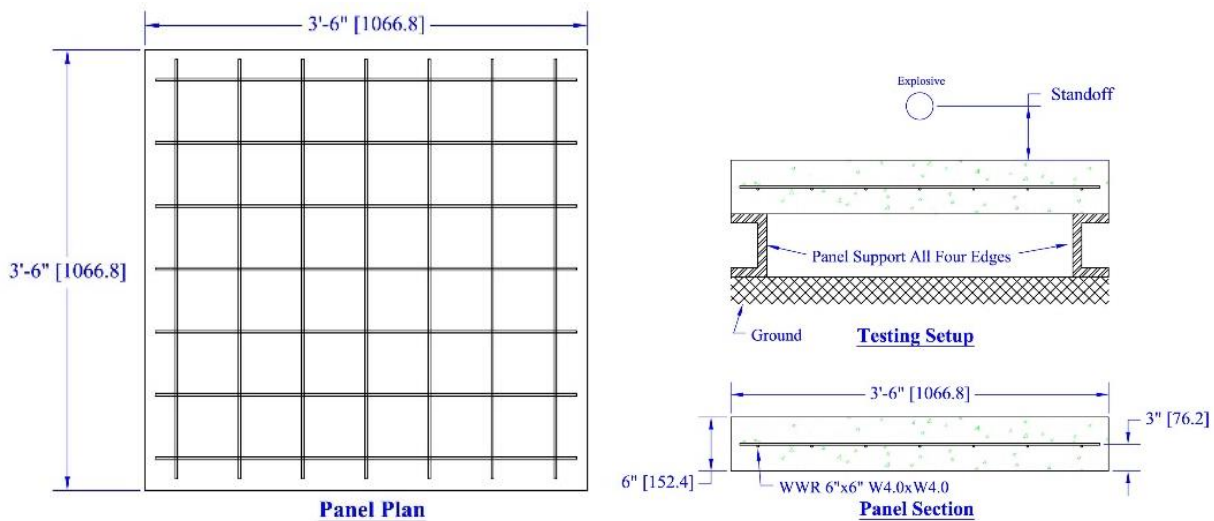
Figure 6: Dimensions and setup (Naito et al. 2014).
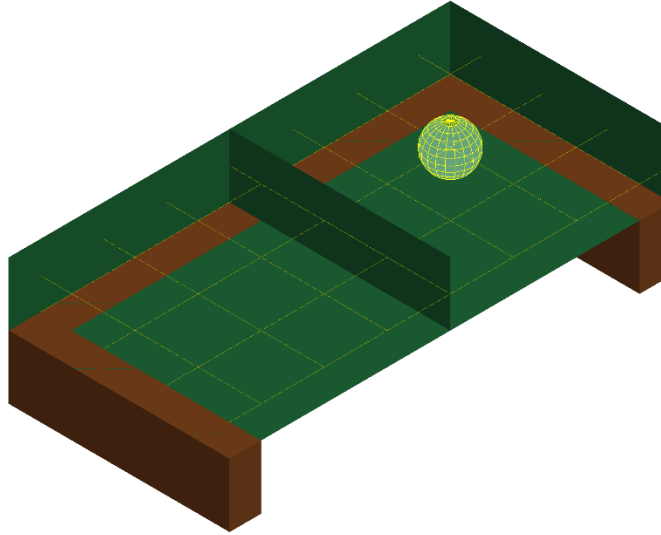
Figure 7: Dimensions and setup in LS-DYNA.

To study the blast wave reflection in thin structural components, a numerical analysis was first done on a perfectly linear elastic material that has the same mechanical properties with the corresponding concrete material in the elastic range during the tests. A quarter model of the concrete slab is meshed with 4.8 million elements by taking advantage of the symmetry around its centroid axis. The 9-inch standoff case is taken as an example and the blast load is modeled with ConWep function through the Load_Blast_Enhanced keyword in LS-DYNA to eliminate the oscillation noises due to Eulerian and Lagrangian domains interaction. The reflected stress wave in the thickness direction, referred as axial direction (Z), is plotted in Figure 8.
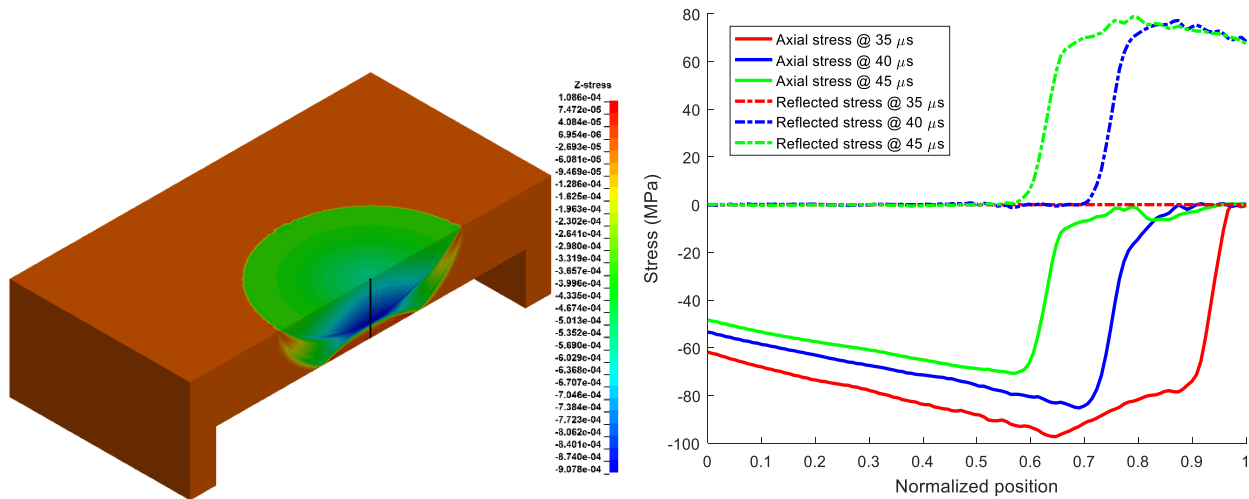
Figure 8: Stress wave propagation and reflection along the depth (left: axial stress contour at 40 μs; right: axial stress at the centroid of the specimen along the entire depth—black line at the left figure.)

In Figure 8, the reflected stress wave is determined by using a reference case and subtracting the actual wave from the reference wave at the same time stamp. As shown in Figure 8, the actual stress wave near the free surface is relatively small and mostly in compression (as shown in the right figure) until the reflected stress wave reach the middle of the slab (as shown in the left figure

at 100 μs). However, at the time the axial reflected stress wave arrives at the front face and the overall axial wave becomes mostly tensile along the entire depth, damage would have already occurred if concrete material damage is considered, which will be demonstrated in the later section.

Material Behavior - Concrete Damage

To perform realistic numerical analyses of concrete behavior in blast, the RHT model is employed in the LS-DYNA program (Livermore Software Technology Corporation 2014). The original RHT model's default input was interpolated between 35 MPa and 140 MPa concrete (Riedel W. 2000) and may show stiffer behavior in the softening portion. Thus the suggested modifications from Tu(Tu and Lu 2009; 2010) are adopted to better account for the post-failure softening behavior. Multi-Material Arbitrary Lagrangian and Eulerian (MM-ALE) approach was used to explicitly model the charge, air, concrete specimen as well as the interaction between them.

Before moving to the full-scale modeling of high strain rate blast loading, two validation cases are carried out as validations of the modeling technique. The first set of validation case as shown in Figure 9 through Figure 11 is a conventional reinforced concrete slab subjected to 0.907 kg (2lbs) of C4 charge at 127 mm (5 inches) above the center of the concrete slab. The concrete slab was 1066.8 mm by 1066.8 mm (42 inches by 42 inches) square and supported by timber around its four edges (Naito et al. 2014). The three figures represent three typical failure patterns of concrete slabs, namely, breaching, spalling and scabbing. Breaching damage is caused apparently by very small scaled distance blast and mechanically the concrete material is crashed by compressive pressure.

The second validation case which is displayed in Figure 12 was a conventional reinforced concrete slab laid on ground. The concrete slab is 275 mm thick and 2800 mm by 2800 mm square. 7.3 kg TNT charge was placed 170 mm above the center of the square concrete slab (J. Wu and Chew 2014; Jun Wu 2012).

The computational models for the two validation cases only built a quarter of the actual tested specimens by taking advantage of symmetry of concrete slabs. The models although reduced through symmetry still consist of 5.6 million (Naito et al. 2014) and 4.36 million (J. Wu and Chew 2014; Jun Wu 2012) solid elements with reduced integration respectively. Hourglass energy control was activated for the reduced integration elements. Multi-Material Arbitrary Lagrangian and Eulerian approach was used to explicitly model the charge, air, concrete specimens and the interaction between them.
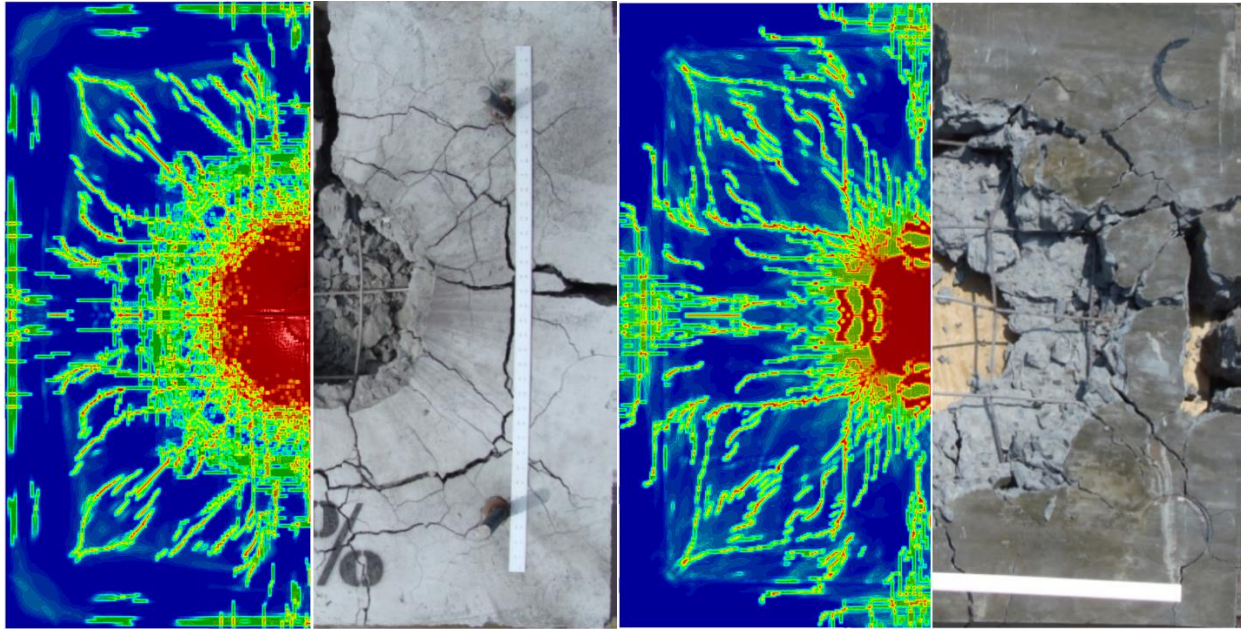
Figure 9: Damage comparison of reinforced concrete slab (Front: left; back: right)
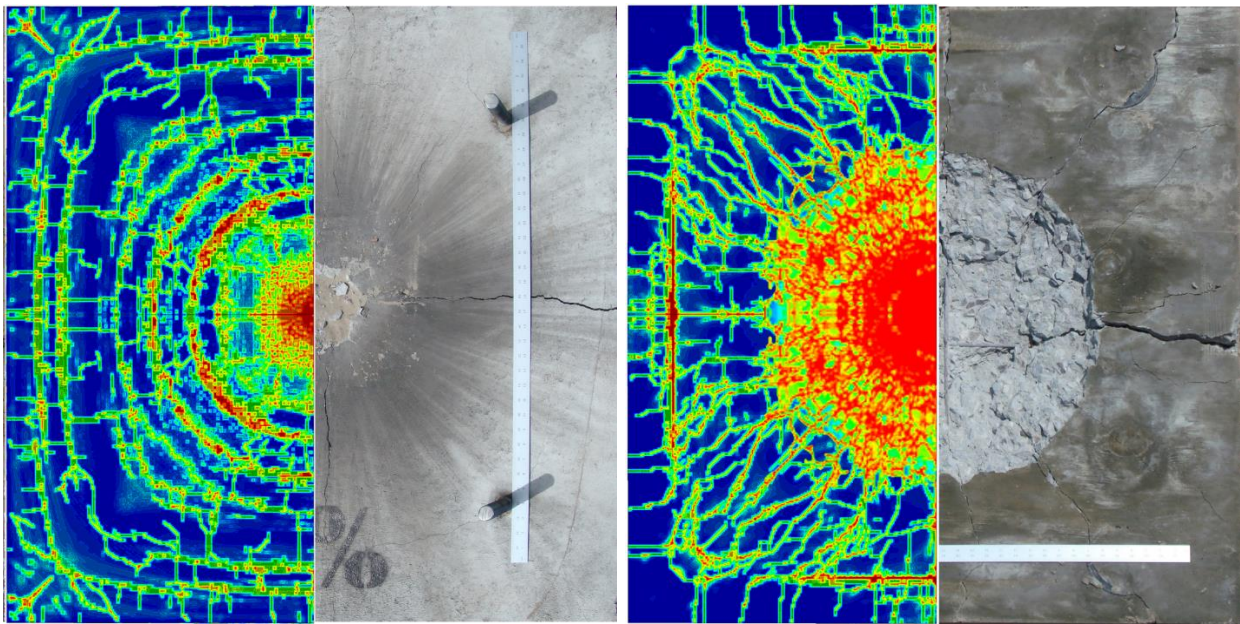
Figure 10: Damage comparison of suspended reinforced concrete slab (Front: left; back: right)
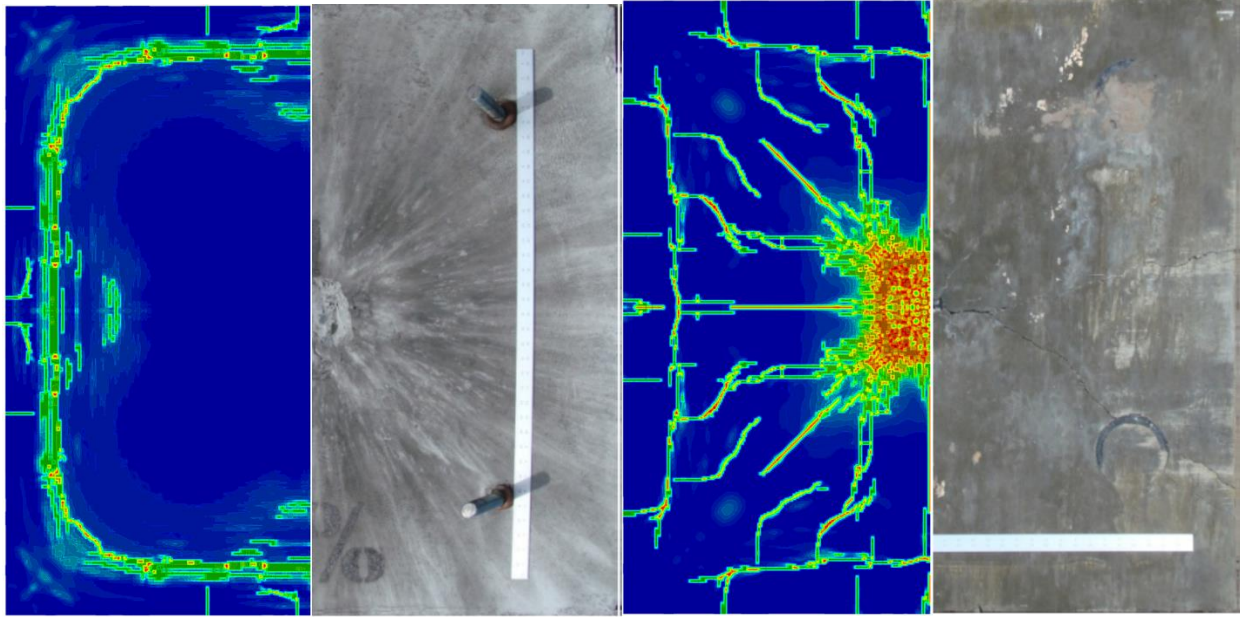
Figure 11: Damage comparison of reinforced concrete slab (Front: left; back: right)
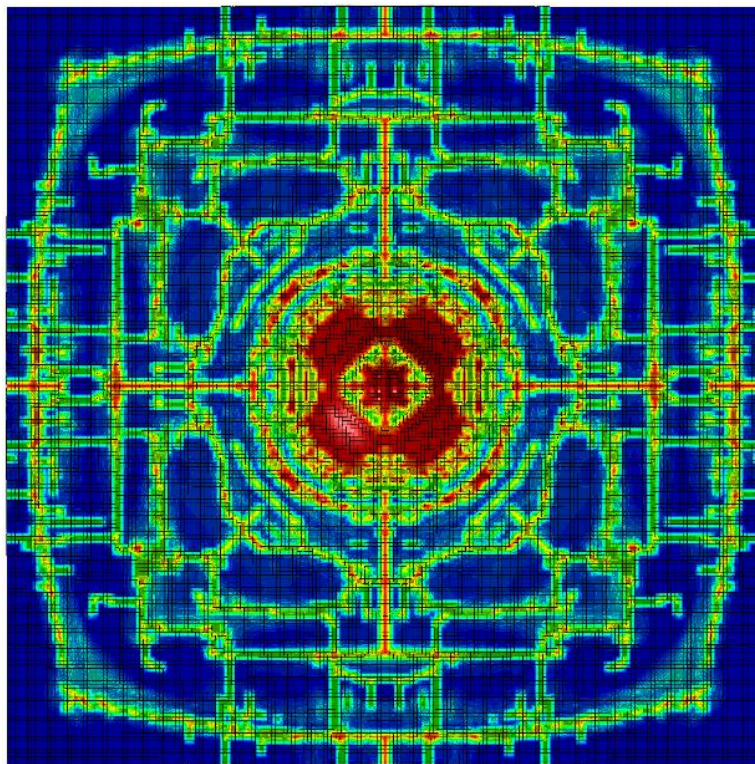
Figure 12: Damage comparison of supported reinforced concrete slab

The numerical results are shown in Figure 9 through Figure 11, as well as Figure 12 demonstrate that the testing results and numerical analyses agree with each other well. So, the models can be used to study concrete slabs under blast loading.

Chapter 6: Influence of Subgrade on Tunnel Lining Subjected To Blast

Analytical Solution of Wave Propagation in Concrete

There are two approaches to analytically study the wave propagation in solids. The first approach is to use Euler Equation and Rankin-Hugoniot jump conditions and the second one is Wave equation which is simply derived based on the Newton's second law. Each is explained

Rankin-Hugoniot jump conditions

The Rankin-Hugoniot jump conditions, which consider the shock waves as discontinuity, and to consider momentum, mass and energy conservation respectively in the following form:

$$p - p_0 = \rho_0 U u \tag{3}$$

$$\rho_0 \left(U - u_0 \right) = \rho \left(U - u \right) \tag{4}$$

$$e - e_0 = \rho_0 A U t u^2 \tag{5}$$

Where U = shock velocity; u = particle velocity; e = energy. Shock velocity, in a linear fashion, can be written as:

$$U = c + su \tag{6}$$

Where c = sound velocity; s = empirical constant. Note, the shock impedance in Eq. (6) is written in first order but an additional second order term u_p^2 can be used. As it is shown in Eq (6), the shock impedance is dependent on the particle velocity that varies between problems. The constant s is material constant and typically ranges from 0.75 to 2.5(Jeandin 2012), which is not very large. Therefore, in low speed shocks the product of su_p is much smaller than the acoustic velocity and therefore negligible. Plugging Eq. (6) into Eq. (3):

$$p - p_0 = \rho_0 c u + \rho_0 s u^2 \tag{7}$$

Eq. (7) can be plotted in the p - u plane and the curve is known as Hugoniot curve. A straight line can be drawn to link two points, the initial state and the state under shock, in the Hugoniot curve. This line is called Rayleigh line and its slope represents the shock impedance $\rho_0 U$.

An equation of state can also be used as an alternative to replace Eq. (6) to solve the Rankin-Hugoniot equations. The Mie-Gruneisen Equation of State (EoS) is one of the most frequently used EOS and it will be discussed in details later. Another key feature of concrete under shock loading is the compaction. Concrete is a very typical porous material and under shock loading it has a compaction curve. The compaction curve starts at zero and goes up linearly until the pores begin to collapse at the Hugoniot elastic limit (HEL). After the pore collapse, a nonlinear curve reaches all the way to the full compaction pressure.

Wave equations

Rankin-Hugoniot jump conditions are applicable to strong shocks that are considered discontinuity. For weak shocks, analysis based on wave equation is a good and practical first approximation. Wave equation studies the phenomenon of stress wave propagation in solids and can be simply derived based on the Newton's second law. Take a bar as the example and on a differential element, the equilibrium can be written as:

$$\rho A dx \frac{\partial^2 u}{\partial t^2} = A \left(\sigma + \frac{\partial \sigma}{\partial x} dx - \sigma \right) \tag{8}$$

Recalling

$$\sigma = E \frac{\partial u}{\partial x} \tag{9}$$

Plugging Eq. (9) into the right hand side of Eq. (8), the governing equation can be obtained as:

$$\frac{\partial^2 u}{\partial t^2} - c^2 \frac{\partial^2 u}{\partial x^2} = 0 \tag{10}$$

Where c = speed of sound in rod = $\sqrt{(E / \rho)}$; u = particle velocity. Eq. (10) is a partial differential equation although greatly simplified in one dimension space. Taking advantage of this simplified form in one-dimension space and assuming two near variables:

$$\alpha = x - ct \tag{11}$$

$$\beta = x + ct \tag{12}$$

The Eq. (10) can be written as:

$$\frac{\partial u^2}{\partial \alpha \partial \beta} = 0 \tag{13}$$

The solutions to Eq. (13) can take many forms as the input waves and boundary conditions vary but all the solutions can be shown in a general form:

$$u = f(x + ct) + g(x - ct) \tag{14}$$

Eq. (14) represents a combination of two waves traveling at the opposite directions in a general form but the resultant waves can only travel in one direction. For the simplicity of analysis, only the wave traveling to the positive direction is kept for analysis. To link the stress with particle velocity, Eq. (14), after eliminating $g(x - ct)$ term, is differentiated with respect to x and t:

$$\frac{\partial u}{\partial x} = f'(x + ct) \tag{15}$$

$$\frac{\partial u}{\partial t} = cf'(x + ct) \tag{16}$$

Eqs. (14) to (16) are in a general form. Stress and particle velocity can be written as:

$$\sigma = E\frac{\partial u}{\partial x} \tag{17}$$

$$v = \frac{\partial u}{\partial t} \tag{18}$$

Recalling in one dimension space, $c^2 = E / \rho$, $c = \sqrt{(E(1-\mu)/(\rho(1-\mu)(1+2\mu)))}$ in 3D, along with Eqs (15), (16) and (18). Eq. (17) can be written as:

$$\sigma = Zv \tag{19}$$

Where $Z = \rho c$. Z is the acoustic impedance. To demonstrate some of the important properties of the stress wave reflection and transmission, the interface of two materials is studied. At the interface the particle velocity and longitudinal force can be written as:

$$v_i + v_r = v_t \tag{20}$$

$$F_i + F_r = F_t \tag{21}$$

Plugging Eq. (19) into Eq. (20):

$$\frac{\sigma_i}{\sigma_1 c_1} - \frac{\sigma_r}{\sigma_1 c_1} = \frac{\sigma_t}{\sigma_2 c_2} \tag{22}$$

Eq. (21) is divided by area to determine the corresponding stresses

$$\sigma_i + \sigma_r = \sigma_t \tag{23}$$

Solving Eqs. (22) and (23), the relations between incident, reflected and transferred waves can be obtained:

$$\sigma_t = \frac{2\rho_2 c_2}{\rho_1 c_1 + \rho_2 c_2} \sigma_i \tag{24}$$

$$\sigma_r = \frac{\rho_2 c_2 - \rho_1 c_1}{\rho_1 c_1 + \rho_2 c_2} \sigma_i \tag{25}$$

After organizing, the transmitted and reflected waves can be written as:

$$\sigma_t = T\sigma_i \tag{26}$$

$$\sigma_r = R\sigma_i \tag{27}$$

Where $T = 2Z_2 / (Z_1 + Z_2)$; $R = (Z_1 - Z_2) / (Z_1 + Z_2)$.

In concrete, shocks propagation and reflection follow the same principals as the stress waves in elastic materials in Eqs. (26) and (27). The only change is that instead of acoustic impedance shocks have to be studied with the shock impedance.

The acoustic impedance of a material can be computed by the following equation.

$$Z = \sqrt{\rho \cdot E} \tag{28}$$

Where ρ is the density of the material and E is the elastic modulus of the material.

Numerical Study of Wave Propagation in Concrete

To demonstrate the influence of subgrade and role of impedance, an elastic material is employed. The key input parameters are summarized in Table 1.

Table 1: Case summary

	Layers	Density (g / cm^3)	Poisson Ratio	Young's Modulus (GPa)	Wave Impedance $(g / (cm^2 \mu s))$	Transmitted (T)	Reflection (R)
A	Top	2.53	0.2	50	1.12	0	1
	Bottom	0	0.0	0	0.0		
B	Top	2.53	0.2	50	1.12	2	-1
	Bottom	$+\infty$	0.0	$+\infty$	$+\infty$		
C	Top	2.53	0.2	50	1.12	0.618	0.382
	Bottom	2.53	0.2	10	0.50		
D	Top	2.53	0.2	50	1.12	1	0
	Bottom	2.53	0.2	50	1.12		

The four cases include one free boundary case, one fixed boundary case, one impedance matching case and one lower subgrade impedance case as shown in Table 1. Results are plotted in Figure 13 to Figure 16, and the results are also summarized in Table 2.
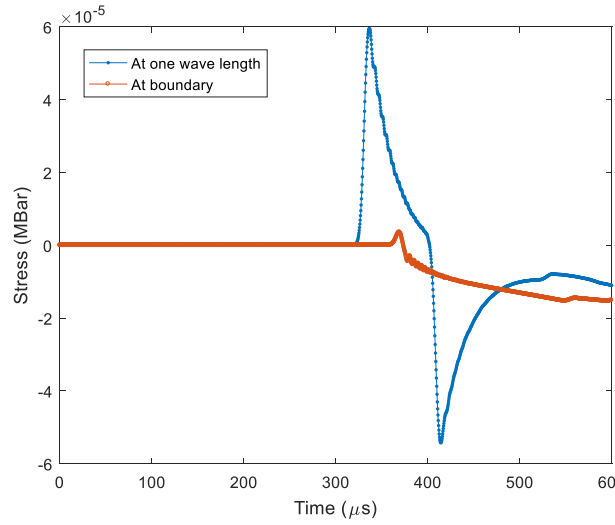
Figure 13: Free boundary case.
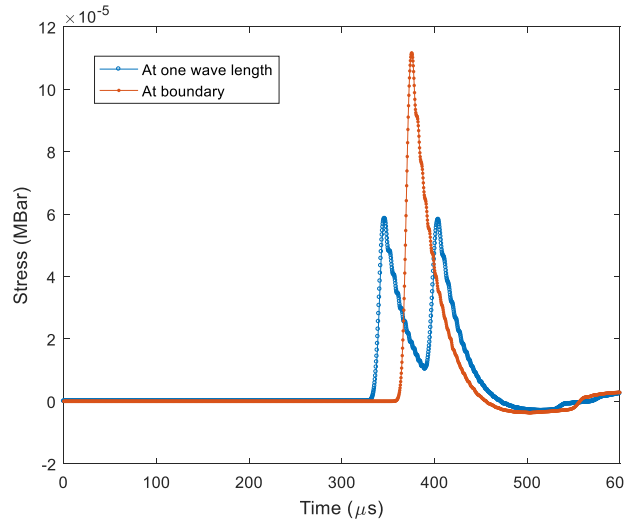
Figure 14: Fixed boundary case.
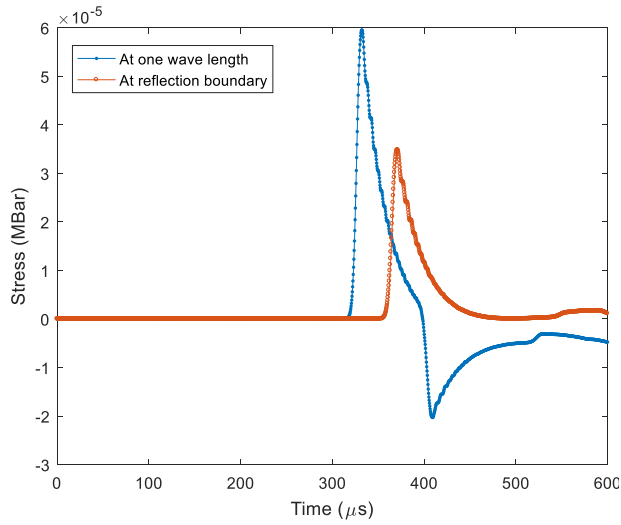
Figure 15: Lower impedance case.
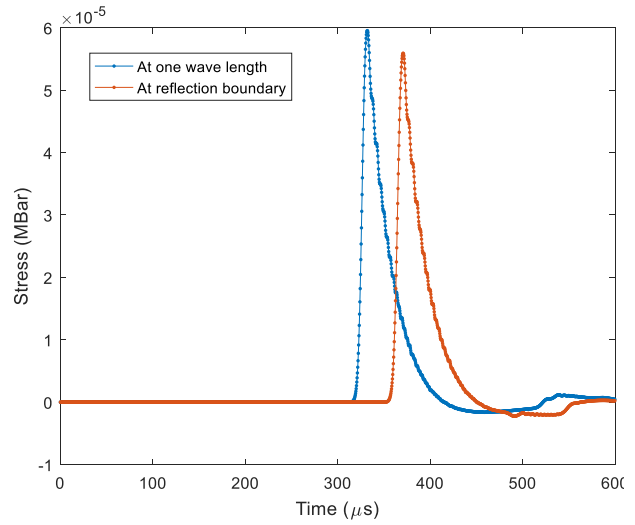
Figure 16: Matching impedance case.

Table 2: Results summary

	Waves	Peak pressure (MPa)	Theory		Calculated		Difference	
			T	R	T	R	T	R
1	Incident	5.95	0	1	0	0.91	0%	9%
	Reflected	-5.42						
	Transmitted	0.0						
2	Incident	5.85	2	-1	1.91	-1.0	4.5%	0%
	Reflected	5.83						
	Transmitted	11.17						
3	Incident	5.95	0.618	0.382	0.58	0.34	6%	8%
	Reflected	-2.03						
	Transmitted	3.48						

4	Incident	5.95	1	0	0.94	0	6%	0%
	Reflected	0.0						
	Transmitted	5.59						

As shown in Figure 13 to Figure 16 and Table 2, the calculated numbers are a little lower than the predicted by theory. The energy loss mainly is through bulk viscosity of the material and the bulk viscosity is introduced to damp out oscillations quickly during wave propagation (Hallquist 2012).

To study the shock propagation in tunnel lining and the subgrades, the RHT concrete model is used. The RHT model defines three damage surfaces, yield surface, failure surface and residual surface. The yield surface is limited with a cap function and strain rate effect is also taken into consideration. In the RHT model the damage is defined as the ratio of current plastic strain divided by the ultimate plastic strain and it ranges from zero to one. In the past, comprehensive studies have been carried out on the concrete response to blast loads. A lot of existing studies focus on the concrete damage. In this study, the influence of subgrade behind concrete is introduced thus the wave transmission and reflection are the primary interest of this study. The wave propagation within concrete and between concrete and subgrade can be influenced by a number of variables, among those, the most important one is the wave impedance. As has been discussed already, the impedance is closely associated with the material property that affects the volumetric response. Therefore, the Equation of state is our primary interest.

Under compressive waves, concrete can become damaged through plastic deformation. Both tensile and compressive stress can induce plastic damage. In civil engineering regime, tensile damage is more common since it takes very large blast pressure to induce the compressive damage in triaxial loading.

To demonstrate possible concrete damage scenarios, ten cases are studied. Among them, five are modeled with concrete materials and the other five are corresponding elastic materials. First, tensile waves may occur when compressive input waves reflect off an interface that has lower wave impedance, and concrete is known for its significant lower tensile strength than the compressive strength. Thus, it is common to see tensile damage on the back of loaded concrete components and this phenomenon is referred as spall. However, if the boundary is properly treated the tensile waves can be avoided.

Figure 17 and Figure 19 demonstrate that it takes relatively small explosion to cause tensile damage. However, Figure 18 and Figure 20 demonstrate that at the same explosion that induce tensile damage on concrete will cause no damage to the concrete if the waves do not reflect as tensile waves. Figure 21 shows that for the components that will have tensile reflected waves can also suffer from compressive damage first.

To demonstrate the transmission and reflection quantified in the theoretical development, models that consist of elastic materials are built in LS-DYNA. Three impedance values are chosen to study the stress wave transmission and reflection.

All the three cases have two layers and the top layer materials are kept the same in all three cases. In the first case, the second layer has smaller impedance than the first layer. In the second case, the second layer has the same impedance with the first layer although the density and stiffness are

both different from the first layer. In the third case, the second layer has higher impedance than the first layer. Note in three-dimensional space, Poisson effect kicks in and the speed of the dilation waves also becomes $c = \sqrt{(E (1 - \mu) / (\rho (1 - \mu) (1 + 2\mu)))}$. However, because in our three computational cases, the Poisson ratio μ doesn't changes therefore it is normalized to exclude its influence.

Table 3: Summary of cases examined

No.	Materials	Concrete Impedance (0.1)	Subgrade Impedance (0.1)	Charge (g)	Boundary condition
1	Elastic	5.0		200	Free
2	Elastic	5.0		600	Free
3	Elastic	5.0		1200	Free
4	Elastic	5.0		600	Fixed
5	Elastic	5.0		1200	Fixed
6	Concrete	5.0		200	Free
7	Concrete	5.0		600	Free
8	Concrete	5.0		1200	Free
9	Concrete	5.0		600	Fixed
10	Concrete	5.0		1200	Fixed
11	Concrete	5.0		5200	Fixed
12	Concrete	5.0	1.0	600	
13	Concrete	5.0	3.0	600	
14	Concrete	5.0	5.0	600	
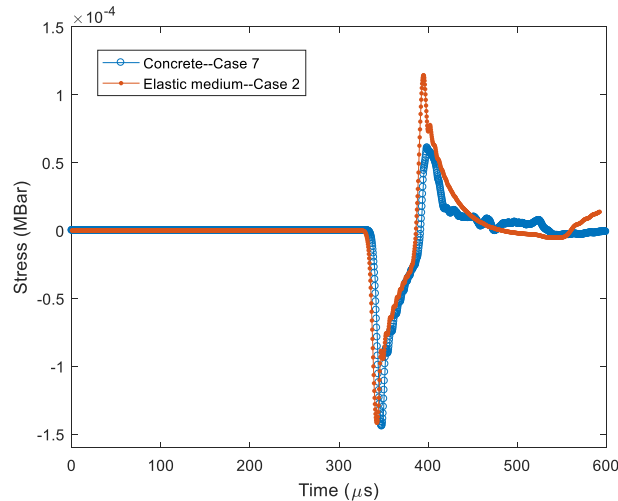
Figure 17: Stress comparison cases 2 and 7.
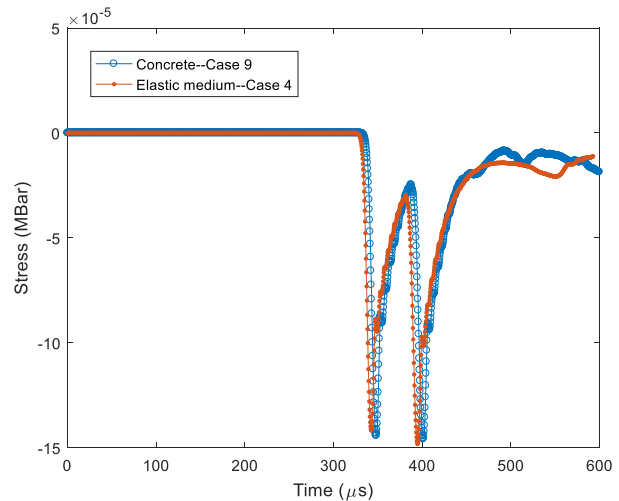
Figure 18: Stress comparison cases 4 and 9.

Figure 17, Figure 18, Figure 19 and Figure 20 compare the influence of different materials and boundary conditions. Figure 17, as shown in Table 3, both cases have 600 grams of charges. However, because the free boundary reflects tensile waves the concrete model (Case 7) suffers from minor concrete tensile damage. Therefore, concrete (Case 7) has a lower reflected stress wave than the elastic material (Case 2). In Figure 18, both concrete and elastic materials are subjected to fixed boundary conditions which reflect compressive waves. As a result, no damage exists in both models and therefore their stress waves are the same.
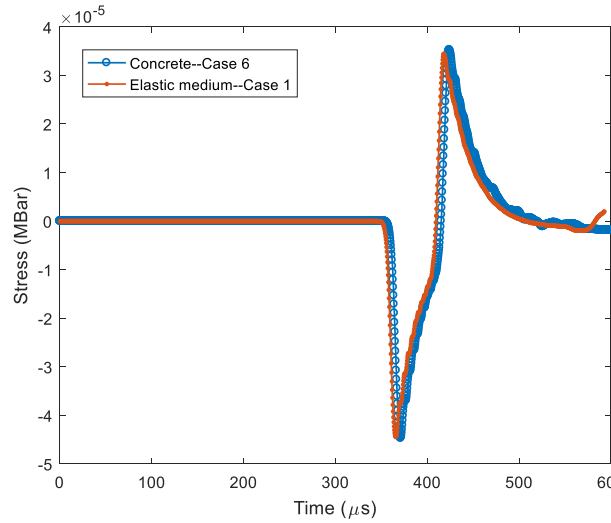
Figure 19: Stress comparison cases 1 and 6.   Figure 20: Stress comparison cases 5 and 10.
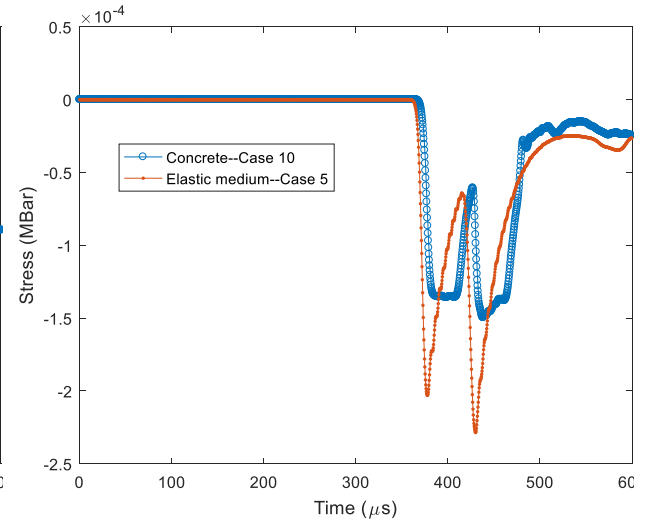
Based on the results in Figure 17 and Figure 18, Figure 19 and Figure 20 further explores the prior cases. Figure 17 showed difference in stress waves because of reflected tensile waves and the associated concrete tensile damage. The question is if the discrepancy in stress waves would disappear when the reflected tensile waves are too weak to cause any concrete material damage. To answer the question, every variable is kept the same except the charge size is reduced from 600 g to 200 g. As expected although the tensile waves are generated at the free boundary the concrete is free from damage and the concrete material model and elastic material model yield the same stress results in Figure 19. Another question is that how the concrete material is damaged by compressive waves. To answer that, the charge size is increased to 1200 g and the results are shown in Figure 20. Obviously, the concrete model has smaller peak stress due to the plastic damage which cannot pass the waves efficiently after its occurrence.
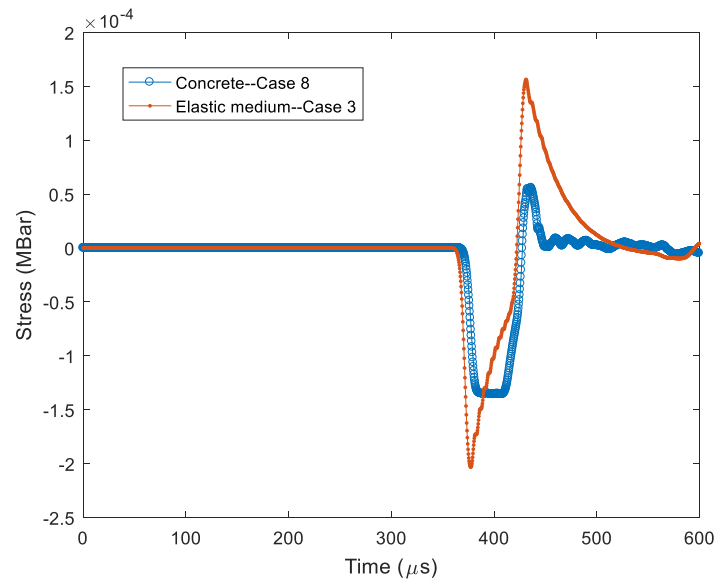
Figure 21: Stress comparison.

Figure 21 shows both compressive and tensile waves damage from a 1200 g charge with free boundary condition. Apparently, the concrete is damaged both in compression and tension.

The question to address is why the concrete suffers from the plastic damage and how to avoid it.

The key is the Equation of State of the concrete materials. Concrete as a porous material has a very distinct volumetric strain vs pressure curve. At certain volume strain, namely, the Hugoniot Elastic Limit (HEL), the pores start to collapse and the compaction is initiated. The EOS employed in RHT model is written as when in compression:

$$p = \frac{1}{\alpha}\left[\left(B_0 + B_1\right)\alpha\rho e + A_1\eta + A_2\eta^2 + A_3\eta^3\right] \tag{29}$$

On the other hand, when in tension, it can be written as:

$$p = \frac{1}{\alpha}\left(B_0\alpha\rho e + T_1\eta + T_2\eta^2\right) \tag{30}$$

The compaction pressure, which is also known as the damage cap, can be written as a function of porosity:

$$p_{cap} = p_{comp} - \left(p_{comp} - p_{el}\right)\left(\frac{\alpha - 1}{\alpha_0 - 1}\right)^{\frac{1}{N}} \tag{31}$$
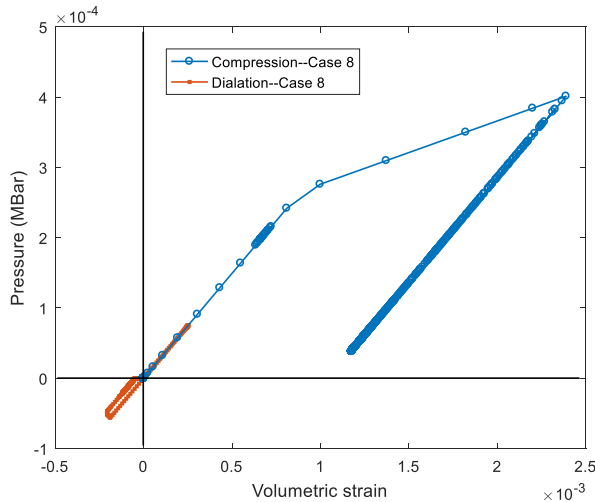
Figure 22. Pressure and volumetric strain relation.
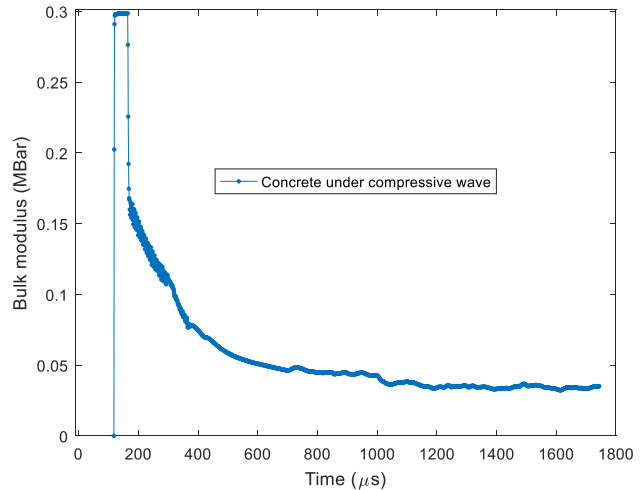
Figure 23. Bulk modulus and time relation.

Figure 22 shows the EoS and Figure 23 shows associated change in bulk modulus. Specifically, Figure 22 shows the volumetric loading and unloading relationship both in tension and compression. The slope corresponds to the bulk modulus in Figure 23.
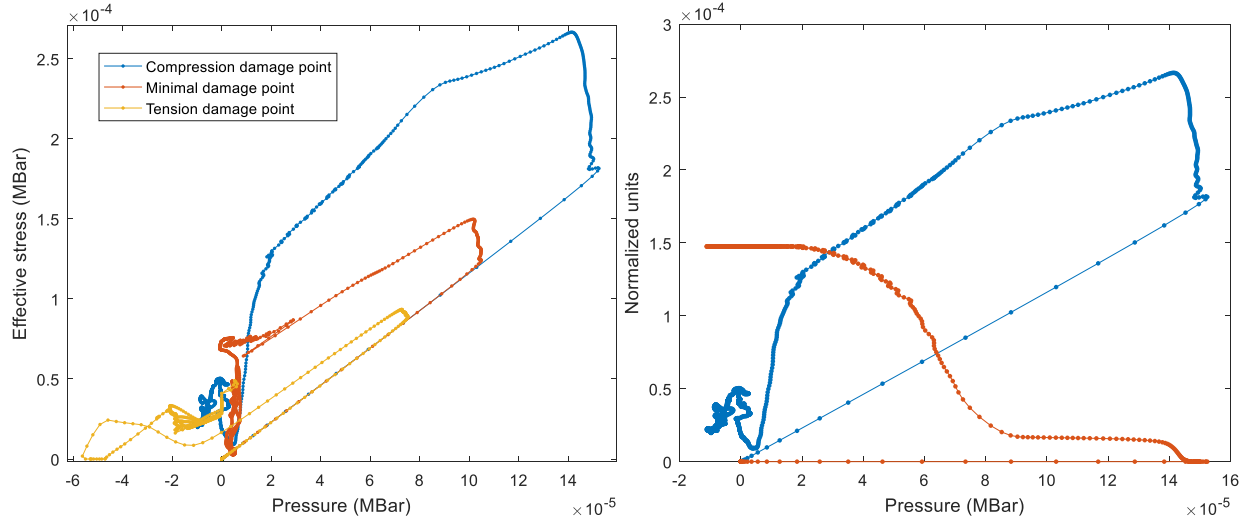
Figure 24: Loading path in pressure and effective stress space.
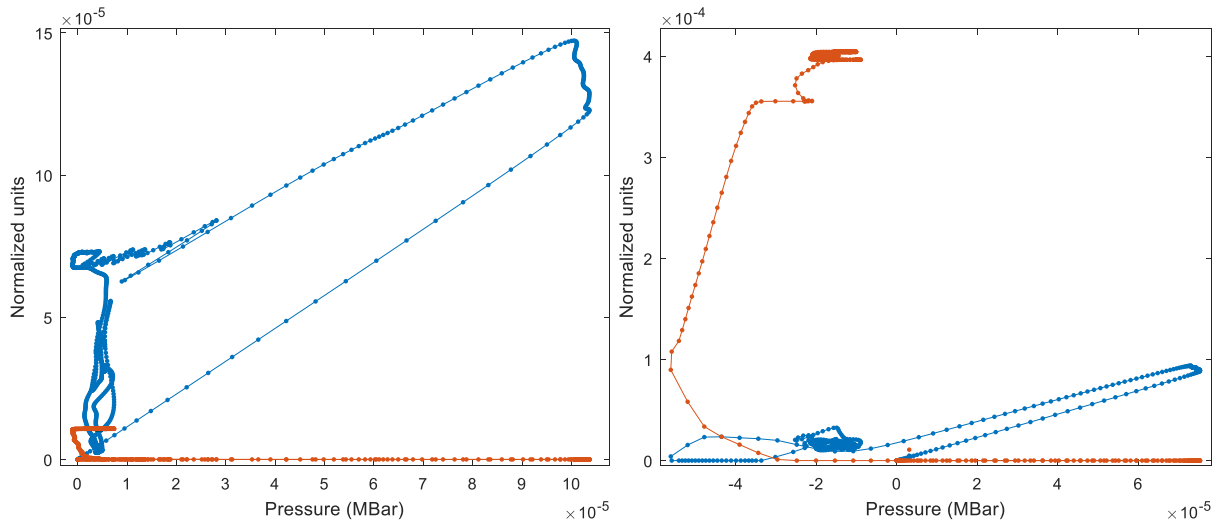
Figure 25: Loading path in pressure and effective stress space continued.

Figure 24 and Figure 25 show the load path in pressure and deviatoric stress space. In this pressure and deviatoric stress space, three damage surfaces representing constitutional law exist and damage accumulate along the path. The trajectory shows how concrete damage evolve along the loading condition. The yellow curve in left hand side of Figure 24 shows obvious tension and the rest, blue and orange lines, shows compression. The effective plastic strain are also plotted in the right hand side of Figure 24 and Figure 25.

Another comparison in details is carried out. The purpose is to show how subgrade can influence damage of the structures above it. The damage pattern from the free boundary case and supported case are shown in Figure 26 and the details are in Table 3.
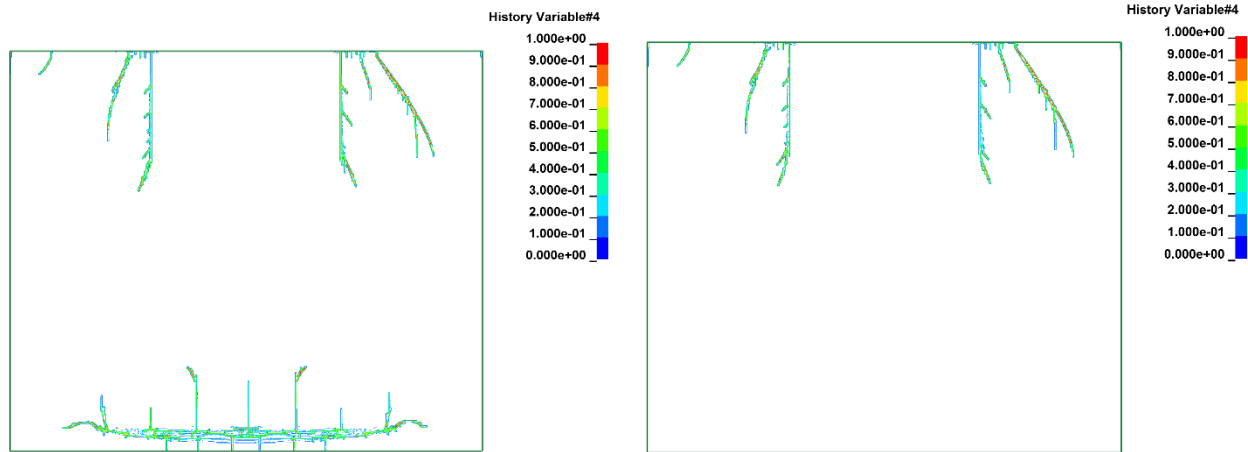
Figure 26: Concrete damage comparison.

In Figure 26, it is apparent that with support the spallation damage can be avoided. Furthermore, the tendency of reduction a function of the subgrade impedance as in Figure 27.
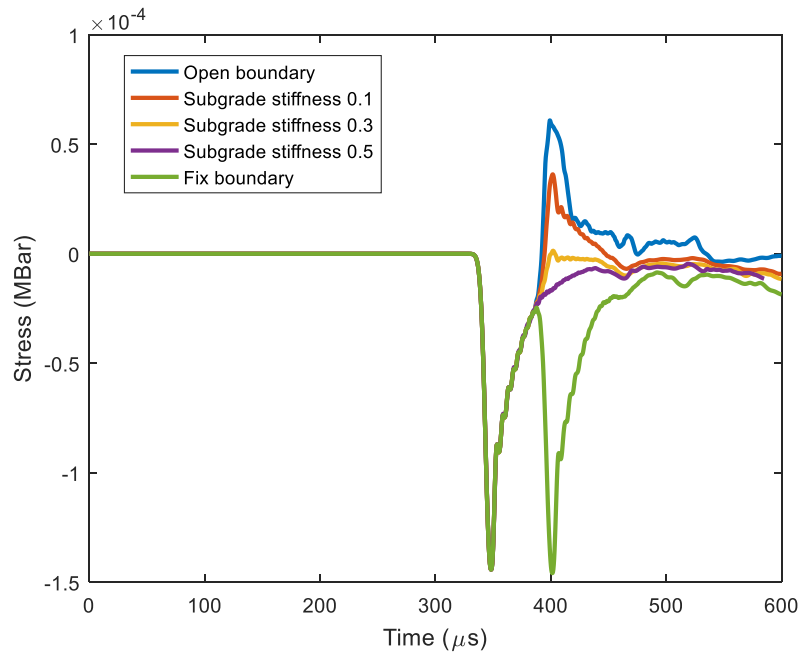
Figure 27: Stress comparison

As demonstrated in Figure 27, free open boundary reflects tensile waves but the reflected tensile waves can be reduced by increasing the subgrade impedance. However, after matching the input media impedance further an increase in wave impedance would reflect compression waves as the fixed boundary case.

Table 4: Case summary results

	Normalized Acoustic Impedance (0.1)	Incident stress (Mbar)	Reflected stress (Mbar)	Reflection percentage	Type
1	free	-1.441e-4	6.092e-5	42.28%	Tension

2	1.0		3.624e-5	25.15%	Tension
3	3.0		1.368e-6	9.49%	Tension
4	5.0		-1.567e-5	-10.87%	Compression
5	fixed		-1.454e-4	-100%	Compression

Tunnel Blast Simulation

To demonstrate the influence of backfill properties on the lining blast resistance, a typical circular tunnel segment is investigated as shown in Figure 28. 18 cases of various conditions are studied. Among them, two cases as upper and lower bounds will be discussed in details. One of the two cases is that the tunnel lining has no backfill and the second case is that the segment has fixed boundary at its exterior. The other cases all have the same dimension, boundary condition, load and backfill on its exterior, but the Young's modulus of subgrade range from 2% to 400% of the concrete segment.

Full models were built and a typical charge of 500 kg TNT was placed near the tunnel segment. Concrete of 40MPa is used for tunnel lining and the subgrade is modeled as elastic solid material. Approximately, three million solid elements are used and the RHT concrete model is adopted with modifications from Tu (Tu and Lu 2009; 2010). The geometry is shown in Figure 28.
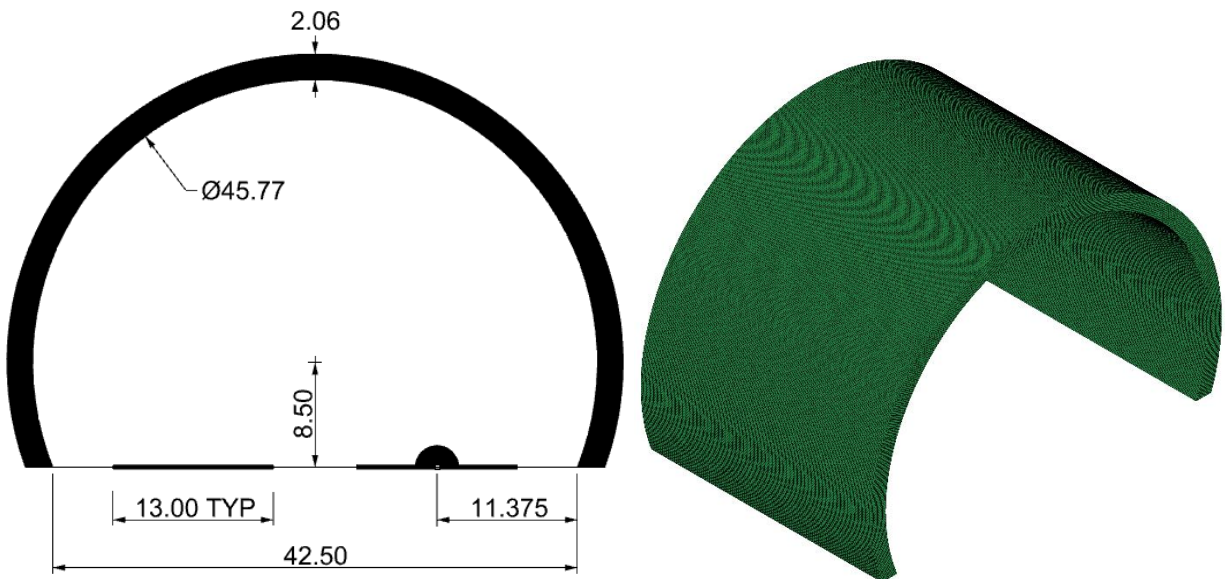
Figure 28: Tunnel segment dimensions (in feet).

The damage of the free boundary and 10% Young's modulus cases are shown in Figure 29 and Figure 30. The exterior(left) and interior(right) are both plotted.
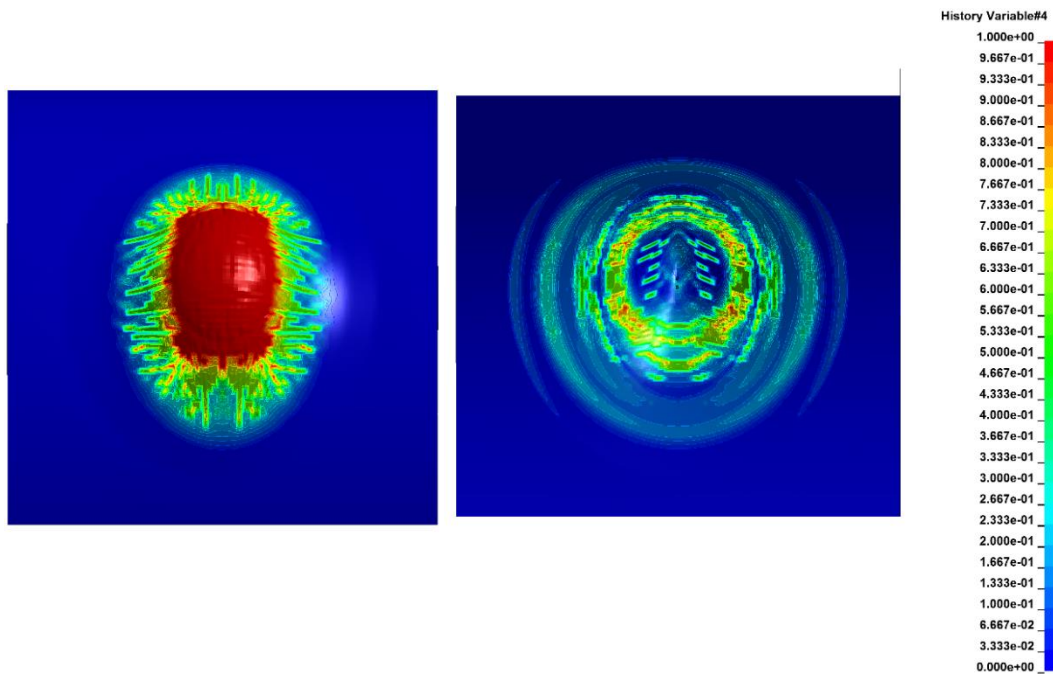
Figure 29: Damage pattern of segment exterior(left) and interior(right).
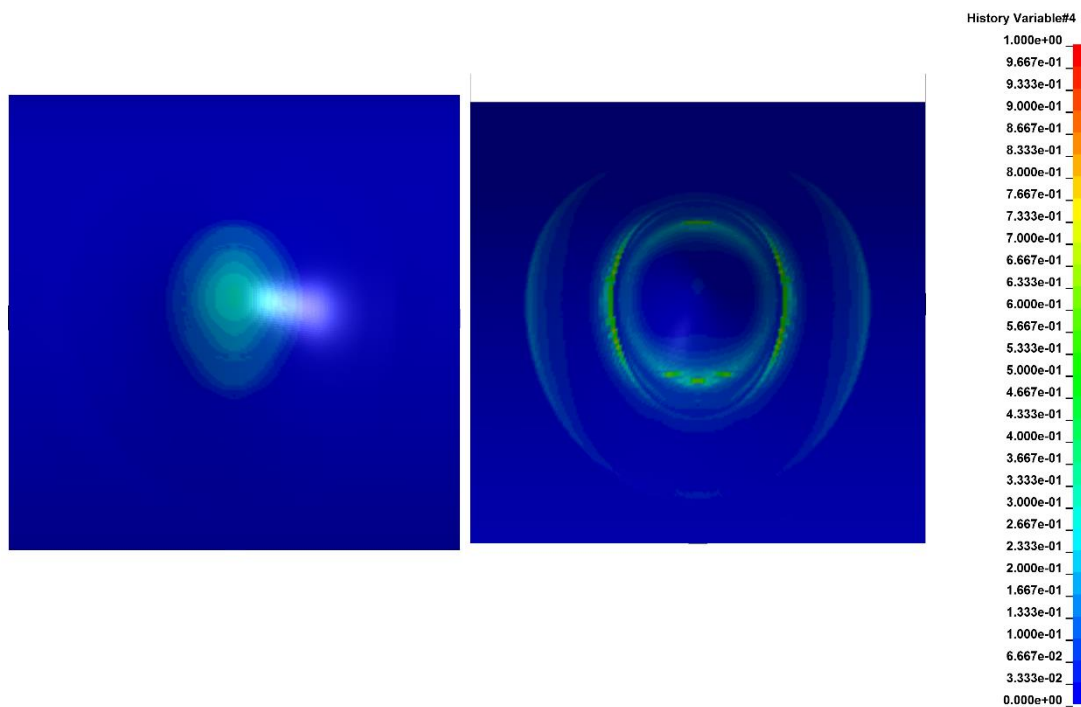
Figure 30: Damage pattern of supported segment exterior(left) and interior(right).

As shown in Figure 29 and Figure 30, the free tunnel segment achieves more damage than the supported. The damage on the free segment is from the tensile stress developed at the free boundary. There is also damage on the supported segment however its magnitude is much smaller. Figure 31 shows the influence of subgrade property on damage. The damage index in Figure 31 is defined based on the damage in RHT model, but instead of on single element the damage index is

calculated based on a section of model, which suffers most damage, at the termination time. The damage index is determined through dividing the sum of damage values in the entire section by the total amount of elements. So that the damage index should be between 0 and 1.
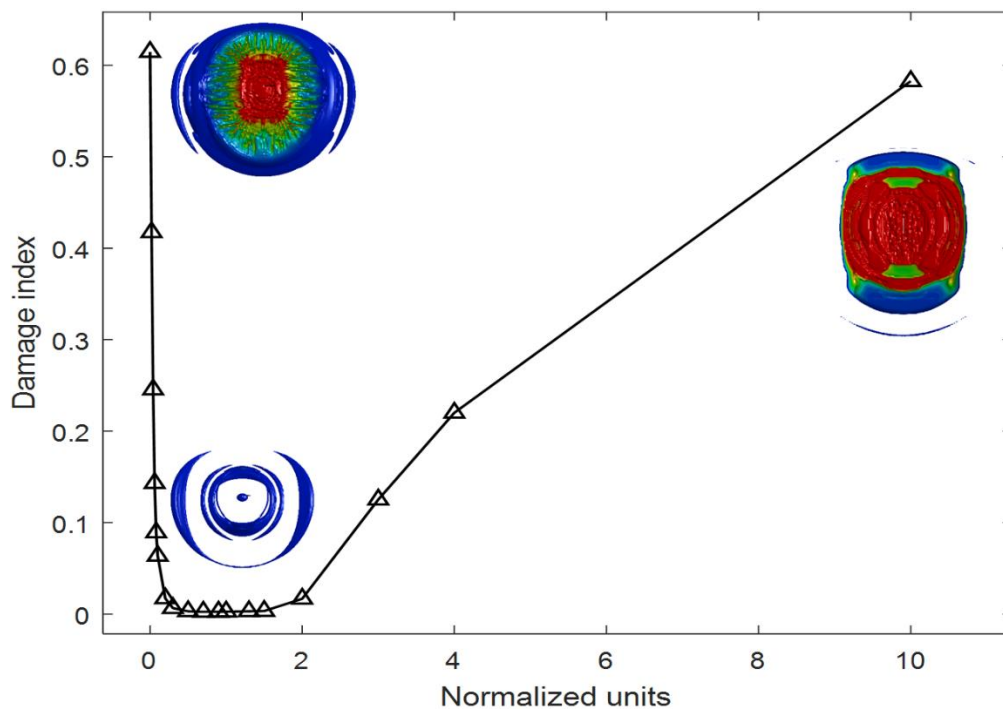
Figure 31: Damage with respect to subgrade property w/ Damage iso-surface illustration.

As shown in Figure 31, damage reduces significantly as subgrade stiffness drops however when the stiffness reaches twice of the concrete stiffness it can bring back damage as it further increases. The failure mechanism is explained by the wave reflection theory derived in the previous section. First, the damage from free surface and very low subgrade stiffness is resulted from tensile wave. As the subgrade stiffness increases the damage is reduced this is because the reflected tensile wave is superimposed and combined with the incoming compressive wave and the resulted compression is increased therefore tensile damage is reduced. However, when the subgrade stiffness reaches certain threshold (200%) the damage picks quickly as subgrade stiffness increases. This is because compression damage becomes dominant at such a subgrade stiffness level.

To quantitatively illustrate this effect, the free boundary and 10% subgrade stiffness cases are discussed in details. Two reference points from each model are taken to compare the influence of the backfill. One of the point is located right above the detonation and the other one is located on the corresponding exterior. The pressure plots of each point from the two different scenarios, floated vs. supported, are shown in Figure 32 and Figure 33. In the subsequent figures, the reference case is the tunnel liner that has infinite thickness.
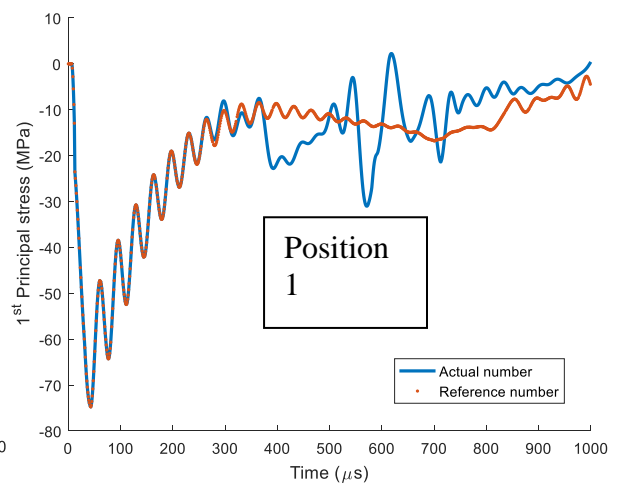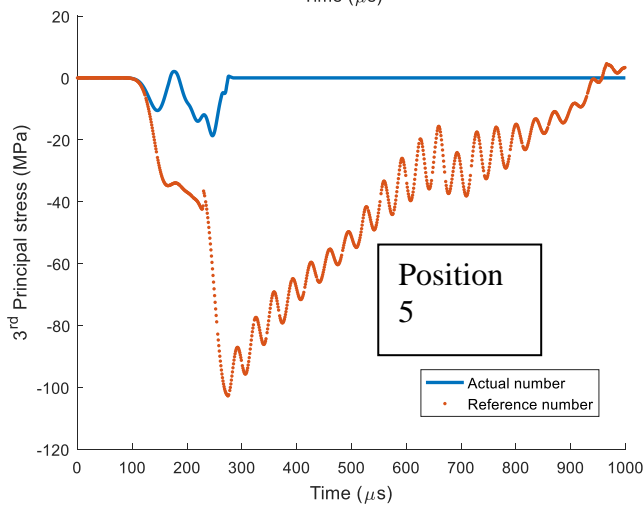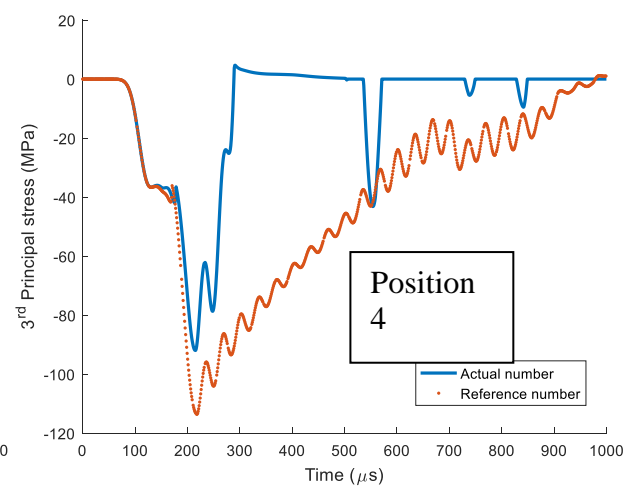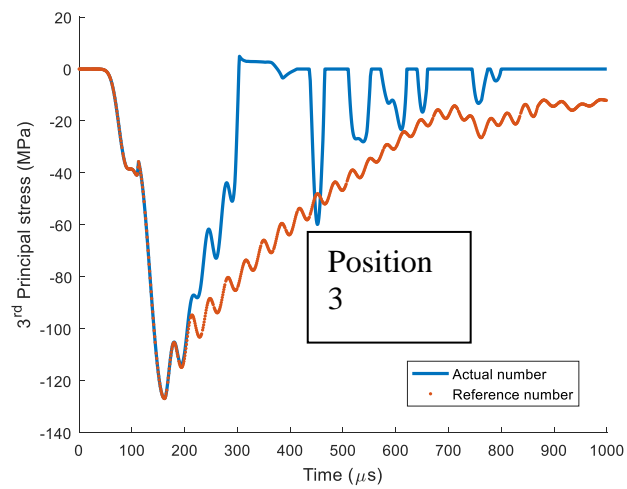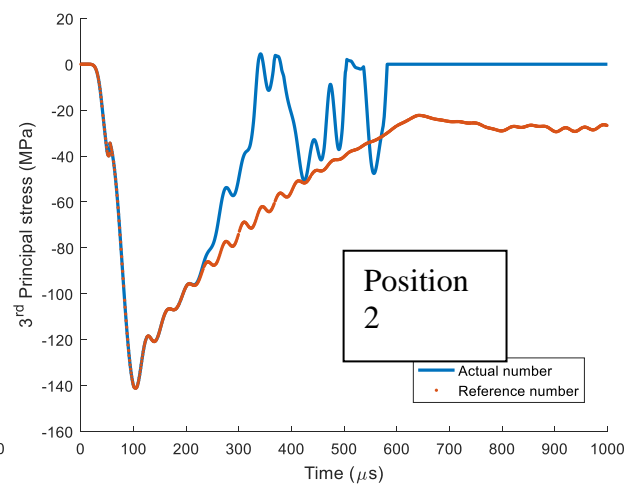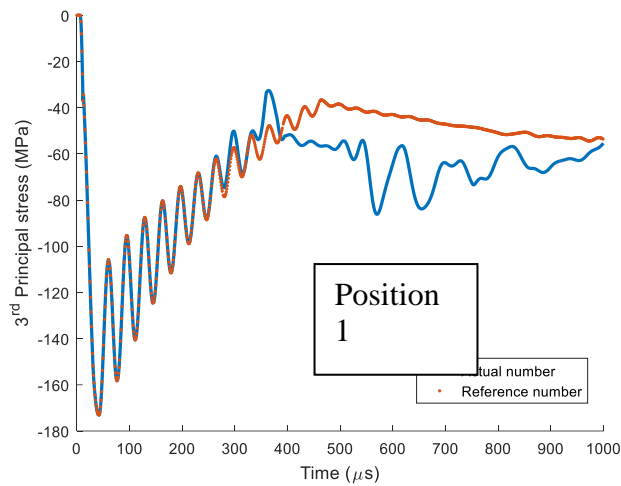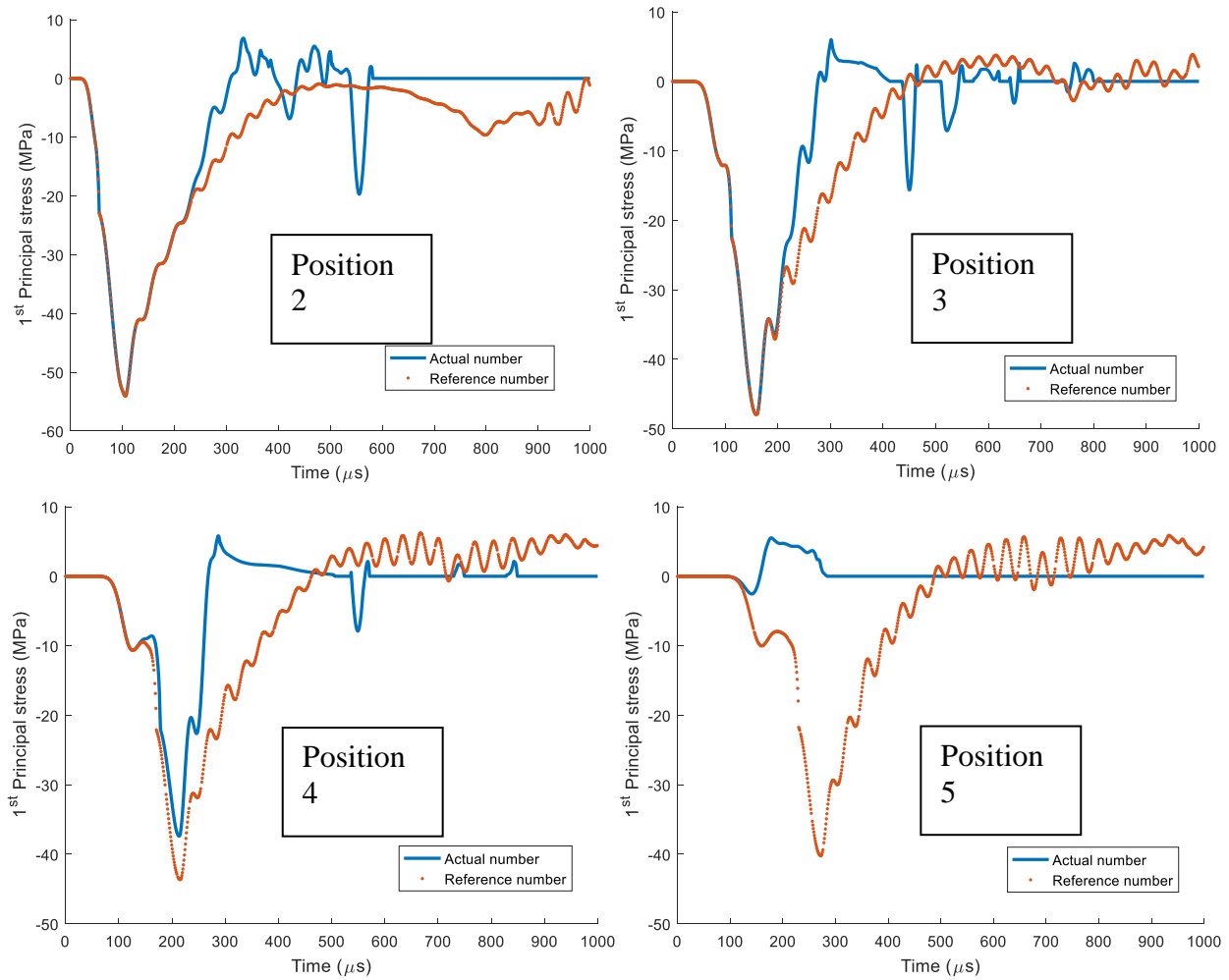
Figure 32: Open boundary case principal stresses comparison.

As in Figure 32, position 5 at the exterior boundary is influenced the most by the reflection while the stresses at positions 1 to 4 are all alleviated by the reflected tensile wave. Specifically, at position 5, the reflected tensile waves are superimposed by the remaining incoming compressive waves, therefore the 3rd principal stress is reduced when comparing to the reference results. On the other hand, the 1st principal stress changes from compression to tension, and this is because the blast wave push the exterior layer of the tunnel lining and resulted in in-plane tensile stresses. It is worth mentioning that the out of plane direction has almost no tensile stress and the reason for damage at position 5 is in-plane stresses, 1st and 2nd principal stresses.
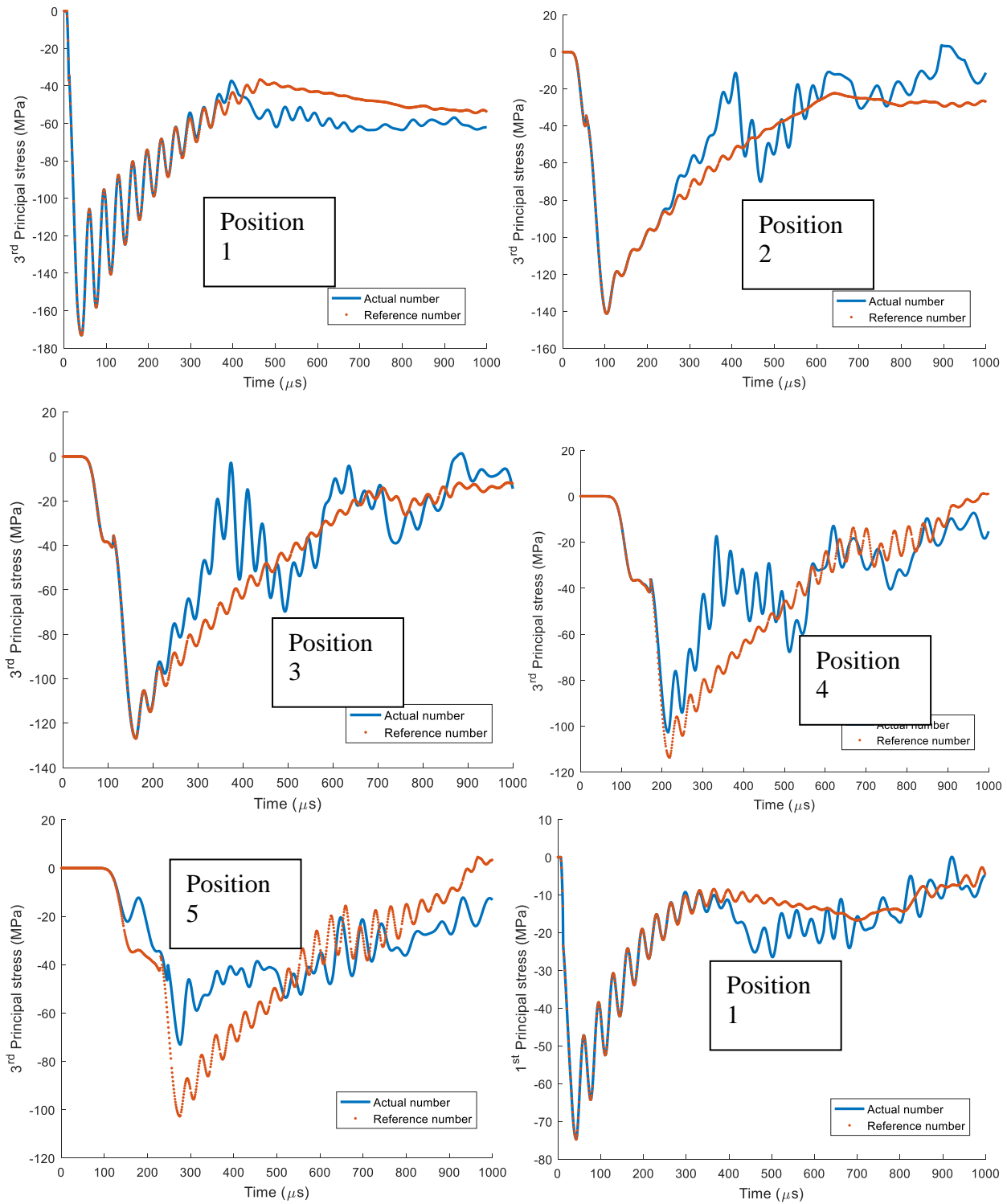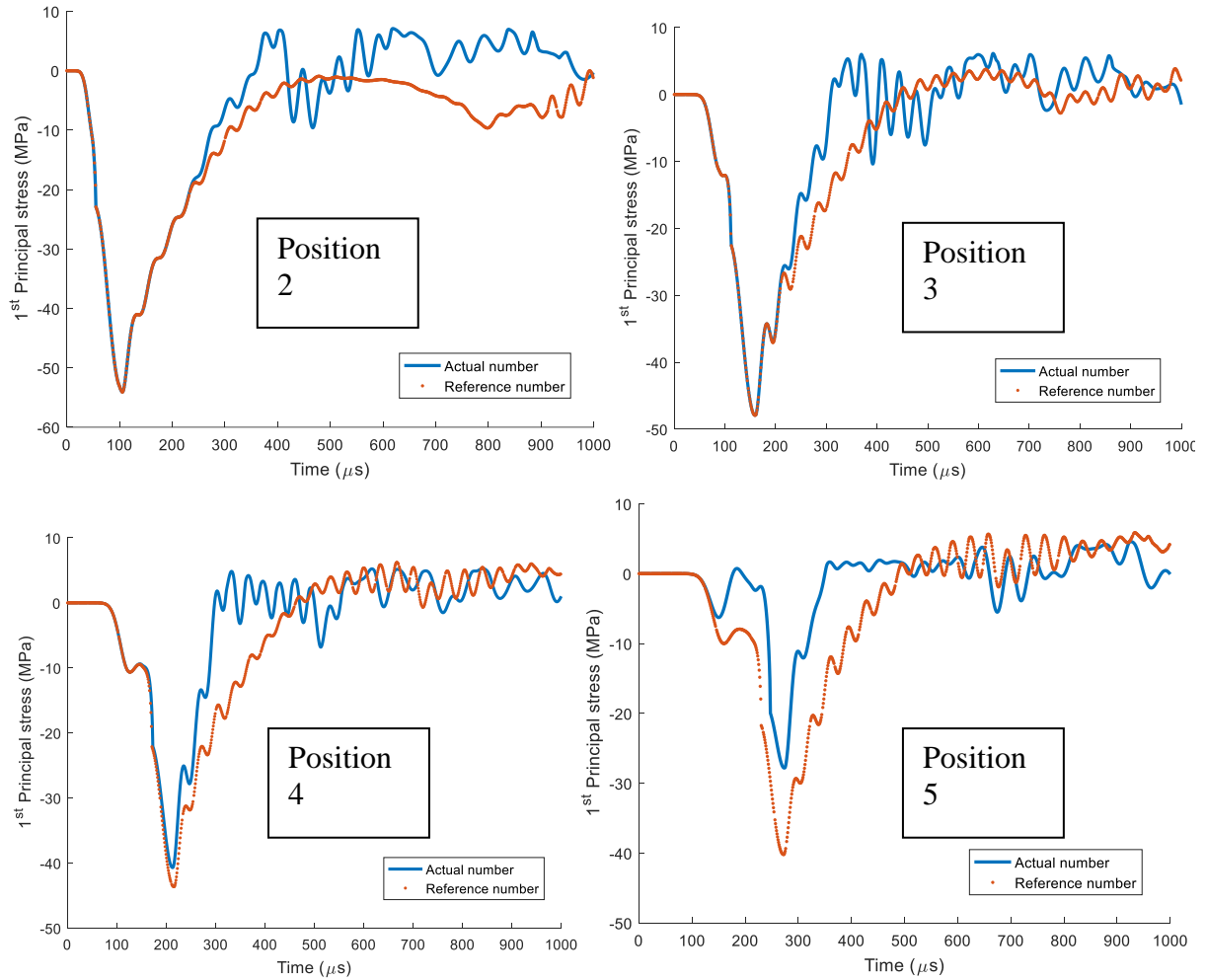
Figure 33: Subgrade case principal stresses comparison.

As in Figure 33, although the stresses at all five positions are reduced by the reflected tensile wave, the position 5 is influenced the most. All stresses at all positions are in compression and especially when comparing to the open boundary case. This is why such a subgrade will avoid damage efficiently. As already demonstrated in Figure 32 and Figure 33, position 5 is the critical point for different cases. To further compare the results, the results at position 5 for various cases are further compared.
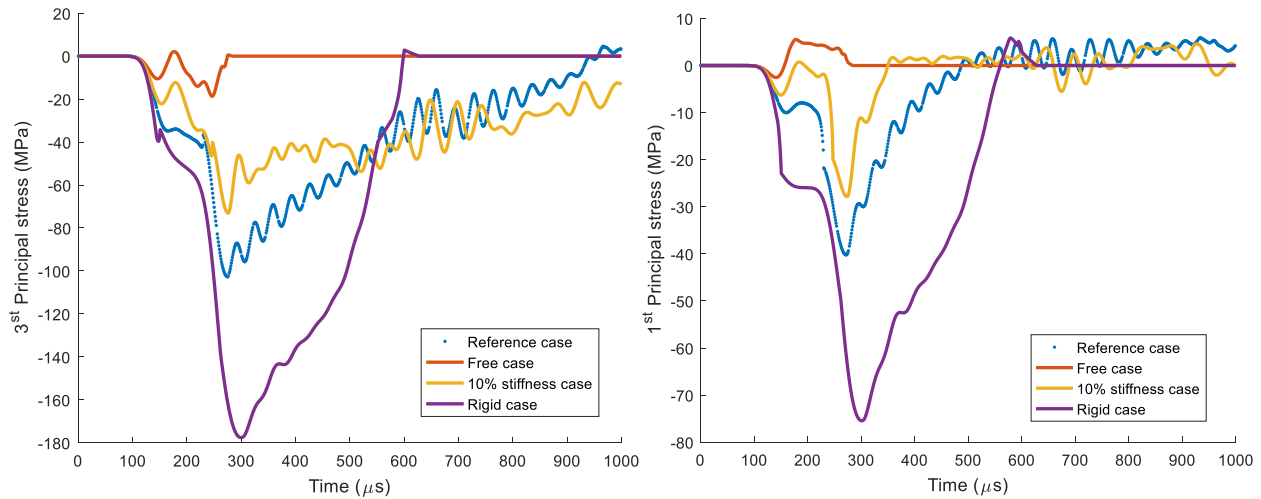
Figure 34: Principal stresses comparison.

Again, the reference case is the tunnel liner that has infinite thickness. As in Figure 34, the free boundary case has minimum 3rd principal stress at the exterior position while the rigid boundary case has maximum 3rd principal stress at the same position, which is almost as big as twice of the reference case. The 10% stiffness case has significantly higher 3rd principal stress than the free boundary although the stiffness is only increased 10% of the concrete linings from the free boundary case. Similarly distribution can be found in the 1st principal stress except the free boundary case has tension instead of compression. This is actul the reason that concrete linings at the free boundary fracture. To demonstrate the damage process, effective pressure, pressure and damage index are plotted together for the free and rigid boundary cases.
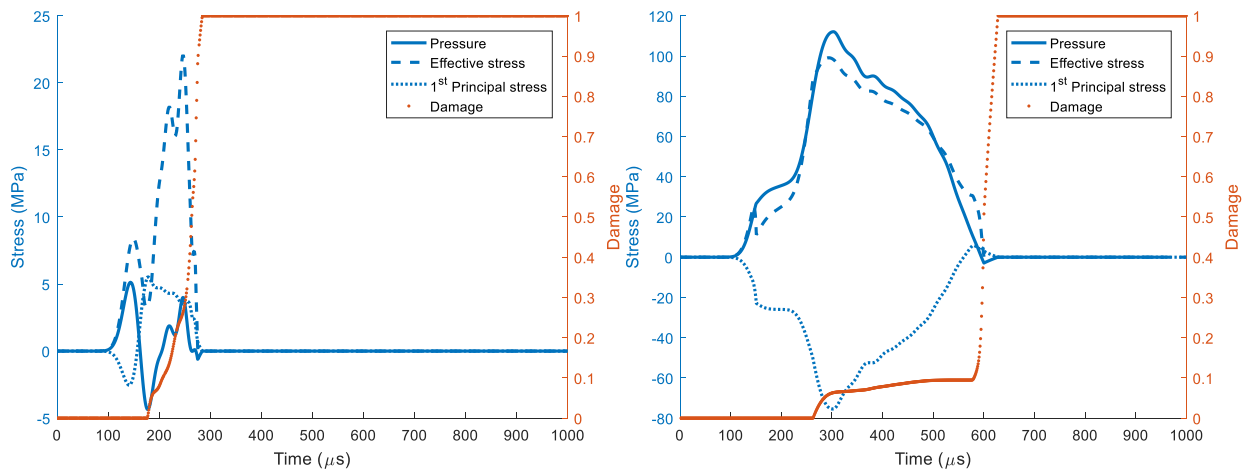
Figure 35: Damage evolution of the free boundary (left) and fixed boundary (right) cases.

As shown in Figure 35, the two cases have very different failure mechanism. For the 10% stiffness subgrade case, the damage occurs as the first principal stress becomes tensile (Pressure drops) and effective stress remains whereas for the rigid case damage accumulates as pressure, 1st principal stress and effective stress increase significantly. Thus, the free boundary tends to induce tensile damage on the lining's exterior position whereas the fixed boundary tends to induce compressive damage at the same position.
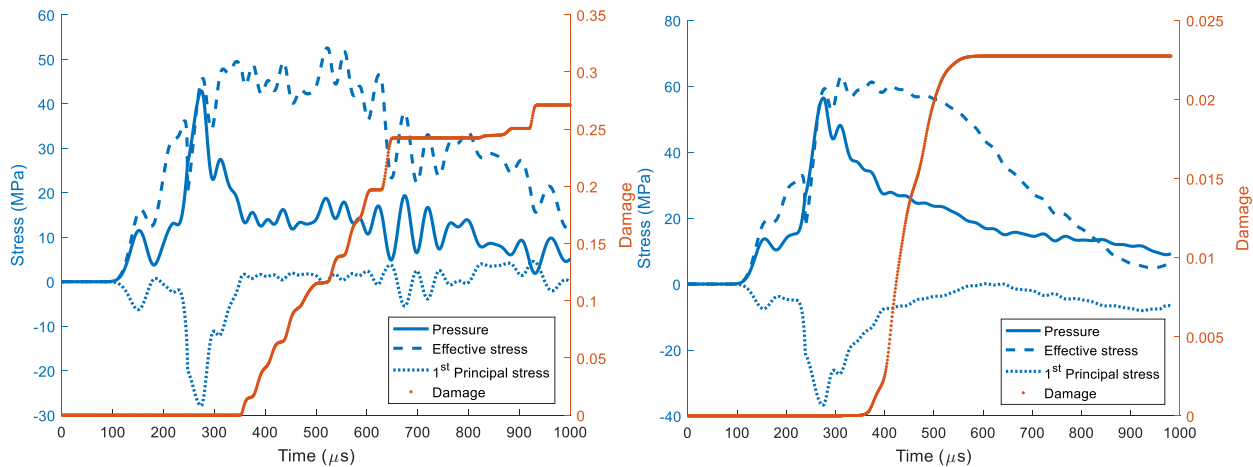
Figure 36: Damage evolution of the 10% stiffness (left) and 30% stiffness (right) subgrades cases.

In Figure 36, position 5 is no longer fully damaged. For the 10% stiffness subgrade case, the damage reaches about 27% whereas the same point only has 2.3% damage for the 30% stiffness subgrade case. Furthermore, unlike the complete damage either by tension or compression in Figure 35, the damage occurs when this position is in a state of combined shear and pressure. However, it is worth mentioning that in both cases the onset of damage follows the sudden drop of pressure and stops when effective stress drops below a threshold.

Summary Results of Blast Assessment

As presented in Chapters 5 and 6, the blast demand from contact and close-in detonations of high explosives results in localized spall and breach of the concrete tunnel liner. The damage to the tunnel liner is dependent on the stiffness of the substrate material used behind the tunnel liner. A substrate material with similar impedance as the concrete liner will exhibit less damage while the case of an unbacked tunnel liner would result in the highest damage. The unbacked liner case is academic and does not represent a real-world scenario but is used to examine the sensitivity to damage. For the case of an impedance match between the liner and substrate, the stress wave generated by the blast event will continue into the substrate and will not reflect. The lack of reflection will eliminate the occurrence of a tensile reflective stress wave on the exterior of the liner, thereby reducing the overall damage to the tunnel.

As illustrated in this chapter, the tunnel liner damage will be primarily on the exterior in the region adjacent to the substrate and less on the interior visible surface. The exterior of the tunnel is not visible nor can it be readily inspected using visual means. Damage to this region can conceptually be inspected using currently available non-destructive ultrasonic or ground penetrating radar methods. The damage to the exterior of the liner could result in eventual degradation due to water intrusion and corrosion of the reinforcement; however, the damage would be limited to the localized region impacted by the blast event. The main concern from a strength perspective would be if the liner is breached and the liner is subjected to significant ground water or is part of a submerged tunnel. For these cases, the blast event could result in water intrusion and possibly progressive damage of the tunnel liner. This specific case may deserve further examination and is studied further in the resilience effort conducted in Task 2 of this research program.

The main result of the work presented in these chapters is that the damage to the tunnel liner from close-in detonations is significantly influenced by the impedance mismatch between the concrete tunnel liner and the substrate. The presence of similar impedance can minimize damage; however, for substrate materials that have considerably different impedance (i.e., very small impedance or greater than twice that of the liner), damage will rapidly increase. To minimize damage to the tunnel liner, a substrate grout that has similar impedance properties (stiffness and density) to the tunnel liner could be used. This will move the location of damage due to wave propagation to the outer edge of the grout layer and away from the structural tunnel liner. This approach can be used for all tunnel liners used for underground transportation. This approach is not viable for submerged tunnels where the system is surrounded by water. For these applications special attention should be made to minimize the possibility of breach. Based on these findings, an experimental study is not warranted and is therefore not pursued.

Chapter 7: Streamlined Calculation of Fire-Induced Heat Flux and Resulting Spall Damage for Concrete Tunnel Linings

To examine the sensitivity of tunnel liners to vehicular fires, a quick running computational tool is developed. The tool makes use of a confined discretized solid flame (CDSF). The model is calibrated with high fidelity simulation (FDS) numerical analyses which in turn were validated with experimental tests. The tool is outlined in this chapter and is used to illustrate the level of damage likely from fire events. The results presented in this chapter are adopted from a published conference paper by the authors (Guo et al. 2019). This research is presented in more detail in Task 2 conducted by the Lehigh University UTC-UTI team in year 1 and 2.

Tunnel Prototypes and Fire Scenarios

A representative comparison between the CDSF and FDS models is performed for three fire scenarios in a circular tunnel that utilizes the same cross-section previously investigated by the authors for tunnel blast damage (Bai et al. 2018) and illustrated in Figure 37. The circular cross-section is used in this study as an acknowledgement of the increased use of boring machines to develop new tunnels in the US (Jianbin Li 2017). Other cross-section shapes such as horseshoe, which are common in the current US tunnel inventory, will also be investigated in future work. Only the portion of the tunnel liner above the road deck is included because the portions below will not be exposed to a vehicle fire. The authors intend to generalize this approach to a range of cross-section shapes in future phases of this project. The size of this cross-section is representative of a two-lane throughput with a shoulder and has similar overall dimensions to the experimentally tested tunnel used for FDS validation (Root et al. 2018). For simplicity, the fire location is assumed at the longitudinal and transverse center of the tunnel – future work will adapt the approach shown here for fires at any location, longitudinal or transverse, within the tunnel.
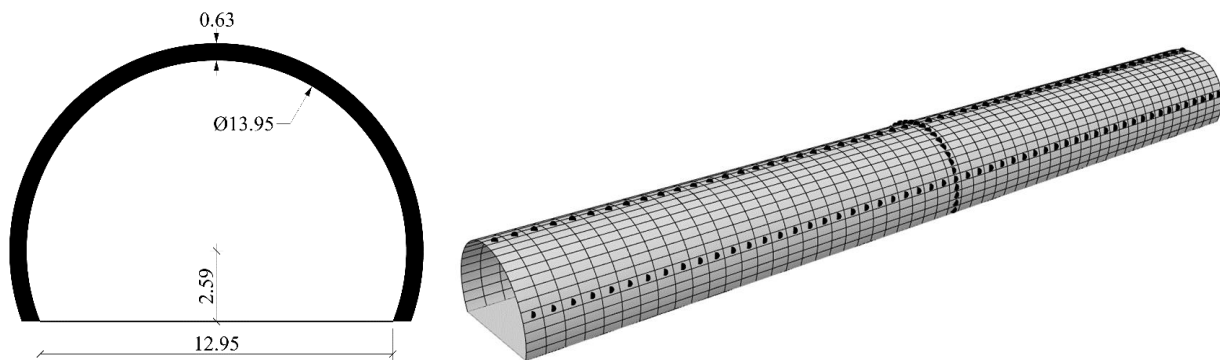
Figure 37: Cross section dimensions (in meters) and isometric profile of the circular tunnel.

Three types of vehicular fire scenarios are considered: bus, light heavy goods vehicle (HGV) and heavy HGV with heat release rates (HRR) of 30 MW, 70 MW and 200 MW, respectively (Association 2011). In reality, these fires would include combustion of multiple materials such as hydrocarbon fuel, lubricants, plastics, foams, wood, etc. Estimating the aggregate combustion properties of these materials, which are needed to calculate the geometry and intensity of the resulting fire, is difficult due to variability and limited availability of data such as mass loss rate and heat of combustion. Rather than modeling the combustion of the various materials that comprise the vehicle and its contents and/or cargo, a diesel pool fire with equivalent HRR is defined as the fire source in both the FDS and CDSF models. Semi-empirical expressions for the

severity and geometry of hydrocarbon pool fires are well established from decades of previous research by others, and combustion properties are readily available in the published literature. The use of an equivalent diesel pool fire for evaluating the tunnel liner under fire is analogous to the use of equivalent weights of TNT for an evaluation of blast effects (Department of Defense (DoD) 2014, 340). Future phases of this project will explore the implementation of combustion properties and fire characteristics which more closely correspond to the vehicle contents.

Most of the semi-empirical equations for calculating pool fire characteristics are based on a circular pool shape – similar expressions for non-circular pool fires are not widely available. To make the diesel pool fire representative of the vehicle design fires, a rectangular footprint is used for this study. Since the pool fire diameter is a required variable for most semi-empirical calculations, an equivalent value $D_{f,eff}$ (m) based on the area of the rectangular footprint can be obtained using Eq. 1:

$$D_{f,eff} = \begin{cases} \sqrt{\dfrac{4A_f}{\pi}} & for\ 0.5 \leq \dfrac{L_f}{W_f} \leq 2 \\[2em] \sqrt{\dfrac{4\left[2 \cdot \min(L_f, W_f)^2\right]}{\pi}} & otherwise \end{cases} \tag{1}$$

L_f (m) and W_f (m) represent the length and width of the fire footprint. For pool fire footprints with an approximate aspect ratio (long edge to short edge) greater than 2, the $D_{f,eff}$ is calculated by limiting the pool fire area, A_f, (m^2) to a rectangle with dimensions of the short edge by two times the short edge. Previous studies have indicated that using $D_{f,eff}$ for areas with aspect ratios greater than 2.5 may lead to inaccuracy when using the semi-empirical equations based on circular pools (McGrattan, Baum, and Hamins 2000). The maximum heat release rate (HRR), $\dot{Q}_{f,max}$ (kW), of the pool fire can then be calculated as follows (Babrauskas 2016):

$$\dot{Q}_{f,max} = \dot{m}"\Delta H_{c,eff} A_f \left(1 - e^{-k\beta \cdot D_{f,eff}}\right) \tag{2}$$

where $\dot{m}"$ is the mass loss rate per unit area (kg/(m^2-s)), $\Delta H_{c,eff}$ is the effective heat of combustion (kJ/kg), and $k\beta$ is the empirical constant (m^{-1}). These variables are fuel specific and can be obtained from standard references for diesel (Siddapureddy 2013).

Figure 38 shows the actual vehicle footprint (dashed) given by AASHTO (American Association of State Highway and Transportation Officials 2001) for the bus, light HGV, and heavy HGV. To maximize flame height for the specified heat release rate of each vehicle, an equivalent diesel pool footprint was developed with an aspect ratio of 2 and a pool fire area A_f that satisfies Eq. 2 for diesel. These equivalent footprints are shown as solid black outlines in Figure 38 for the three fire scenarios. Due to the semi-empirical constraints of Eq. 2, the area of the equivalent diesel footprint is 64% and 22% smaller than the vehicle footprint for the 30 MW and 70 MW fires, and 29% larger for the 200 MW fire. By ensuring maximum flame amplitude, the equivalent diesel footprints are used as a conservative basis for the fires analyzed in both FDS and the CDSF model for this study. Analyses with pool fire footprints that more closely resemble the aspect ratio of the full vehicle footprint will be examined in future work.
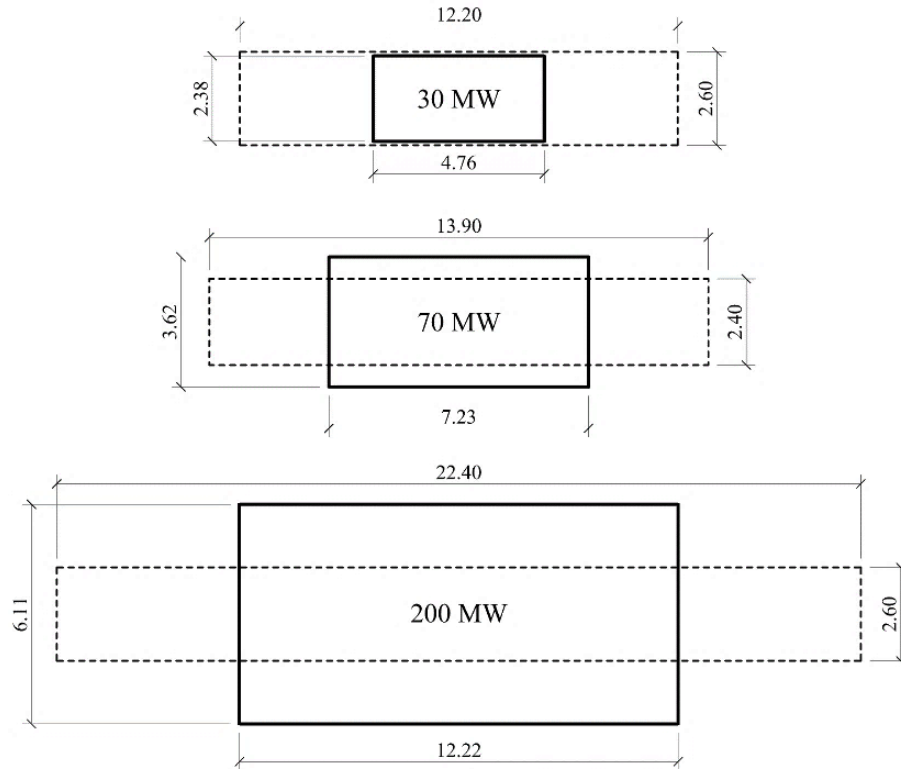
Figure 38: Dimensions (in meters) of actual vehicle footprints and equivalent diesel pool footprints

Computational Validation Models

The primary output of the CDSF model is a spatial contour of total heat flux over the exposed faces of the tunnel liner due to a severe fire. Direct experimental validation of total heat flux is not feasible since most full-scale experimental tests of tunnel fires to date have focused on temperature distributions, combustion dynamics, and smoke movement. Temperature data from a full-scale tunnel fire test program performed in the Memorial Tunnel in West Virginia, USA (Bechtel / Parson Brinckerhoff 1995) is therefore used to validate a corresponding model in FDS. The validated FDS model is adapted to a prototype tunnel of similar size as the Memorial Tunnel for several design fire scenarios. While the Memorial Tunnel has a slope angle of 3.2%, the prototype tunnel is modeled with no slope to eliminate the influence of gravity on longitudinal smoke movement. With this simplification, the current CDSF model is thereby calibrated for natural ventilation conditions. Total heat flux results from FDS simulations are then used to computationally calibrate the CDSF approach.

Two tests from the Memorial Tunnel program without a forced ventilation system (Nos. 501 and 502) were selected as the basis for developing a validated FDS model for a large-scale fire. The tests had target heat release rates (HRR) of 20 MW and 50 MW and used diesel as the fuel. The fire source was modeled in FDS as a rectangular pool whose area and heat release rate per unit area (HRRPUA) were defined to achieve the same HRR as in the experiment. The reaction properties such as radiative fraction and soot yield of diesel are defined according to preexisting

experimental data. Soot yield is taken as 0.1 for diesel (Siddapureddy 2013) and radiative fraction, χ_{rad} is calculated according to Munoz et al. (Muñoz et al. 2007) as a function of $D_{f,eff}$ (m):

$$\chi_{rad} = \begin{cases} for\ D_{f,eff} \leq 5m: & 0.158 D_{f,eff}^{0.15} \\ for\ D_{f,eff} > 5m: & 0.436 D_{f,eff}^{-0.58} \end{cases} \tag{3}$$

An in-depth discussion of the FDS validation has been previously presented by the authors (Root et al. 2018). Ceiling temperatures from FDS, taken at the same point in time as the experiment, compare well with test data for both fire sizes as shown below in Figure 39.
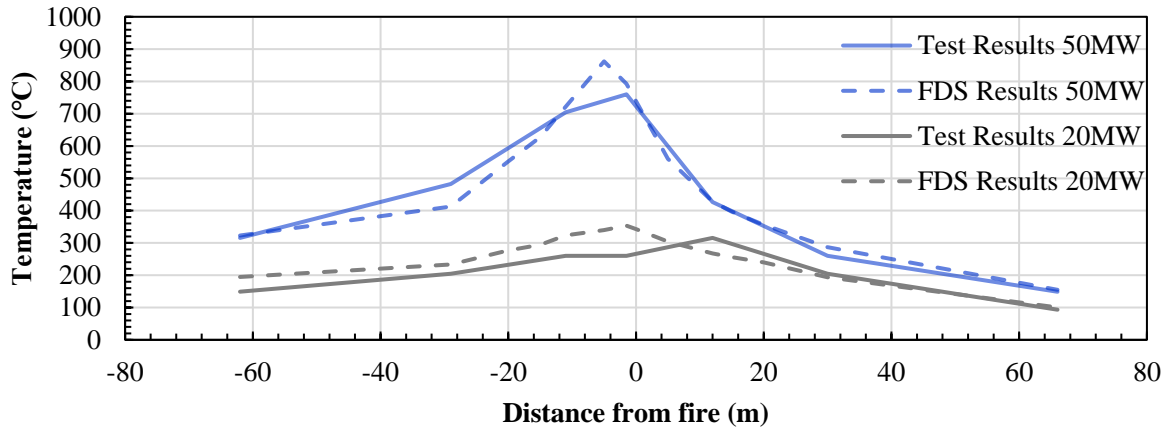
Figure 39: Comparison of experimental and FDS ceiling temperatures during the 20 MW and 50 MW diesel test fires in the Memorial Tunnel (Bechtel / Parson Brinckerhoff 1995)

The FDS analyses were performed on a personal computer with quad-core i7 processor, 16 GB of RAM, and an SSD hard drive. Analysis of a 200-second duration for the 50 MW fire required 13 hours of computational time with parallel processing and full system dedication. The simulation produced 1.6 GB of data, even though only a limited number of locations were recorded for temperature and heat flux. Long runtimes and data density hinders the practicality of using FDS for design processes or stochastic analysis of multiple scenarios or multiple tunnel parameters, which further highlights the necessity for a more efficient approach to predict thermal demands.

Using the experimentally validated approach, FDS analyses were then performed for the prototype tunnel in Figure 37 for all three fire scenarios. Due to the density of FDS data, strategic measurements of total incident heat flux were made at increments ranging from 2- to 5-m along the ceiling and the sidewall as shown with the black dots in Figure 37. Time histories of heat flux, which reflect realistic turbulence of the combustion reaction, were obtained at every target for comparison to the CDSF results.

Confined Discretized Solid Flame (CDSF) Model

The CDSF is a radiative and convective hybrid model for calculating total incident heat flux on the surface of a tunnel liner due to fire. As a first step in developing the radiation model, a solid flame shape, known as the free flame, is generated without consideration of tunnel confinement. If the calculated free flame height extends beyond the confines of the tunnel geometry, the shape is compressed and becomes confined to the tunnel, thereby regarded as the confined flame shape. The flame shape, either confined or free, is then appropriately discretized for analysis and denoted as the analytical flame, for which an emissive power is assigned to each discretized surface. Each

target surface on the tunnel lining receives straight-line radiation from each discretized solid flame element. An approximate convective region is then defined along the tunnel ceiling to account for additional thermal demands from smoke and ceiling jets. The summation of these radiative and convective effects, illustrated below in Figure 40, is calculated and visualized for all elements in the tunnel liner mesh.
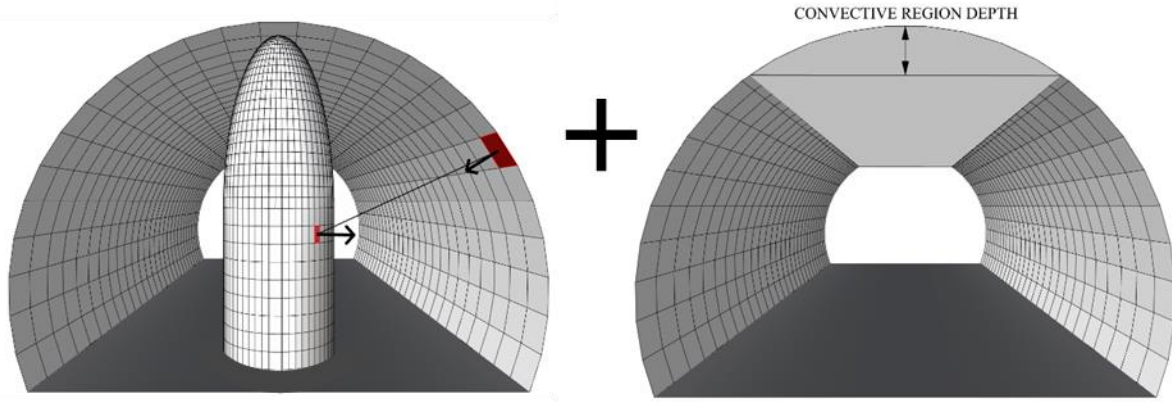
Figure 40: Radiative and convective heat transfer illustrations for the CDSF model.

All geometric modelling and calculation is performed using Rhino and Grasshopper, thus allowing for continuous, analytical flame shapes and rapid visualization of thermal demands. The rectangular, equivalent diesel footprints shown in Figure 38 are first converted to an equivalent elliptical footprint in order to remove sharp edges (and potential radiative "blind spots") when the solid flame shape is extruded. The analytical elliptical footprint has the same perimeter as the rectangular equivalent diesel footprint, limited to an aspect ratio of 2.0. The height of the free flame, H_f (m), is calculated as a function of the peak heat release rate, $\dot{Q}_{f,max}$ (kW) and effective diameter, $D_{f,eff}$, (from Eqs. 1 and 2) via Heskestad's correlation (Hurley 2016):

$$H_f = 0.235\dot{Q}_{f,max}^{0.4} - 1.02D_{f,eff}$$

(4)

The final form of the free flame is shown in Figure 41. The height of the flame is proportioned in accordance with previous work by Zhou et al. (K. Zhou et al. 2014), in which the solid flame is bifurcated into a cylindrical body and a cone (representing the realistic taper of the flames) at $0.4H_f$ from the base of the flame. To again avoid discontinuities in the solid flame shape, the cone (above $0.4H_f$) is replaced with a truncated ellipsoid dome, and the body (below $0.4H_f$) is a uniform extruded ellipse. The flame emissive power (in kW/m^2) is assumed to be uniform across the surface of the free flame – it is calculated as a function of the radiative fraction, χ_r (from Eq. 3), peak heat release rate, $\dot{Q}_{f,max}$ (from Eq. 2), and free flame surface area A (m^2) (McGrattan, Baum, and Hamins 2000):

$$E = \frac{\chi_r \, \dot{Q}_{f,max}}{A}$$

(5)

As shown in Figure 41, the height of the fire's base above the road surface, H_{base} (m), approximately accounts for the height of the bottom of the vehicle (0.5 m for bus and 1.0 m for HGV). If the height of the free flame H_f from Eq. 4 plus H_{base} remains below the tunnel height

(minus a small ceiling offset, specified for this study as $0.02H_f$), then H_f is used as the analytical flame height. However, the free flame height from Eq. 4 will often exceed the height of the tunnel for significant fires. In those cases, the analytical flame height is reduced to fit inside the tunnel enclosure, thus *confined*. To allow the flame surfaces to have adequate view of the tunnel liner at close range and "engulf" those targets with appropriately high radiation heat flux, the top of the ellipsoid dome is restricted to the offset of $0.02H_f$ from the tunnel ceiling height. The confined flame height, H_c, (m) is therefore calculated as follows:

$$H_c = H_T - 0.02H_f - H_{base}$$

(6)

For free flame heights that just exceed the tunnel height, the ellipsoid dome is simply compressed as shown in Figure 41 while the height of the extruded ellipse body remains at $0.4H_f$. As the free flame height increases for increasingly severe fires, the body height can become so large that the ellipsoid dome would be unrealistically compressed or even eliminated (resulting in poor analytical calculations of radiation heat flux on the ceiling) if no height adjustments were made to the body. To preserve the bifurcated structure of the confined solid flame, the height of the confined flame body can be no greater than 75% of H_c, and the ellipsoid dome can therefore be no less than 25% of H_c.
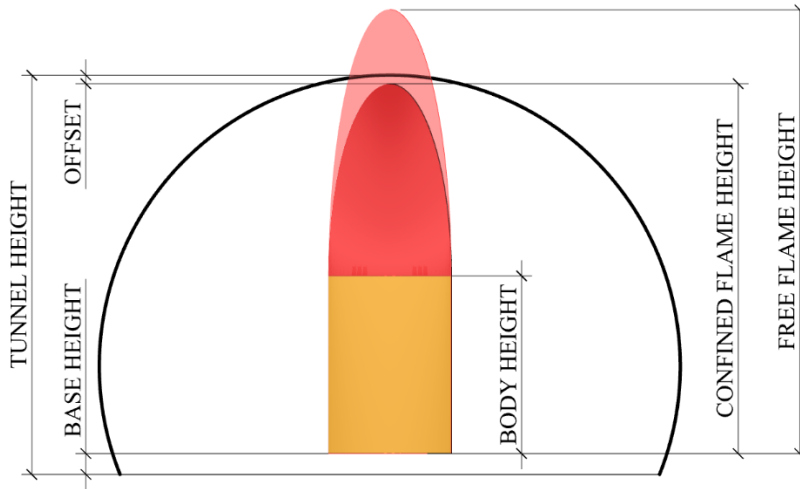
Figure 41: Schematic comparison of the free flame and confined flame models in the tunnel cross-section

Conservation of energy is preserved when free flame shapes that extend beyond the tunnel height are compressed to create the confined flame shape, which will naturally have less surface area. Since the ellipsoid dome and extruded ellipse body will experience different amounts of surface area reduction, the average emissive power over the free flame surface area, E in (kW/m^2) from Eq. 4 is amplified by the ratios shown below in Eqs. 7 and 8 for the body and dome of the confined flame, respectively:

$$E_b = E\left(\frac{A_b}{A_b'}\right) * C$$

(7)

$$E_d = E\left(\frac{A_d}{A_d{'}}\right) * C \qquad (8)$$

A_b and A_d (both in m^2) are the surface areas of the free flame body and dome, and $A_b{'}$ and $A_d{'}$ (again in m^2) are the areas of the confined flame body and dome, respectively. Surface emissive power in the body, E_b (kW/m^2) and surface emissive power in the dome, E_d (kW/m^2), are applied to the analytical flame body and dome, respectively. Additionally, when the free flame height far exceeds the tunnel height and the body height is restricted to 75% of H_c, the average emissive power, E, is increased by an additional confinement factor, C, to account for increased combustion efficiency and turbulence resulting from significant confinement of the flame (Wang et al. 2017). For this study, C is taken as the ratio of A_b to $A_b{'}$. Note this value equals unity for free flame body heights not exceeding 75% of H_c. As will be shown later in this paper, this approach to energy conservation between the free and confined solid flame models can accurately capture the magnitude and distribution of radiation heat fluxes that are expected with increasing fire size as compared to the FDS solutions. Preliminary studies have indicated a maximum edge distance of 85 cm in the analytical flame mesh provides an acceptable level of resolution and convergence.

The CDSF model includes a convective field at the upper region of the tunnel cross-section to conservatively capture the heat flux contributed by the ceiling jet and smoke effects. The depth of the convective zone below the tunnel ceiling is scaled linearly with peak heat release rate. Kurioka et al. determined a power scaling fit for longitudinal temperature decay in the smoke filled region that accumulates under a tunnel ceiling (Kurioka et al. 2003). The convective heat flux is also scaled linearly over the vertical depth of the convective zone according to Hu (L. H. Hu et al. 2004), who noted a strong correlation between smoke temperature and distance below tunnel ceiling. Using an FDS-informed fit correlated to peak heat release rate and tunnel size, a similar model has been developed for the maximum convective heat flux as well as its longitudinal and vertical decay under the tunnel ceiling (Root 2018). By combining radiative and convective effects, the spatial distribution of total incident heat flux is mapped to the discretized tunnel liner, as shown in the section cut below in Figure 42.
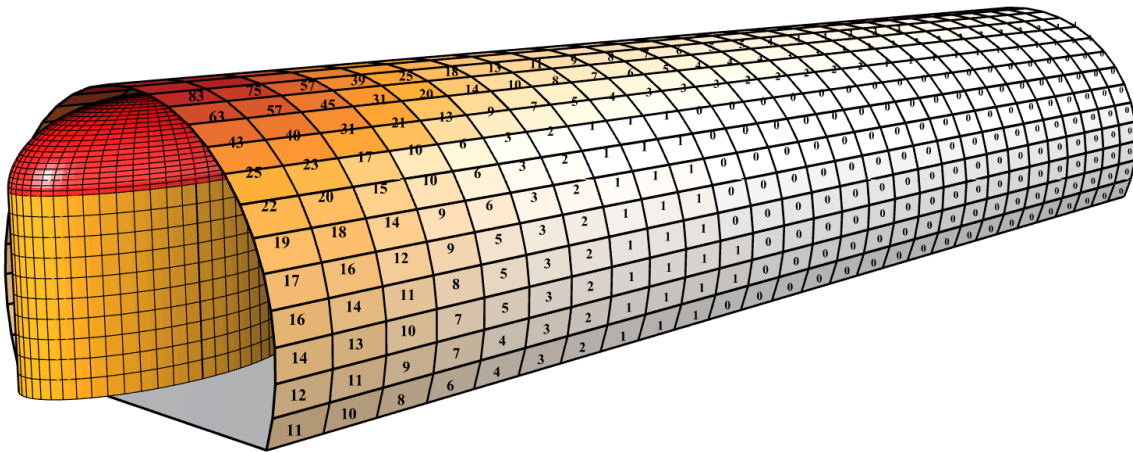
Figure 42: Section cut at the longitudinal center showing typical CDSF output (heat flux in kW/m^2)

Comparison and Discussion

Heat flux results from the CDSF and FDS models for the three fire sizes in the prototype tunnel are compared at the locations marked with black dots in Figure 37 along the ceiling, sidewall and cross-section. While the CDSF output provides a single heat flux value at each target location, FDS provides a heat flux time history at the selected measurement points. The time history of heat fluxes (solid) shown below in Figure 43 are those directly measured at the ceiling location above the fire in FDS for each scenario. Oscillation is exhibited for all three fire sizes, with the 200 MW fire showing the most fluctuation and a slight drop at about 230 seconds. The 200 MW fire generates much more smoke and higher gas flow rates compared to the smaller fires, making its resulting heat flux output more turbulent. To appropriately compare the FDS and CDSF results, an upper and lower bound of the FDS time histories are determined statistically. In this study, the mean heat flux +/- one standard deviation is selected and plotted as dashed lines in Figure 43 against the heat flux time histories. Upper and lower bound time histories start with a 30-second t^2 ramp up to a constant heat flux and remain at that value for the duration of the fire.
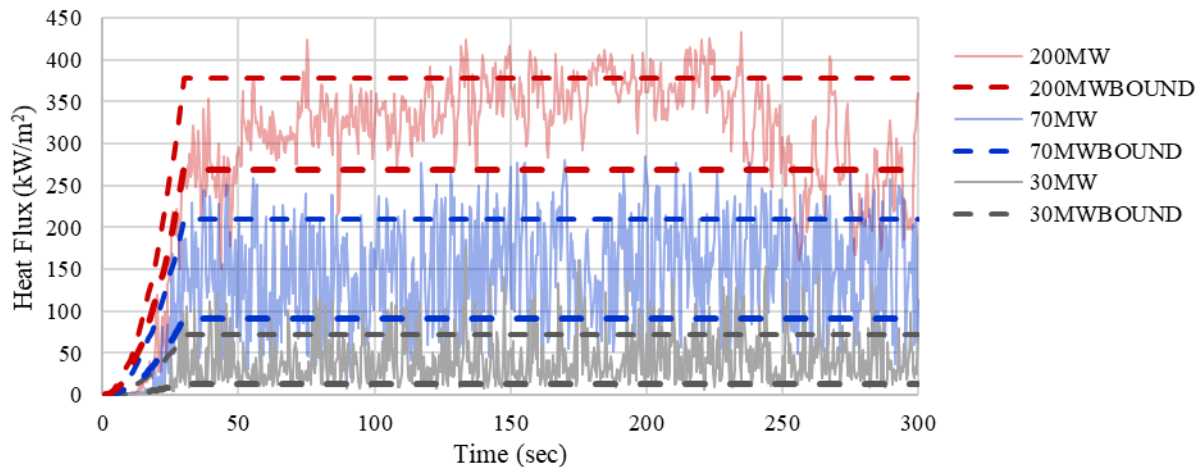
Figure 43: Heat flux time histories with upper and lower bounds for the three fire scenarios.

When considering thermal effects on tunnel occupants in the event of a tunnel fire, it may be appropriate to consider only peak values of thermal demands. However, the case is different when evaluating the structural consequences caused by their cumulative duration of exposure. Through-thickness temperature gradients are important in characterizing the structural response of concrete in fire for resulting spalling and/or cracking damage (Le et al. 2016). Therefore, the selection of the mean heat flux +/- one standard deviation as the upper and lower bounds is justified by comparing thermal analyses of the tunnel liner thickness for the two bounding curves against the actual turbulent time history in Figure 43. The tunnel liner, with a thickness of 630 mm per Figure 37, is discretized into 100 layers through its thickness, and used in a 1-D heat transfer analysis. The concrete is assumed to have density of 2300 kg/m³ and moisture content of 46 kg/m³. Utilizing SAFIR (Franssen and Gernay 2017), each heat flux time history is applied on one face of the concrete panel, and temporal temperature gradients are calculated. All time histories are analyzed with a constant 1-second time step, which is sufficiently small based on preliminary calculations and is smaller than the minimum time step from the FDS analysis. Ambient temperature is applied as a thermal boundary condition to the unheated face, which in accordance with Eurocode 1 is assigned a relative emissivity of 0.5 and a convective coefficient of 4 kW/m² (EUROPEAN COMMITTEE FOR STANDARDIZATION 2002). The concrete is defined as SILCONC_EN (i.e.

siliceous concrete) in SAFIR, and the thermal properties are assumed according to Eurocode 2 (CEN 2008, 2).

Figure 44 compares the temperature gradients into the concrete liner within the first 5 minutes of fire exposure at two ceiling locations: (1) directly above fire, and (2) 20 meters from fire. The Figure 44 dashed lines represent the upper and lower bound flux histories, and the solid lines represent the more complex FDS heat flux time history. The results are presented for the three fire cases and presented at three points in time: 50, 150 and 250 seconds. The results show that the upper and lower bound solutions bracket the thermal gradient calculated from the raw FDS results. Once the fire becomes fully developed, the FDS results trend toward the mean value between the upper and lower bound. These bounding values will be used to evaluate the CDSF modeling results for the remainder of this paper.
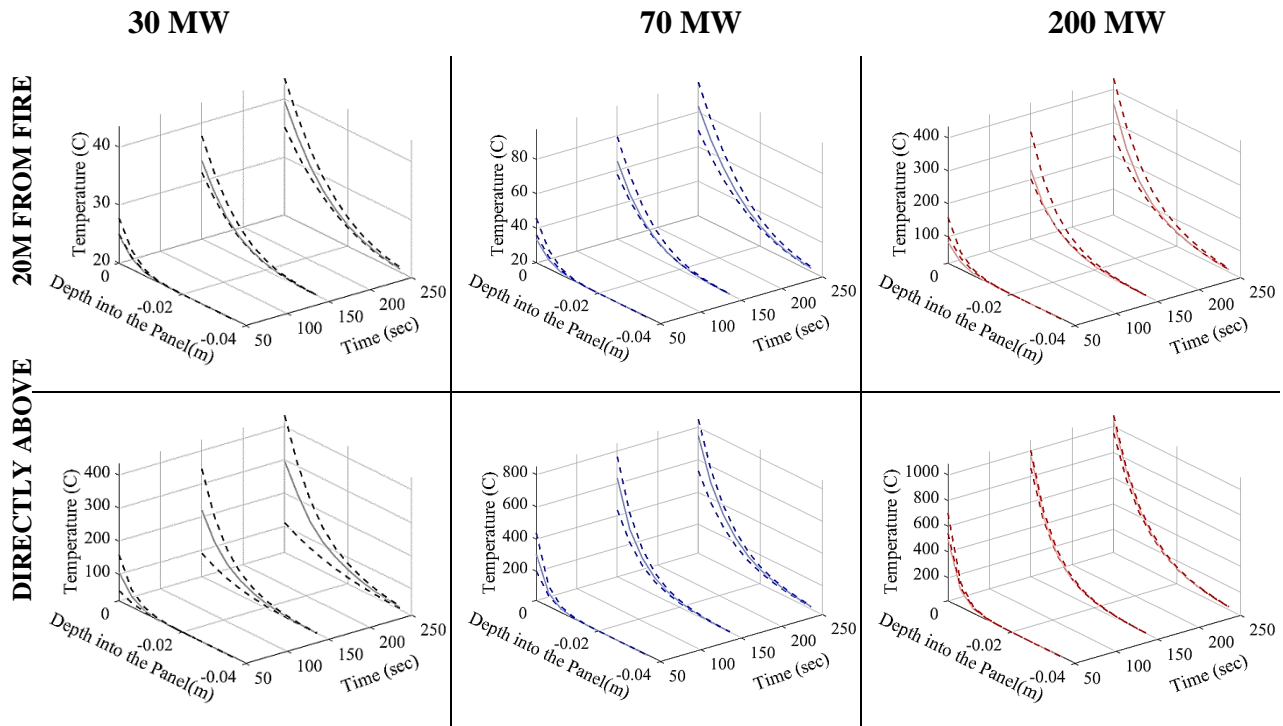
Figure 44: Comparison of through-thickness temperature gradients at two ceiling locations.

The comparison between the FDS and CDSF results at the locations specified in Figure 37 are shown below in Figure 45 and Figure 46. In Figure 45, the solid red lines represent the upper and lower bounds of the FDS solution at the ceiling, and the red dashed line is the mean value taken after 30 seconds. The blue lines represent a similar breakdown of FDS results for the sidewall. In Figure 46, the region between the upper and lower bound FDS solutions is shaded in red. The CDSF provides a robust and accurate calculation of heat fluxes at various locations within the tunnel for the different fire sizes. The "bump" at the ceiling shown in the 70 MW and 200 MW cross-section comparisons indicates a fully developed convective zone, which is accurately captured by the CDSF. CDSF predictions also come at a fraction of the computational effort compared to that of FDS solutions, needing just under 4 minutes to complete compared to 13 hours for FDS simulations on equivalent desktop workstations for the same duration of fire exposure.
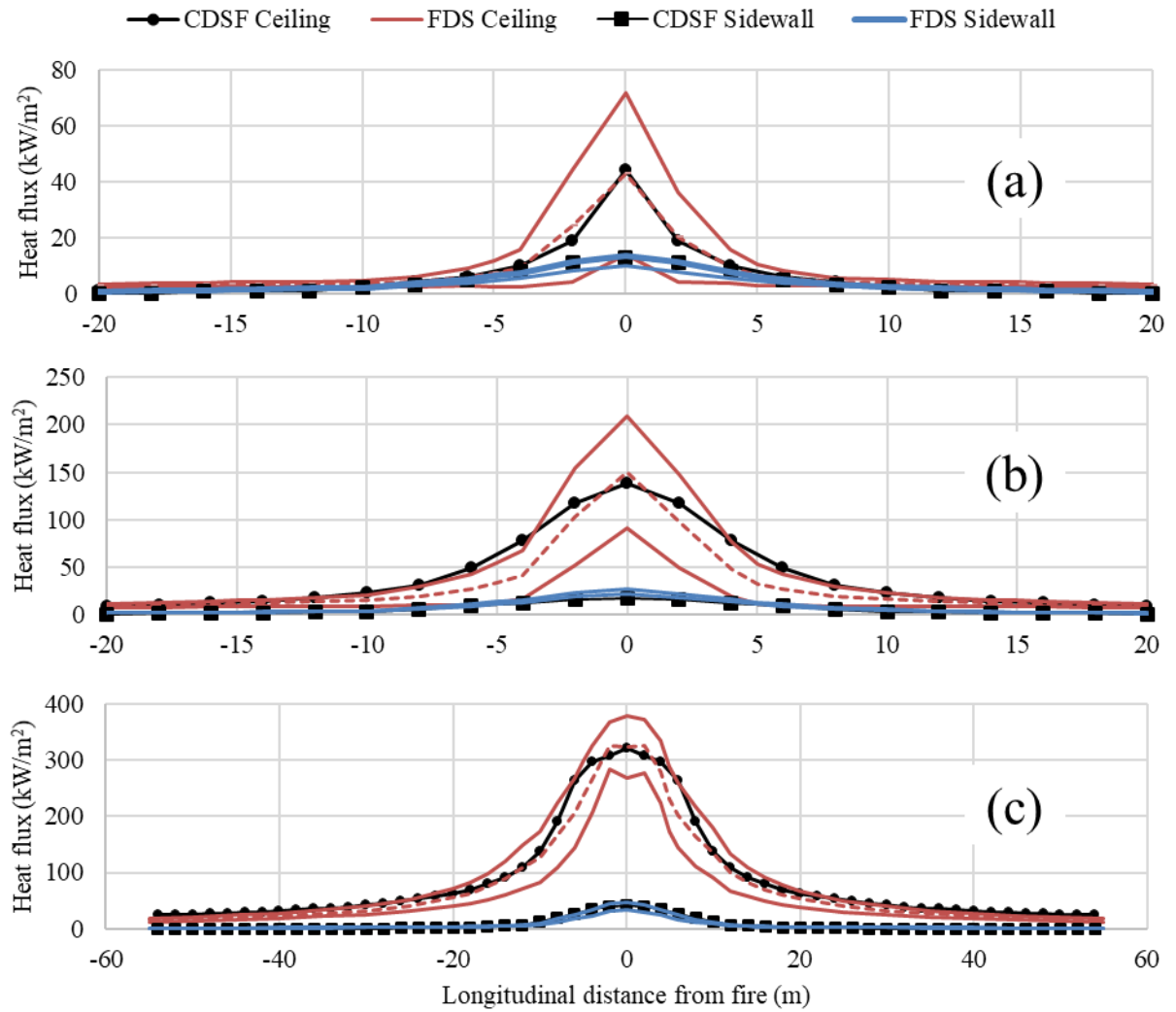
Figure 45: Longitudinal comparison of CDSF and FDS results along the tunnel centerline: (a) 30 MW, (b) 70 MW, and (c) 200 MW fire scenarios.
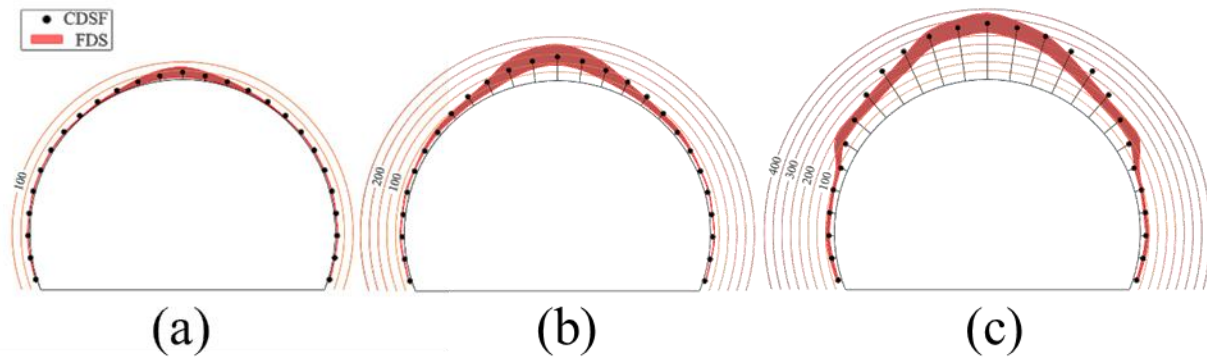
Figure 46: Cross-section comparison of CDSF and FDS heat flux (kW/m^2) at the fire location: (a) 30 MW, (b) 70 MW, and (c) 200 MW fire scenarios.

Structural Damage Mapping

Concrete has been long regarded for its fire performance due to its low conductivity, high thermal capacity, and high cross-sectional mass. However, it is a hydrated material that is sensitive to changes in moisture and internal stress, making it susceptible to spalling at elevated temperatures. While broad theories have been proposed for fire-induced spalling (most relying on pressure build-up of heated and vaporized moisture as well as restrained thermal dilation) the exact mechanism for concrete spalling under high temperature remains a complex phenomenon for which consensus has not been reached (Kodur 2000). Heat-induced spalling has the potential to lead to further structural consequence in concrete tunnel liners, as the net section is reduced from material loss on the fire-exposed face and reinforcement becomes increasingly exposed to heating.

To demonstrate how the CDSF can be leveraged for structural evaluation, a simplified spalling prediction is made for the circular tunnel prototype in Figure 37. According to experimental work done by Khoury (Khoury 2000), concrete spalling typically occurs when internal temperatures are between 250°C to 420°C and the heating rate is between 20°C/min to 30°C/min. For simplification, a heating rate of 20°C/min and temperature of 250°C will be used as the spall criteria in this study. Future work will explore the mechanics behind fire-induced spalling and develop more advanced models that can be coupled with the results of the CDSF model.

To determine whether spalling occurs during exposure to a fire from ignition to burnout, a time history of the total heat flux is needed for each discretized element of the tunnel liner. The heat flux calculated from the CDSF at each location represents the maximum value in a heat flux time history. The shape and duration of the heat flux time history can be constructed using design fire curves developed previously by Ingason (Ingason 2009) for HRR of tunnel fires. The equations needed to assemble Ingason's quadratic HRR curve are shown below in Eqs. 9-11:

$$\dot{Q}(t) = \begin{cases} \alpha_{g,q}t^2 & , \ t \leq t_{max} \\ \dot{Q}_{max} & , \quad t_{max} < t < t_D \\ \dot{Q}_{max}e^{-\alpha_{D,q}(t-t_D)}, & t \geq t_D \end{cases} \qquad (9)$$

$$t_{max} = \sqrt{\dot{Q}_{max}/\alpha_{g,q}} \qquad (10)$$

$$t_D = \frac{\chi E_{tot}}{\dot{Q}_{max}} + \frac{2}{3}t_{max} - \frac{1}{\alpha_{D,q}} \qquad (11)$$

A summary of the input parameters needed for these equations is provided in Table 5. Maximum heat release rate $\dot{Q}_{max}$ corresponds to the values selected for the three fire scenarios (30 MW, 70 MW, and 200 MW). Values for the total calorific content, E_{tot} (kJ), quadratic growth rate, $\alpha_{g,q}$ (kW/s²), and quadratic decay rate, $\alpha_{D,q}$ (s⁻¹), are taken according to the literature for the bus, light HGV, and heavy HGV design vehicles (Ingason 2009). Combustion efficiency, χ, was conservatively taken as 80% (L. Yi et al. 2006). A plot of the resulting HRR time histories for the three fire scenarios is provided in Figure 47. The same time histories can be used for total heat flux at every target by substituting the heat flux from the CDSF model for $\dot{Q}_{max}$.

Table 5: Summary of input parameters to assemble the heat flux time history

Q (MW)	E_{tot} (GJ)	χ	$\alpha_{g,q}$ (kW/s^2)	$\alpha_{D,q}$ (s^{-1})	t_{max} (min)	t_D (min)
30	150	0.80	0.178	0.001	7	54
70	350	0.80	0.178	0.001	10	57
200	1000	0.80	0.178	0.001	18	62
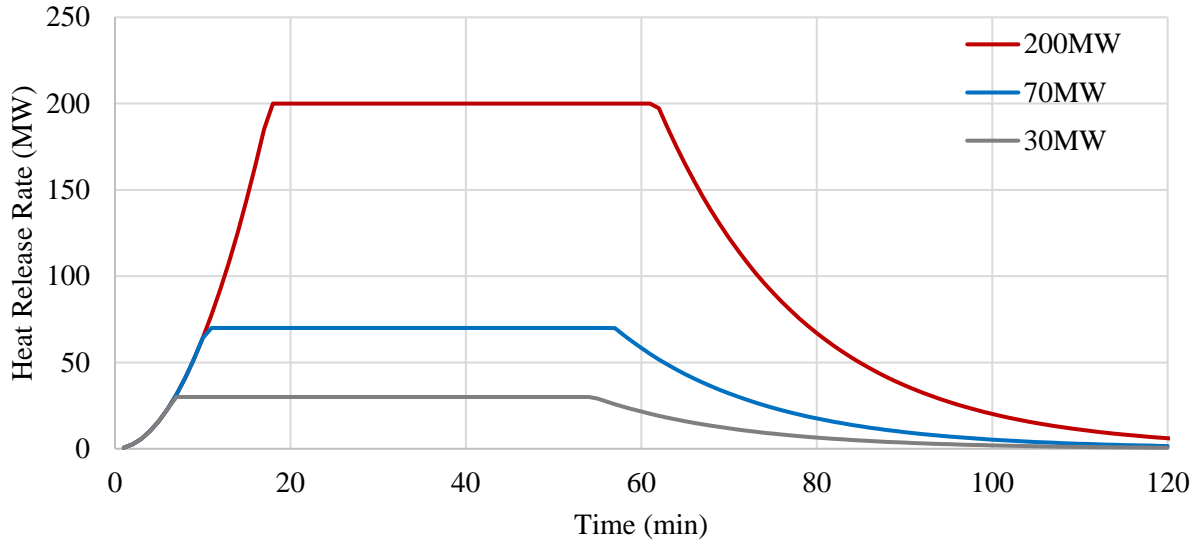
Figure 47: Time histories of HRR for the three design fire scenarios

A flowchart of the procedure for predicting spall is provided in Figure 48. At each discretized tunnel liner element, the quadratic heat flux time histories using the maximum values from the CDSF model results are used to perform a 1-D thermal analysis over the liner thickness. The liner is then checked for spalling, starting at the outermost layer at the heated face. If the two spalling criteria are not reached at any point during the exposure duration, then no spalling will occur and the evaluation is over. If the two spalling criteria are reached, then the outermost layer is said to spall. Subsequent layers moving inward are similarly checked for spalling until a layer is reached at which the two criteria are not met – the last layer to meet the criteria thereby sets the spalling depth.

The maps of spalling damage in Figure 49 are produced by using this procedure for the CDSF results of the three fire scenarios in the prototype circular tunnel. Only a single element in the discretized liner experiences any spalling for the 30 MW fire. Spalling becomes significantly more extensive for the two larger fires, with both experiencing maximum spall depths up to 25 mm (1 in.). These results could be used as input for a structural analysis model to determine the extent and timing of reduced section and cover. Future work will enhance the sophistication of the spalling evaluation and streamline the use of the CDSF model toward holistic evaluation of the tunnel structure during a severe fire.
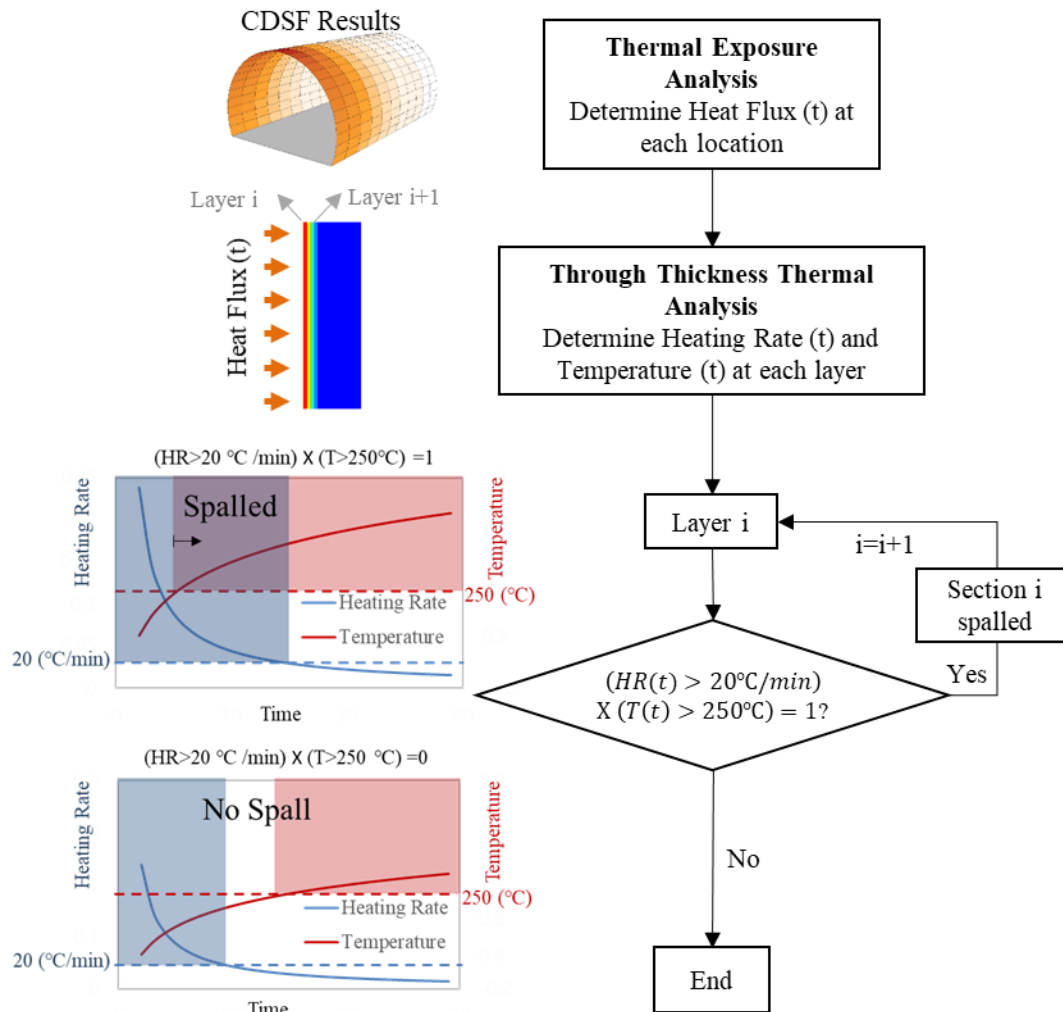
Figure 48: Flowchart for layer-by-layer spall prediction.
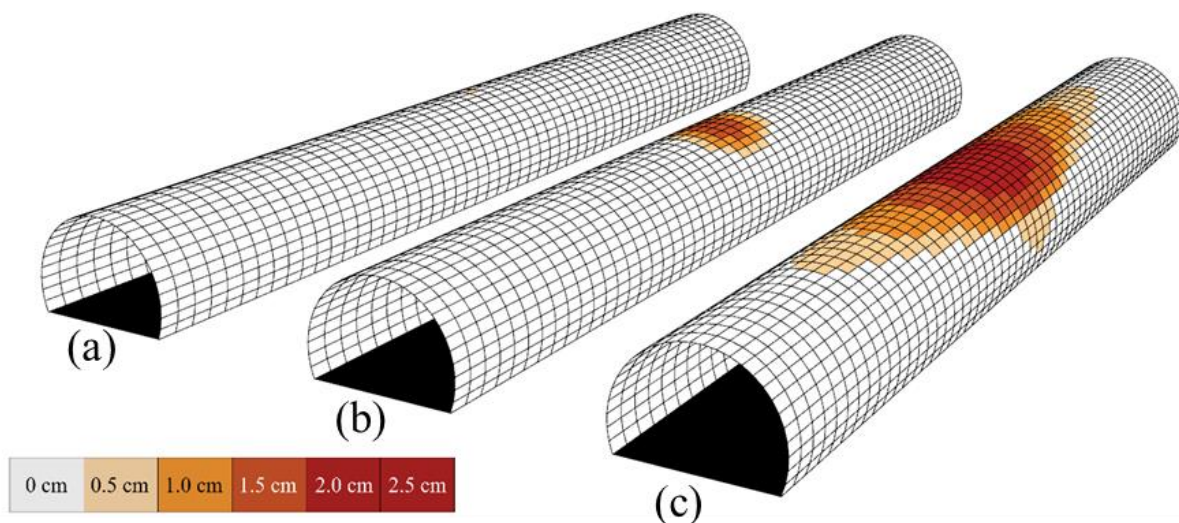
Figure 49: Map of predicted spalling on the tunnel liner: (a) 30 MW, (b) 70 MW, and (c) 200 MW

Summary of Fire Performance of Tunnels

Fires due to burning vehicles and/or cargo represent one of the most severe and likely extreme loads that a tunnel may experience over its service life. This chapter proposes a new methodology for efficient and conservative calculation of fire-induced heat flux and the resulting spall damage in concrete-lined road tunnels. Three fire severities were used to evaluate a circular tunnel prototype that is representative of current inventory and emerging construction via boring. The results of the study are as follows:

- A simplified, equivalent diesel pool fire (for which combustion properties and semi-empirical fire geometry is well studied) is proposed to represent vehicle fires (which have varying material composition and flame shape, and are thus more difficult to explicitly model).
- Thermal exposure recorded from previous full-scale tunnel fire experiments by others were used to successfully validate a high-fidelity computational fluid dynamics (CFD) solution. The CFD models were then used to benchmark the proposed analytical solutions for a broader range of fire cases.
- A statistical upper and lower bound of the heat flux time histories from CFD analysis are defined and subsequently shown to bracket the temperature gradients through the thickness of the concrete tunnel liner that are produced by the turbulent CFD results.
- A confined discretized solid flame model (CDSF) is proposed to provide an accurate and robust assessment of incident heat fluxes on circular tunnel cross sections. It provides more accurate assessment than the design fire curves and a good agreement with the CFD results at a fraction of the computational effort needed for high-fidelity numerical modeling. Future work will extend this model for other tunnel geometries and sizes.
- Fire-induced spalling damage is mapped using simplified predictive models that utilize the thermal demands calculated by the CDSF model, thereby providing a visual, holistic evaluation of direct consequences from large tunnel fires. The extent and severity of spall damage can be used as input for structural analysis of the tunnel liner. Future work will incorporate a more sophisticated calculation of spalling potential.

As illustrated in this chapter the damage to the tunnel liner can be significant for large fire events. Given that vehicular accidents and subsequent fires are much more prevalent than accidental or intentional blast events a focused research effort on determination of the fire resistance of concrete liners is conducted.

Chapter 8: Preliminary Fire Evaluation of Tunnel Liners

Concrete is widely viewed in structural design as a best-choice fire-resistant material due to its low thermal conductivity and the fact that it is non-combustible. Concrete, however, can exhibit explosive spalling and strength and stiffness loss when subjected to high thermal loading. Reduction in concrete strength and stiffness during and after fire events has been well researched and standard estimates exist for determination of residual capacity (ACI 2014). Spalling results in loss of concrete section and in extreme cases can breach the structural thickness resulting in possible progressive failure. Loss of section can expose steel reinforcement resulting in premature strength degradation and loss of flexural capacity for reinforced concrete structural elements.

A unified approach for predicting heat induced concrete spall has not been established. The current publication record has shown various results and experimental approaches, however the focus is largely on high strength concrete, and yet, still do not provide a means for spall prediction. The purpose of this chapter is to describe the preliminary experimental procedures and experimental results from trial-and-error initiation that was used to create a proof-of-concept experimental capacity for structural concrete performance under fire exposure. The authors believe that the approaches to concrete evaluation in fire in the current experimentation record lacks important detail of the concrete mix properties, heat exposure description, and day-of-testing concrete state. There are no agreed upon mechanical equation for spall prediction within the software or literature with good correlation to available experimental results showing a need for additional experimentation for concrete in fire.

Preliminary Experimentation

An experimental program was initiated to evaluate concrete material performance experiencing thermal loading consistent with fire scenarios in tunnels. A self-reacting structural loading frame was constructed to apply a typical compressive load to a concrete specimen, which also allowed a heating element to expose the structurally loaded concrete specimen to thermal loading. The axial and thermal loading frame was created following a similar experimental setup as Maluk et al. (2016). The following describes the experimental program including: structural loading frame, thermal loading, and a basic concrete specimen detail.

Preliminary Testing Apparatus

The testing apparatus, loading frame was largely based upon the experimental setup described in Maluk et al. (2016), consisting of a self-reacting loading frame with hydraulic actuator delivered load to constrain and apply axial load to the concrete specimen with a separate heating source on track sled. As shown in Figure 50, the initial concept was largely similar to the H-TRIS loading frame, however simplified with the initial attempt consisting of an electric heating source to avoid the required additional infrastructure of running gas fuel lines to power a gas heating in the H-TRIS. The testing apparatus is designed to allow for variation in applied load and axial constraint in one-direction while allowing for variation in applied thermal loading via standoff distance of the heating source with the sled positioning from a perpendicular direction to the axial constraint.
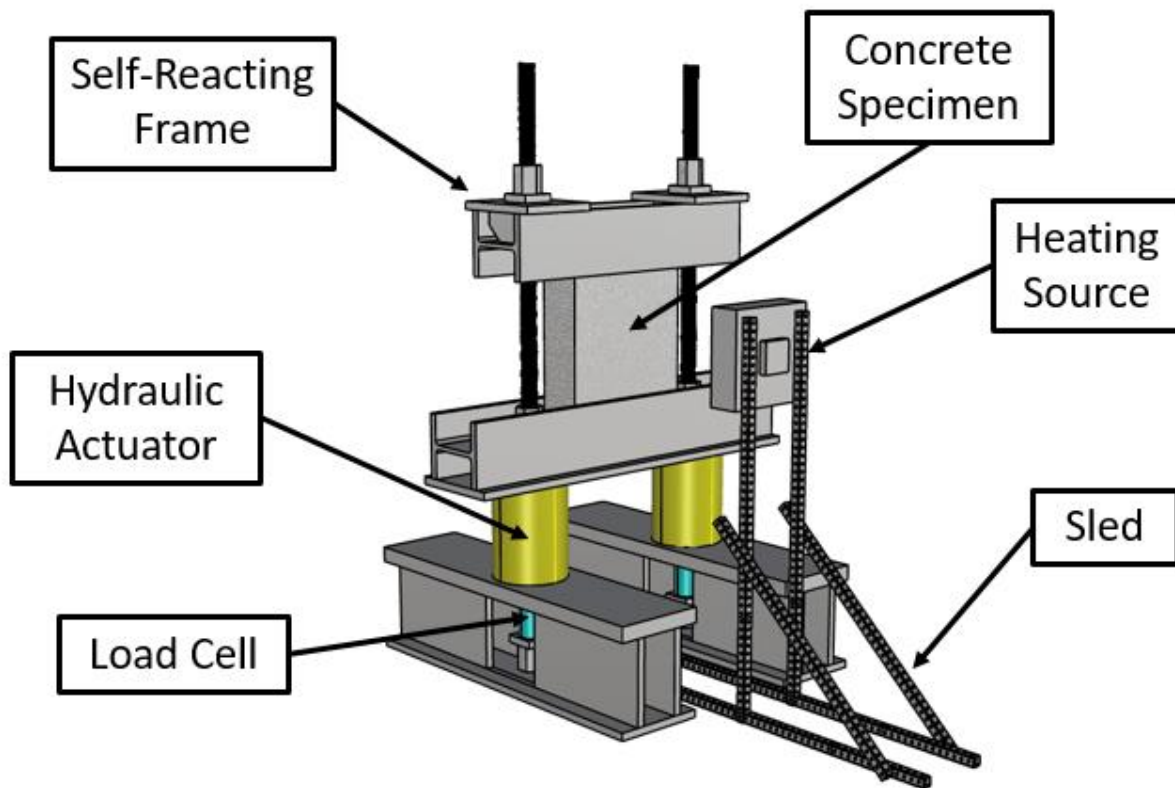
Figure 50: Initial Concept H-TRIS based Heating Load Frame

The self-reacting frame consists of two double webbed, built-up I-sections acting as spreader beams to distribute the loading frame and specimen weight over a larger floor area. Between the spreader beam webs on both spreader beams, a nut and washer cap a threaded rod. The threaded rod sandwiches a hollow pipe-style load cell between the washer and the bottom of the spreader beam top flange. The threaded rod passes through a hollow section hydraulic actuator ram and through a welded plate and w-section that acts as the base support for the concrete specimen. The threaded rods pass the sides of the concrete specimen and through the top built-up plate and I-shaped section that acts as the top support for the concrete specimen. The configuration allows for the hydraulic rams to push the bottom specimen support beam to compress the concrete sample against the top specimen support beam.

The hydraulic actuators are pressure controlled via a hydraulic fluid pump that is pressure controlled. The in-line load cells are used to set the delivered axial load as well as monitor the variation in the applied load throughout the heat exposure duration. Axial load of 600 kips can be applied, easily accommodating 30% of the compressive strength of the concrete. Due to the pressure control system the axial load variation is typically 2% of the targeted value throughout the duration of heat exposure, and also 2% between left and right actuators.

The heating source is mounted on the track sled to allow for vertical adjustment to center the radiant output of the heater on the load frame mounted concrete specimen. The sled then allows for horizontal movement to allow for a safe distance to start the heat output and also to control the applied peak heat flux to the sample. Additional detail concerning the heating sources used in the

experimental refinement is included in the following section, Thermal Loading, so that calibration of the heat output can be discussed in conjunction.

Thermal Loading

The first selected heating source was an electric quartz-faced 10 in. by 10 in. radiant surface heating panel running at 208 V. An electric panel was first used to simplify the infrastructure requirements of the complete load frame and thermal loading setup, allowing for ease of relocation of the loading frame and reduction in required gas lines or fuel tanks for power. To calibrate the heating source output via standoff distance, a water-cooled radiometer, specifically the Hukseflux SBG01 heat flux meter, was used to record the heat flux at the specimen surface at specific standoff distances. The thermal load calibration setup is shown in Figure 51.
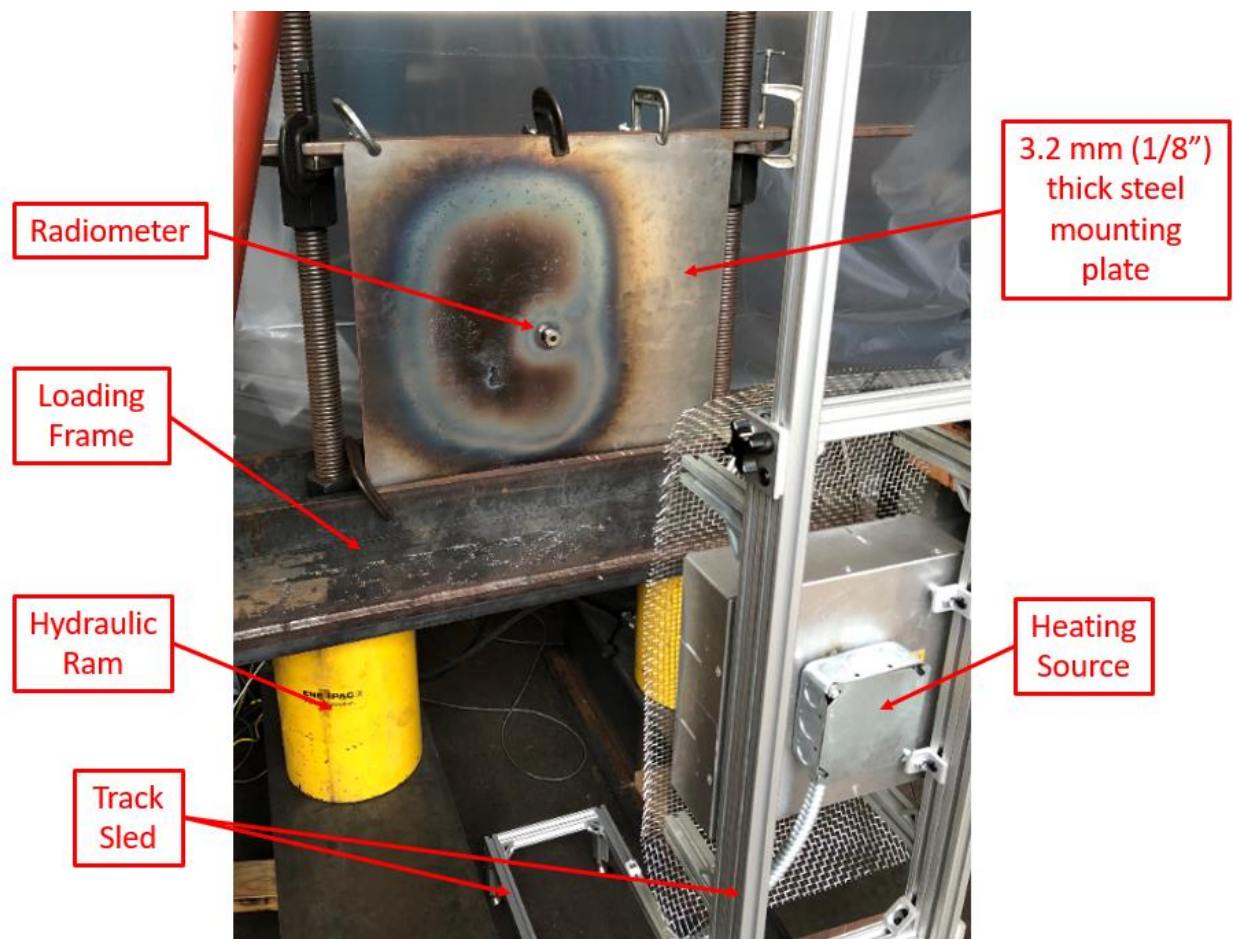
Figure 51: Thermal load calibration setup

To calibrate the heating source output, the radiometer was mounted through a hole in a plate of steel and located on-center of the heating source. The plate steel was used to duplicate the radiation feedback loop between the heating source and test specimen. As additional calibrations were completed a thicker 6.4 mm (1/4 in.) steel plate was substituted for the 3.2 mm mounting steel, and the dimensions of the 6.4 mm steel was adjusted to match the typical concrete specimen heat exposed surface with the top specimen support beam of the loading frame also included to match specimen setup as closely as possible during calibrations.

Calibrations for the heating source were also conducted to evaluate the effects of convective air movements around the heating source and target by placing metal film around the heating source, closing and opening doors to the experimentation space, etc. Ultimately, it was determined that convective effects could not be eliminated therefore specific heat flux curve time-histories were recorded instead of reporting a specific peak heat flux. This approach gives a better description of the actual thermal load on the test specimen through time, being more explicit in describing heating rate and heat fluctuations due to convective effects.

Figure 52 shows a standoff to heat flux output as measured by the radiometer in the calibration setup. Note, an estimate of Maluk et al. (2016) H-TRIS power curve is included as reference. The square 25.4 cm electric heating panel is significantly under powered when compared with the H-TRIS. Additionally, the initial concrete specimen tests, Panels 1 through 3 showed heat cracking, as seen in the results section, however no spalling behavior was observed even after a full hour of heat exposure. The first three panels were tested with the 25.4 cm electric heating source at 5.1 cm (2 in.) of standoff, such that the concrete specimen experienced approximately 50 kW/m^2 of peak heat flux. For panel 4, the standoff distance was reduced to 2 cm to achieve approximately 80 kW/m^2 of heat flux, inducing explosive concrete thermal spalling behavior. The 25.4 cm square electric heater was damaged by the spall event at the 2 cm standoff.
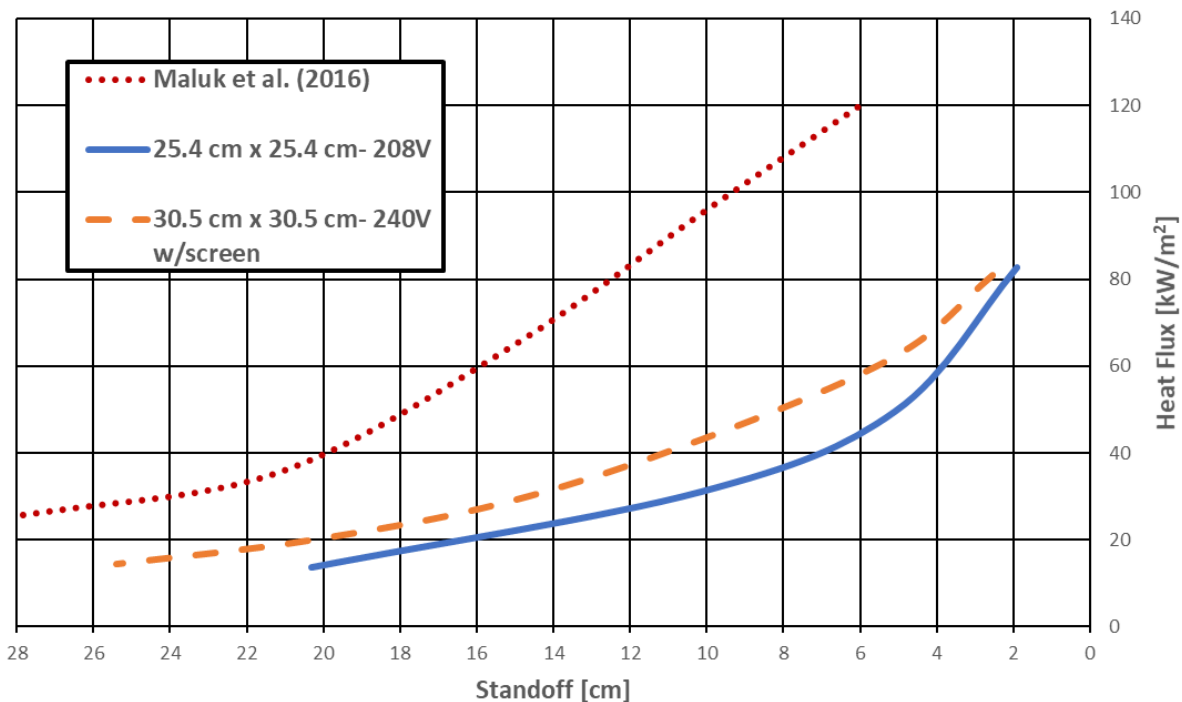
Figure 52: Heat Flux to Standoff Distance Power Curve Comparison

Post panel 4 testing, a new heater was ordered to replace the 25.4 cm heater. At the time, it was believed that increasing the radiative surface would be sufficient to increase the peak heat flux. The goal being to increase the output heat flux of the heater so that a standoff distance adequate to protect the equipment during spalling behavior; to approach the H-TRIS power curve output. Therefore, a 30.5 cm quartz-faced electric heating panel was obtained. Several iterations of the electric power source for the 30.5 cm electric panel was used to evaluate additional means of increasing heat flux output; 208 V and 240 V setups were tested in calibration. Additionally, a

protective screen was placed at the concrete specimen to prevent projectile spalling debris, however was found to reduce some of the thermal load. Figure 52 shows the H-TRIS, the 25.4 cm, and the 30.5 cm electric heater with a protective screen power curves.

Two specimens (Panels 5 and 6) were tested with the 30.5 cm electric heater at 5.1 cm (2in.) and 3.8 cm (1.5 in.) of standoff respectively, yielding peak heat fluxes of 57 and 65 kW/m^2. Both panels did not exhibit spalling behavior after more than an hour of heat exposure. The initial experimental results suggest that threshold is between 70 and 80 kW/m^2 is needed to induce spall, however additional variable in the thermal load may play significant roles which is not evaluated in the brief preliminary experimental study. Heating rate is suggested in the literature review for thermal concrete spall as playing a significant role. Further testing with the explicit goal of evaluating heat flux threshold for spall behavior to include heating rate would be required to validate this initial finding.

Moving forward with testing apparatus evolution, a commercial heating unit company was contracted to adapt a gas-fueled open deep-fat fry cooker to the project needs. It was determined that the available electric heating units would not be capable of delivering adequate heat flux output to clear the 80 kW/m^2 threshold at a greater than 12.7 cm (5 in.) standoff distance. The first iteration heater used a permeable metal foam material for the radiant surface grillage and was initial powered via a camp-style propane tank. After several adaptations, the commercial company provided a 30.5 cm (12 in.) metal foam grillage heater, fueled by natural gas that included a pre-flame air to fuel mixer. The air to fuel ratio was controlled to optimize the energy potential for the heater. Additionally, a reflector box was added to surround the heated radiant panel surface of the heater to focus arrant radiation back to the target. The metal foam grillage heater was used in 19 tests and a series of calibrations. Ultimately, the metal foam grillage experienced thermal cycling fatigue and ruptured.

The commercial company replaced the metal foam material at the grillage with a metal fiber material, which performed slightly better than the metal foam, however after only 2 calibrations and 3 tests the grillage box (which the grillage material is mounted to and receives the pre-mixed air and fuel) ruptured. Additional spot welds were added to the grillage box, which slightly increased the peak heat flux output compared to the fewer welds box.

Figure 53 shows the heat flux time-history calibrations from the metal foam grillage at two standoff distances, the two-weld pattern metal fiber grillages, and the ASTM E1529 specified heat flux values for hydrocarbon fire simulation. Two metal foam heater standoff distances are meant to illustrate the drastic difference is heat flux between only 3.5 cm (1-3/8 in.) observed at the target, indicative of the exponential behavior of radiation to distance. As seen in Figure 52 the metal foam and two metal fiber heater setups provided heat flux values just below the ASTM defined hydrocarbon fire values (ASTM Standard E1529 2016). Note that ASTM E1529 does not specify any behavior or rate of heating before 5 minutes of exposure, and the dashed E1529 high and low lines are representative of the $\pm$ 8 kW/m^2.
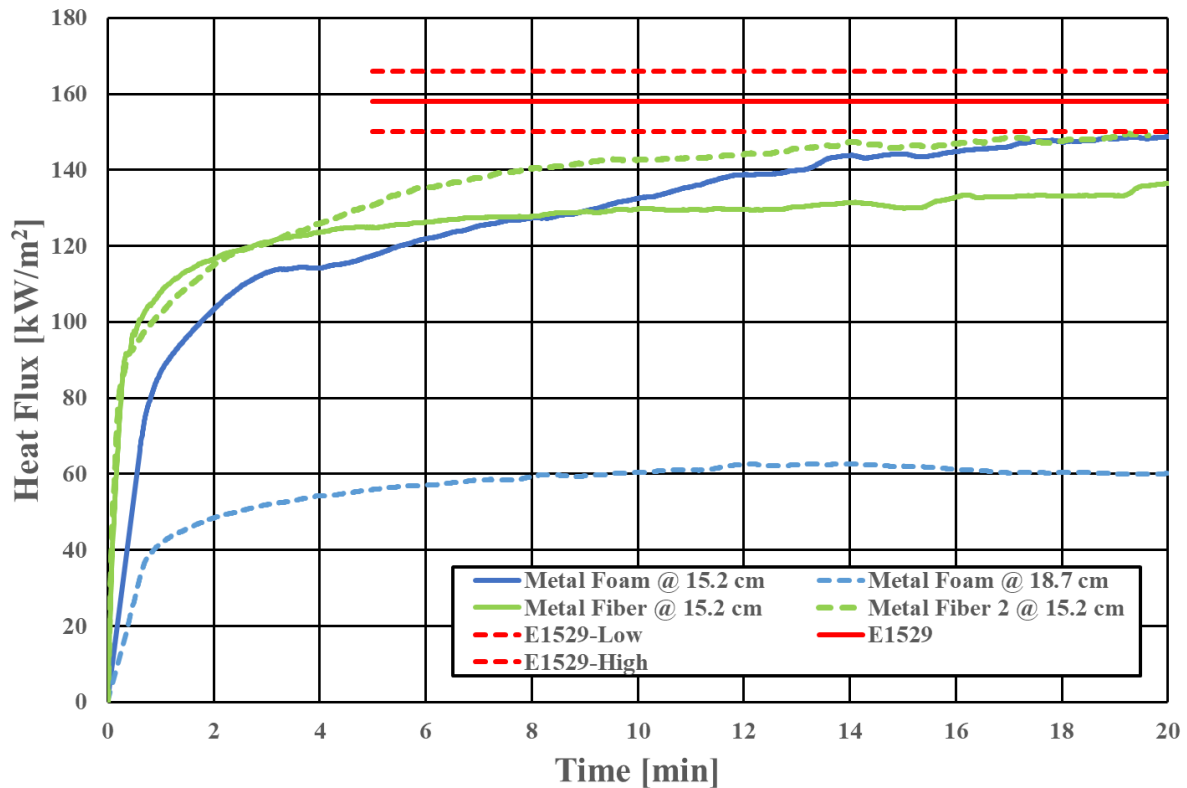
Figure 53: Heat Flux Time History Summary

Concrete Specimens

The testing apparatus was designed to accommodate a concrete specimen panel constructed similarly as that shown in Figure 54, 152 mm (6 in.) in thickness, 610 mm (24 in.) in height, and 457 mm (18 in.) in width with #16 (#5 US) steel reinforcing bars aligned with two longitudinal and two transverse located at a clear cover of 38 mm (1-1/2 in.) from the heat exposed face. Two lifting lugs were also placed in the top edge of the sample to facilitate movement of the sample.
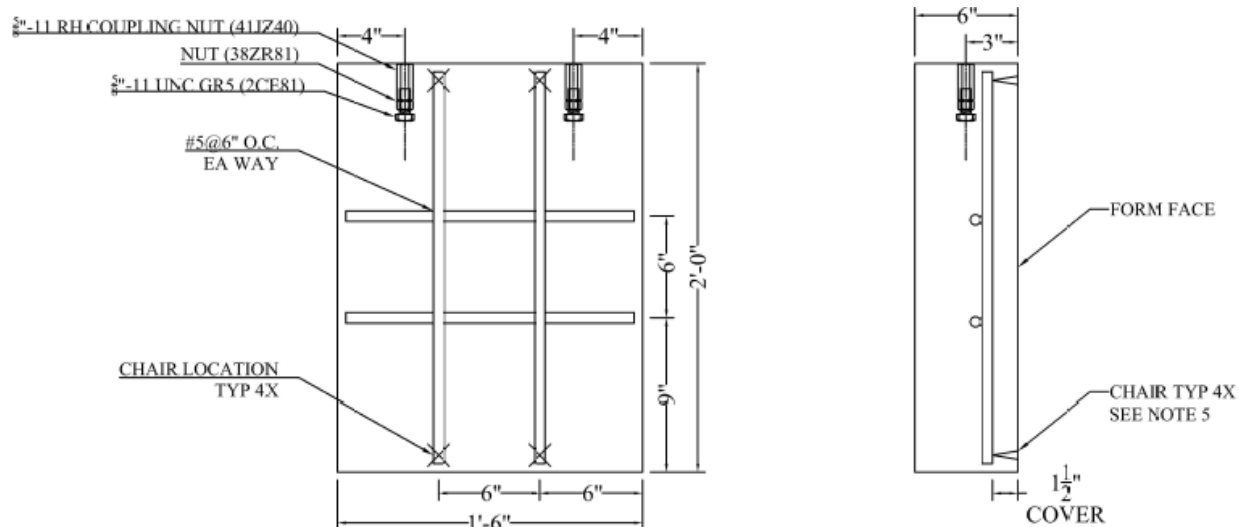
Figure 54: Concrete Specimen Detail (Typical)

The exposed face is covered at the top and bottom by 83 mm (3-1/4 in.) of the loading frame flanges reducing the directly heat exposed face to 2032 sq. mm (315 sq. inches) of area minimizing any additional thermal effects caused by the locations of lifting lug and reinforcing bar location chairs. In addition to the typical specimen shown in Figure 54, three specimens with (6) #10M (#3 US) reinforcing bars vertical and horizontal, instead of (2) #16M typical, and three specimens with 50x50 MW13.3/13.3 (2x2 W2.1/2.1) Surface Mesh with 3/4 inches of concrete cover and (2) #5 US horizontal bars were also tested.

Typical concrete specimens have embedded k-type thermocouple sensors placed at various depths within the sample thickness. The initial experimentation used thermocouples placed at 2.54 cm (1 in.), 7.62 cm (3 in.), and 12.7 cm (5 in.) from the heated specimen face, with approximately 60 cm of wire lead extending beyond the opposite parallel concrete surface from the heated surface. K-type thermocouple leads are connected via a junction box for each depth to k-type thermocouple wire extensions to a data-logger for computer recording.

Two concrete mix designs were used in the preliminary testing setup samples, from two different manufacturers. Manufacturer 1 was a contracted precast concrete company that used concrete mix, C1 consisting of two batches with slightly different water to cement ratios. C1 used Type III Portland cement, fly ash pozzalan, A57 aggregate, with an average 0.38 water to cement ratio, which resulted in a 6700 psi tested compressive strength. Manufacturer 2 consisted of in-house formwork completed by the research team with a local commercial concrete supplier for the second concrete mix, C2. C2 consisted of Type I Portland cement, blast furnace slag pozzalan, A57 and A8 aggregate, with a water to cement ratio of 0.40, resulting in a 5400 psi tested compressive strength. Large aggregate for both mixes were sourced from the same or neighboring quarries, with fine aggregate from the exact same location. Admixture chemicals for air entrainment and high-range water reducer, as well as, the requested design air percentage were the same.

Ultimately, the testing apparatus was designed to accommodate 152 mm (6 in.) thick by 610 mm (24 inches) height by 457 mm (18 inches) wide specimens, however modifications can be made the loading frame specimen supports to accommodate larger or thicker specimens. Protective coatings, such as tile or Spray-Applied Fire-Resistant Material, may also be added to any concrete specimens to be tested in the current physical load frame.

Refined Testing Apparatus

The refine testing apparatus is shown in Figure 55. The self-reacting load frame was unchanged from the initial concept, but thermal insulation was added to the exposed threaded rod and the hydraulic ram actuators to minimize thermal cycling fatigue and to reduce unintended fire ignition. Additions of thermocouple sensors to be in surface contact on the heat exposed sample surface: one at the center top of the exposed surface and one at the center bottom were made. Not shown: the electrical 110 V power chord to run the gas-fueled heater controller that operates the air to fuel mixer and ignition spark; the flexible gas line that allows the heater to move on the sled; and a computer and data logger used to record the output from the embedded thermocouple sensors, the surface contact thermocouple sensors, and load cells.
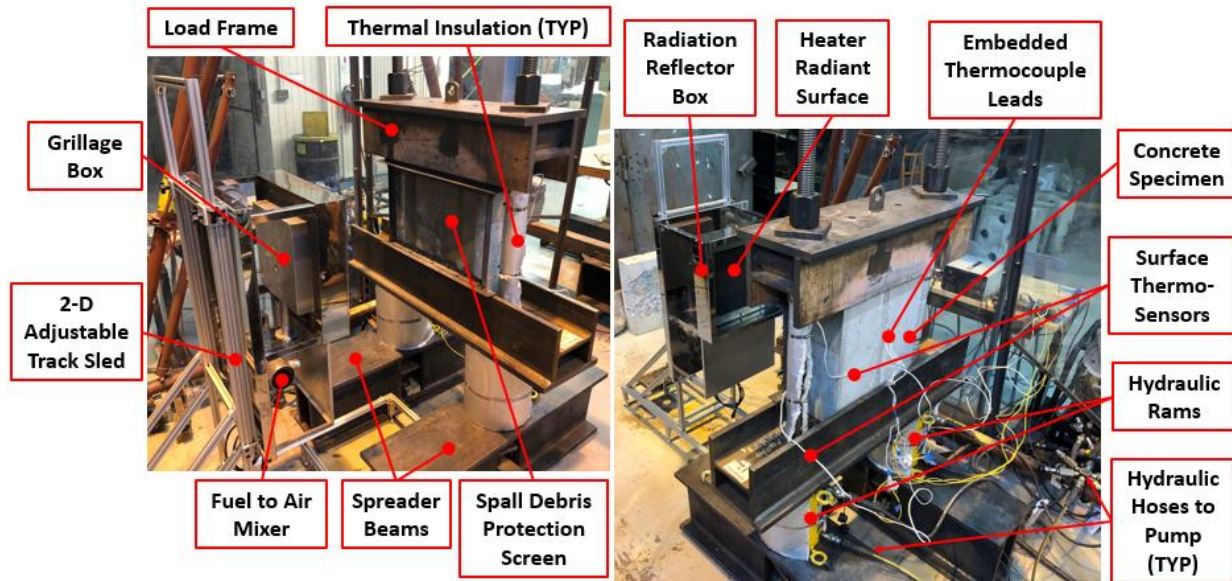
Figure 55: Full concept experimental testing apparatus

Selected Panel Results

As discussed in the testing apparatus section concerning the heating source selection process, the panels tested under the 25.4 cm electric heater are shown in Figure 56. Black felt-tipped ink marker was used to mark cracking on the heat exposed specimen surface post testing for visual aid. As can be seen in Figure 56 the non-spalled samples exhibited extensive cracking at the peak heat flux affected areas (i.e. the 25.4 cm region in the center of the specimen. Note the concrete discoloration around the highest heat affected area in Panels 1, 2, and 3, while Panel 4 has not discernable discoloration. This is largely due to the heat exposure duration. Panel 4 spalled at approximately 12 minutes of heat exposure not allowing the extensive interior temperatures and chemical dehydration reactions to occur.

Panel 1 – C1 – No
Spall Panel 2 – C1 – No
Spall Panel 3 – C1 – No
Spall Panel 4 – C1 – Spall
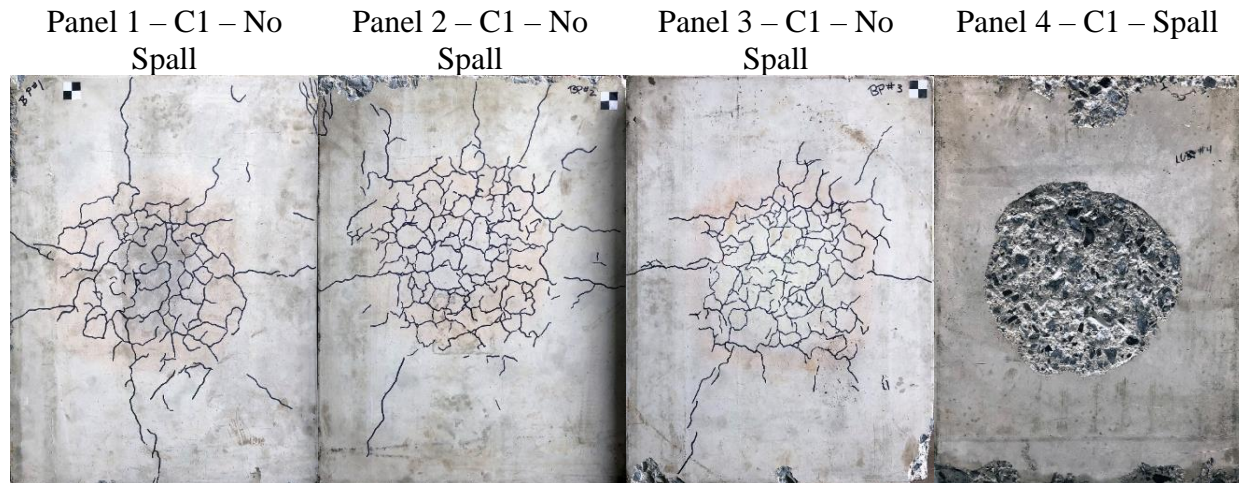
Figure 56: 25.4 cm at 208 V Electric Heater Test Results

Figure 57 shows a comparison between Panel 3 and 4 from the embedded thermocouples. Note the different in duration with Panel 3 at nearly 1 hour of exposure while Panel 4 was exposed for less than 7 minutes. The internal peak temperature at the 2.54 cm thermocouple depth, T1, is over 450ºC for Panel 3 while not exceeding 90ºC in Panel 4. Therefore peak internal temperature does not appear to have a direct effect on concrete thermal spall behavior. Additionally the peak heat flux for Panel 3 was approximately 60 kW/m^2 while Panel 4 was approximately 80 kW/m^2, therefore the energy transmission for the spalled behavior was much greater leading to a faster rate of heating observed at the embedded thermocouples. Note that the T5 thermocouple, embedded at 12.7 cm from the heated surface is relatively unaffected even after nearly an hour of heating in Panel 3. It was observed that temperature collection at depths exceeding 7.5 cm was uninformative for concrete material behavior under thermal load.
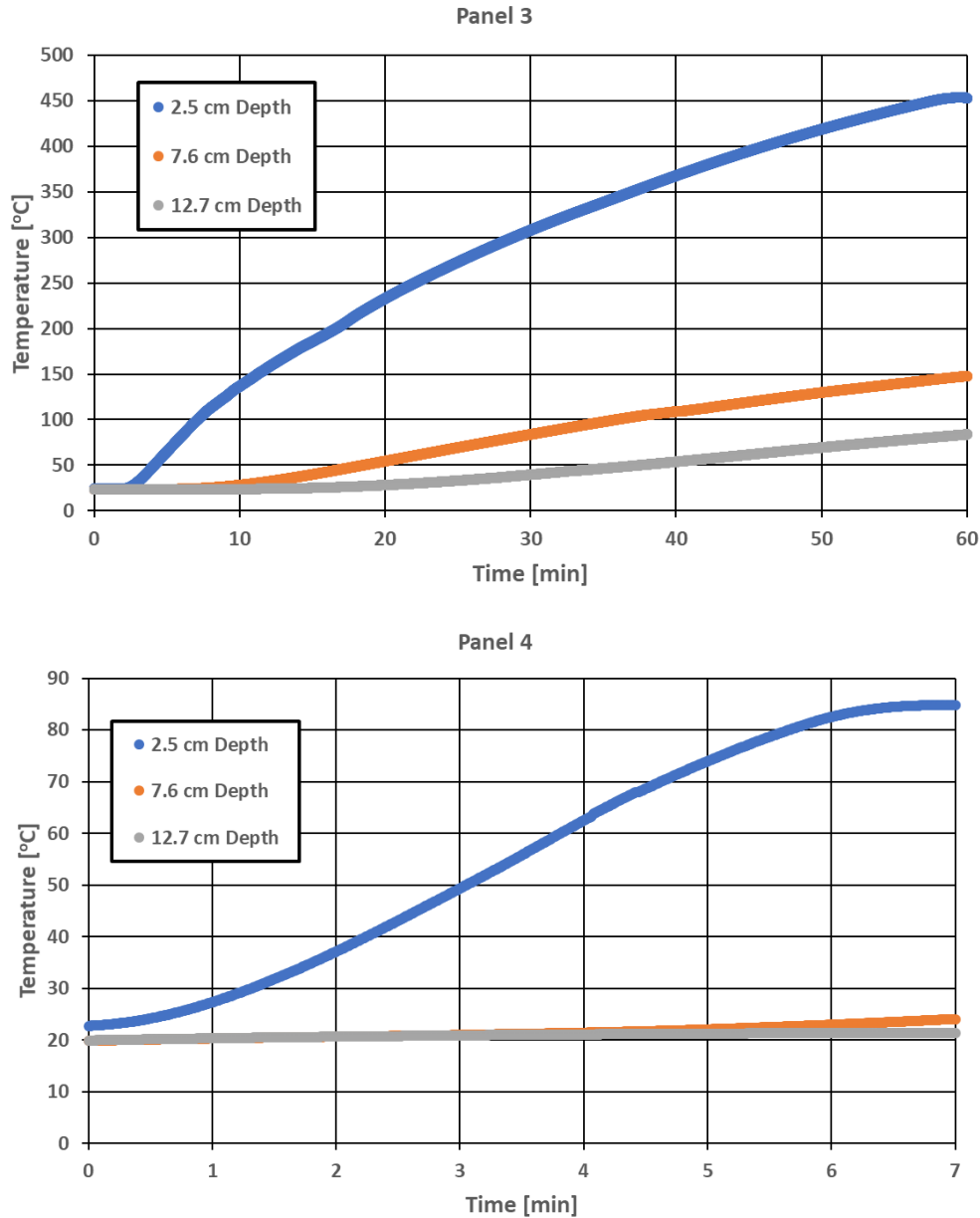
Figure 57: Sample embedded thermocouple results

Shown in Figure 58 with the 30.5 cm^2 electric heater on 240 V power expressing a peak heat flux less than 65 kW/m^2, Panels 5 and 6 did not spall even after an hour of heat exposure. Note the same discoloration patterning on these panels that was also observed with the smaller surface area electric heater used on Panels 1-4. The embedded thermocouple output for Panels 5 and 6 were similar to Panel 3 shown in Figure 57.

Panel 5 – C1 – No
Spall

Panel 6 – C1 – No
Spall
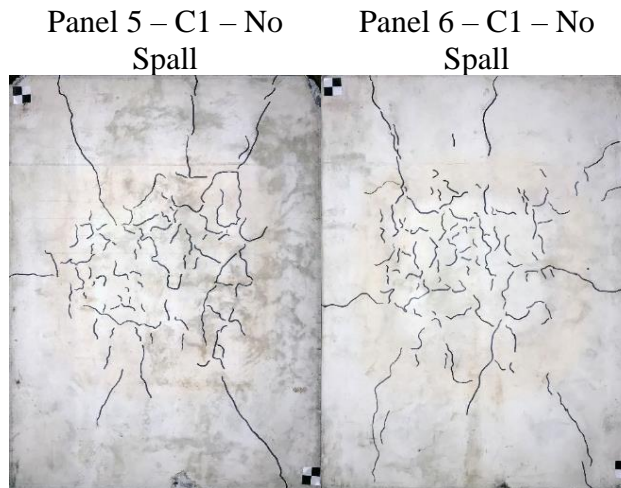
Figure 58: 30.5 cm x 30.5 cm at 240 V Electric Heater Test Results

Figure 59 shows the specimen results for Panel 14 exposed to the Metal Foam heater, Panel 28 exposed to the Metal Fiber 1 heater, and Panel 29 exposed to Metal Fiber 2 heater iterations all at 15.2 cm of standoff. The closer to the ASTM E1529 curve the heater iteration performs, the more extensive the observed spalling behavior.

Panel 14 – C1 –
Spalled

Panel 28 – C2 –
Spalled

Panel 29 – C2 –
Spalled
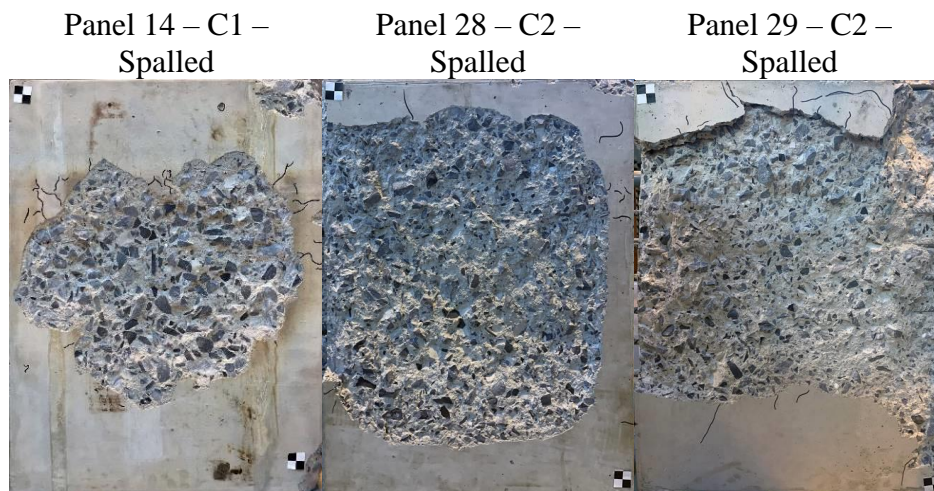
Figure 59: Results from metal foam, metal fiber 1, and metal fiber 2

Preliminary Fire Experimental Program Findings

A preliminary experimental program was conducted on concrete to assess the impact of fire exposure on concrete elements. The background on the test setup is provided. An axial load frame combined with a gas-powered heating panel is developed for examination of spall on concrete exposed to fire effects. The results of the preliminary experimentation are presented and discussed. A list of novel preliminary findings are given here:

- The preliminary experimentation was successful in establishing the capabilities of the refined testing apparatus to evaluate performance near the ASTM E1529 hydrocarbon fire thermal loading intensities. Concrete material behavior under thermal loading can be evaluated in a consistent and repeatable fashion for variation in axial load/restraint, heat flux intensity, moisture conditions, mix designs, and reinforcement details.

- The observation of a threshold between 70 and 80 kW/m^2 was required to exhibit spalling behavior. This observation is contingent upon the specific experimental apparatus discussed herein and requires additional focused experimentation to verify for different concrete mix designs and heating rates.
- Internal concrete temperatures far exceeding the boiling point of water were observed in specimens that did not exhibit spalling behavior. Therefore, the observation that peak temperature and heating rate must be considered to assess the likelihood of concrete spalling behavior.

Based on the observed response a comprehensive experimental program is recommended to examine the performance of concrete subject to thermal effects.

References

ACI. 2014. *Code Requirements for Determining Fire Resistance of Concrete and Masonry Construction Assemblies*. Farmington Hills, MI: American Concrete Institute.

American Association of State Highway and Transportation Officials, ed. 2001. *A Policy on Geometric Design of Highways and Streets, 2001*. 4th ed. Washington, D.C: American Association of State Highway and Transportation Officials.

Association, National Fire Protection. 2011. *NFPA 502, Standard for Road Tunnels, Bridges, and Other Limited Access Highways*. NFPA.

ASTM Standard E1529. 2016. "Test Methods for Determining Effects of Large Hydrocarbon Pool Fires on Structural Members and Assemblies." Conshocken, PA: ASTM International. https://doi.org/10.1520/E1529-16E01.

Aydar, Buribayev. 2010. "Suicide Bombers Kill at Least 38 in Moscow Subway." *Reuters*, March 29, 2010. https://www.reuters.com/article/us-russia-metro-blast-idUSTRE62S0FM20100329.

Babrauskas, Vytenis. 2016. "Heat Release Rates." In *SFPE Handbook of Fire Protection Engineering*, 799–904. Springer.

Bai, Fengtao, Qi Guo, Kyle Root, Clay Naito, and Spencer Quiel. 2018. "Blast Vulnerability Assessment of Road Tunnels with Reinforced Concrete Liners."

Bechtel / Parson Brinckerhoff. 1995. "Memorial Tunnel Fire Ventilation Test Program: Test Report." MA: Massachusetts Highway Department, FHWA.

Bergeson, William, and Steve Ernst. 2015. "Tunnel Operations, Maintenance, Inspection, and Evaluation (TOMIE) Manual." FHWA-HIF-15-005. Washington DC 20590.

Bjnews. 2017. "Blast Result From Nature Gas Tank Truck near No. 5 Futuyu Tunnel." Bjnews. 2017.

Branch, Rail Accident Investigation. 2010. "Technical Investigation Report Concerning the Fire on Eurotunnel Freight Shuttle 7412 on 11 September 2008." *Rail Accident Investigation Branch, Derby, UK*.

Brannon, Rebecca M, and Seubpong Leelavanichkul. 2009. "Survey of Four Damage Models for Concrete," no. August: 1–80.

Broadhouse, B.J. 1995. "The Winfrith Concrete Model in LS-DYNA 3D." Carlsbad: Strucututal Performance Department AEA Technology Winfrith Technology Center.

Broadhouse, B.J. and Neilson, A.J. 1987. "Modelling Reinforced Concrete Structures in DYNA3D." *Safety and Engineering Division* AEEW-M 246.

Buonsanti, M., and G. Leonardi. 2013. "3-D Simulation of Tunnel Structures under Blast Loading." *Archives of Civil and Mechanical Engineering* 13 (1): 128–34. https://doi.org/10.1016/j.acme.2012.09.002.

Cadorin, J. F., J. M. Franssen, D. Pintea, L. G. Cajot, M. Haller, and J. B. Schleich. 2002. *Software OZONE V 2.2*. Liège.

Castedo, R., P. Segarra, A. Alañon, L. M. Lopez, A. P. Santos, and J. A. Sanchidrian. 2015. "Air Blast Resistance of Full-Scale Slabs with Different Compositions: Numerical Modeling and Field Validation." *International Journal of Impact Engineering* 86: 145–56. https://doi.org/10.1016/j.ijimpeng.2015.08.004.

CEN. 2008. *EN 1992-1-2: Eurocode 2: Design of Concrete Structures - Part 1-2: General Rules - Structural Fire Design*. Brussels, Belgium: European Commission for Standardization.

Colombo, Matteo, Paolo Martinelli, and Marco di Prisco. 2016. "On the Blast Resistance of High Performance Tunnel Segments." *Materials and Structures/Materiaux et Constructions* 49 (1–2): 117–31. https://doi.org/10.1617/s11527-014-0480-7.

De, Anirban, Alberto N. Morgante, and Thomas F. Zimmie. 2016. "Numerical and Physical Modeling of Geofoam Barriers as Protection against Effects of Surface Blast on Underground Tunnels." *Geotextiles and Geomembranes* 44 (1): 1–12. https://doi.org/10.1016/j.geotexmem.2015.06.008.

Department of Defense (DoD). 2014. *UFC 3-340-02 Unified Facilities Criteria: Structures to Resist the Effects of Accidental Explosions*. Washington, D.C.

D.L. Grote, S.W. Park, M. Zhou. 2001. "Dynamic Behavior of Concrete at High Strain Rates and Pressures: I. Numerical Simulation." *International Journal of Impact Engineering* 25 (9): 887–910. https://doi.org/10.1016/S0734-743X(01)00021-5.

Duffe, Pierre, and Michel Marec. 1999. "Task Force for Technical Investigation of the 24 March 1999 Fire in the Mont Blanc Vehicular Tunnel." *Minister of the Interior, Ministry of Equipment, Transportation and Housing, France* 30.

Dwaikat, M. B., and V. K. R. Kodur. 2009. "Hydrothermal Model for Predicting Fire-Induced Spalling in Concrete Structural Systems." *Fire Safety Journal* 44 (3): 425–34. https://doi.org/10.1016/j.firesaf.2008.09.001.

Egilsrud, Philip. 1984. "Prevention and Control of Highway Tunnel Fires." Tech Report FWHA/RD-83-032.

Ekström, Jonas. 2015. "Concrete Structures Subjected to Blast Loading." Chalmers University of Technology.

EUROPEAN COMMITTEE FOR STANDARDIZATION. 2002. *EN 1991-1-2 Eurocode 1: Actions on Structures - Part 1-2: General Actions -Actions on Structures Exposed to Fire*. EN 1991-1-2:2002 E.

Feldgun, V. R., Y. S. Karinski, and D. Z. Yankelevsky. 2014. "The Effect of an Explosion in a Tunnel on a Neighboring Buried Structure." *Tunnelling and Underground Space Technology* 44: 42–55. https://doi.org/10.1016/j.tust.2014.07.006.

Feldgun, V. R., A. V. Kochetkov, Y. S. Karinski, and D. Z. Yankelevsky. 2008. "Internal Blast Loading in a Buried Lined Tunnel." *International Journal of Impact Engineering* 35 (3): 172–83. https://doi.org/10.1016/j.ijimpeng.2007.01.001.

Franssen, Jean-Marc, and Thomas Gernay. 2017. "Modeling Structures in Fire with SAFIR®: Theoretical Background and Capabilities." *Journal of Structural Fire Engineering* 8 (3): 300–323.

Grunwald, Christoph, Benjamin Schaufelberger, Alexander Stolz, Werner Riedel, and Thomas Borrvall. 2017. "A General Concrete Model in Hydrocodes: Verification and Validation of the Riedel–Hiermaier–Thoma Model in LS-DYNA." *International Journal of Protective Structures* 8 (1): 58–85. https://doi.org/10.1177/2041419617695977.

Guo, Qi, Kyle Root, Spencer E. Quiel, and Clay J. Naito. 2019. "Streamlined Calculation of Fire-Induced Heat Flux and Resulting Spalling Damage for Concrete Tunnel Liners." In *Transportation Research Board Conference Proceedings*. Washington, D.C.

Hallquist, John O. 2012. *LS-DYNA THEORY MANUAL. International Journal of Imaging Systems and Technology*. Vol. 22. https://doi.org/10.1002/ima.22028.

Holmquist, Timothy J., and Gordon R. Johnson. 2011. "A Computational Constitutive Model for Glass Subjected to Large Strains, High Strain Rates and High Pressures." *Journal of Applied Mechanics, Transactions ASME* 78 (5): 1–9. https://doi.org/10.1115/1.4004326.

Holmquist, Timothy J., Gordon R. Johnson, and Charles A. Gerlach. 2017. "An Improved Computational Constitutive Model for Glass." *Philosophical Transactions of the Royal Society A: Mathematical, Physical and Engineering Sciences* 375 (2085): 1–5. https://doi.org/10.1098/rsta.2016.0182.

Hu, Guo, Jun Wu, and Liang Li. 2016. "Advanced Concrete Model in Hydrocode to Simulate Concrete Structures under Blast Loading." *Advances in Civil Engineering* 2016. https://doi.org/10.1155/2016/7540151.

Hu, L. H., R. Huo, W. K. Chow, H. B. Wang, and R. X. Yang. 2004. "DECAY OF BUOYANT SMOKE LAYER TEMPERATURE ALONG THE LONGITUDINAL DIRECTION IN TUNNEL FIRES." *Journal of Applied Fire Science* 13 (1): 53–77. https://doi.org/10.2190/BQ02-N5TG-7TC7-TQFX.

Hurley, Morgan J., ed. 2016. *SFPE Handbook of Fire Protection Engineering*. New York, NY: Springer New York.

Ingason, Haukur. 2009. "Design Fire Curves for Tunnels." *Fire Safety Journal* 44 (2): 259–65.

Jansen, Bart. 2017. "St. Petersburg Subway Bombing Reveals Terror Vulnerability." *USA TODAY*, April 3, 2017. https://www.usatoday.com/story/news/2017/04/03/subway-security-st-petersburg-new-york-london-paris-brussels/99988934/.

Jansson, Robert. 2013. "Fire Spalling of Concrete: Theoretical and Experimental Studies." Stockholm, Sweden: KTH Architecture and The Built Environment. http://www.diva-portal.org/smash/get/diva2:647411/FULLTEXT01.pdf.

Jeandin, Michel Arrigoni Michel Boustie Cyril Bolis Sophie Barradas Laurent Berthe Michel. 2012. "Shock Mechanics and Interfaces." In *Mechanics of Solid Interfaces*, edited by Muriel Braccini Michel Dupeux.

Jiang, Hua, and Jidong Zhao. 2015. "Calibration of the Continuous Surface Cap Model for Concrete." *Finite Elements in Analysis and Design* 97: 1–19. https://doi.org/10.1016/j.finel.2014.12.002.

Jiang, Nan, and Chuanbo Zhou. 2012. "Blasting Vibration Safety Criterion for a Tunnel Liner Structure." *Tunnelling and Underground Space Technology* 32: 52–57. https://doi.org/10.1016/j.tust.2012.04.016.

Johnson, Gordon R. 1983. "A Constitutive Model and Data for Metals Subjected to Large Strains, High Strain Rates and High Temperatures." In *Proceedings of the 7th International Symposium on Ballistics*. The Hague, Netherlands.

Jr, Don van Natta, and Elaine Sciolino. 2005. "Bombing Suspect Killed in Subway by London Police." *The New York Times*, July 23, 2005, sec. World. https://www.nytimes.com/2005/07/23/international/bombing-suspect-killed-in-subway-by-london-police.html.

Kalifa, Pierre, François-Dominique Menneteau, and Daniel Quenard. 2000. "Spalling and Pore Pressure in HPC at High Temperatures." *Cement and Concrete Research*, Papers presented at the Symposium on "Transport Properties and Microstructure of Cement-Based Systems," 30 (12): 1915–27. https://doi.org/10.1016/S0008-8846(00)00384-7.

Kandil, Kamel S., Mouhamad T. Nemir, Ehab A. Ellobody, and Ramy I. Shahin. 2014. "Strain Rate Effect on the Response of Blast Loaded Reinforced Concrete Slabs." *World Journal of Engineering and Technology* 02 (04): 260–68. https://doi.org/10.4236/wjet.2014.24027.

Khoury, Gabriel Alexander. 2000. "Effect of Fire on Concrete and Concrete Structures." *Progress in Structural Engineering and Materials* 2 (4): 429–47. https://doi.org/10.1002/pse.51.

Kodur, V. K. R. 2000. "Spalling in High Strength Concrete Exposed to Fire: Concerns, Causes, Critical Parameters and Cures." In *Advanced Technology in Structural Engineering*, 1–9.

Kolymbas, Dimitrios, ed. 2005. "Earthquake Effects on Tunnels." In *Tunnelling and Tunnel Mechanics: A Rational Approach to Tunnelling*, 337–39. Berlin, Heidelberg: Springer. https://doi.org/10.1007/3-540-28500-8_18.

Kong, Xiangzhen, Qin Fang, Q. M. Li, Hao Wu, and John E. Crawford. 2017. "Modified K&C Model for Cratering and Scabbing of Concrete Slabs under Projectile Impact." *International Journal of Impact Engineering* 108: 217–28. https://doi.org/10.1016/j.ijimpeng.2017.02.016.

Kurioka, Hitoshi, Yasushi Oka, Hiroomi Satoh, and Osami Sugawa. 2003. "Fire Properties in near Field of Square Fire Source with Longitudinal Ventilation in Tunnels." *Fire Safety Journal* 38 (4): 319–40. https://doi.org/10.1016/S0379-7112(02)00089-9.

Kutter, B. L., O'Leary, L. M., Thompson, P. Y., & Lather, R. 1988. "GRAVITY-SCALED TESTS ON BLAST-INDUCED SOIL-STRUCTURE INTERACTION" 114 (4): 431–47.

Le, Q. X., V. T. N. Dao, C. Maluk, J. Torero, and L. Bisby. 2016. "An Investigation into Temperature Gradient Effects on Concrete Performance at Elevated Temperatures." In *The 24th Australasian Conference on the Mechanics of Structures and Materials (ACMSM24)*.

Li, Jianbin. 2017. "Key Technologies and Applications of the Design and Manufacturing of Non-Circular TBMs." *Engineering* 3 (6): 905–914.

Li, Jun, and Hong Hao. 2014. "Numerical Study of Concrete Spall Damage to Blast Loads." *International Journal of Impact Engineering* 68: 41–55. https://doi.org/10.1016/j.ijimpeng.2014.02.001.

Li, Jun, Chengqing Wu, and Hong Hao. 2015. "Investigation of Ultra-High Performance Concrete Slab and Normal Strength Concrete Slab under Contact Explosion." *Engineering Structures* 102: 395–408. https://doi.org/10.1016/j.engstruct.2015.08.032.

Li, Jun, Chengqing Wu, Hong Hao, Zhongqi Wang, and Yu Su. 2016. "Experimental Investigation of Ultra-High Performance Concrete Slabs under Contact Explosions." *International Journal of Impact Engineering* 93: 62–75. https://doi.org/10.1016/j.ijimpeng.2016.02.007.

Liu, Huabei. 2009. "Dynamic Analysis of Subway Structures under Blast Loading." *Geotechnical and Geological Engineering* 27 (6): 699–711. https://doi.org/10.1007/s10706-009-9269-9.

Liu, Jin-Cheng, Kang Hai Tan, and Yao Yao. 2018. "A New Perspective on Nature of Fire-Induced Spalling in Concrete." *Construction and Building Materials* 184 (September): 581–90. https://doi.org/10.1016/j.conbuildmat.2018.06.204.

Livermore Software Technology Corporation. 2014. *LS-DYNA Keyword User's Manual Volume II R7.1. Materials & Design*. Vol. II. https://doi.org/10.1007/978-3-540-69451-9.

Luccioni, B., F. Isla, R. Codina, D. Ambrosini, R. Zerbino, G. Giaccio, and M. C. Torrijos. 2017. "Effect of Steel Fibers on Static and Blast Response of High Strength Concrete." *International Journal of Impact Engineering* 107: 23–37. https://doi.org/10.1016/j.ijimpeng.2017.04.027.

Maluk, Cristian, Luke Bisby, Michal Krajcovic, and Jose Luis Torero. 2016. "A Heat-Transfer Rate Inducing System (H-TRIS) Test Method." *Fire Safety Journal*, June. https://doi.org/10.1016/j.firesaf.2016.05.001.

Malvar, L. Javier, John E. Crawford, James W. Wesevich, and Don Simons. 1997. "A Plasticity Concrete Material Model for DYNA3D." *International Journal of Impact Engineering* 19 (9–10): 847–73. https://doi.org/10.1016/s0734-743x(97)00023-7.

Mao, L., S. J. Barnett, A. Tyas, J. Warren, G. K. Schleyer, and S. S. Zaini. 2015. "Response of Small Scale Ultra High Performance Fibre Reinforced Concrete Slabs to Blast Loading." *Construction and Building Materials* 93: 822–30. https://doi.org/10.1016/j.conbuildmat.2015.05.085.

McGrattan, Kevin B, Howard R Baum, and Anthony Hamins. 2000. "Thermal Radiation from Large Pool Fires." NIST IR 6546. Gaithersburg, MD: National Institute of Standards and Technology.

McGrattan, Kevin B., Randall J. McDermott, Craig G. Weinschenk, and Glenn P. Forney. 2013. "Fire Dynamics Simulator, Technical Reference Guide, Sixth Edition." *Special Publication (NIST SP) - 1018*, November.

McVay, Mark K. 1988. "Spall Damage of Concrete Structurtes." Department of the Army SL-88-22. Vicksburg, MS: Waterways Experiment Station.

Mobaraki, Behnam, and Mohammad Vaghefi. 2015. "Numerical Study of the Depth and Cross-Sectional Shape of Tunnel under Surface Explosion." *Tunnelling and Underground Space Technology* 47: 114–22. https://doi.org/10.1016/j.tust.2015.01.003.

Muñoz, Miguel, Eulàlia Planas, Fabio Ferrero, and Joaquim Casal. 2007. "Predicting the Emissive Power of Hydrocarbon Pool Fires." *Journal of Hazardous Materials* 144 (3): 725–29.

Murray, Yvonne. 2007. "Users Manual for LS-DYNA Concrete Material Model 159." *Federal Highway Administration*, no. May: 77.

Murray, Yvonne, Akram Abu-Odeh, and Roger Bligh. 2007. "Evaluation of LS-DYNA Concrete Material Model 159." *Federal Highway Administration*, no. May: 206.

Naito, Clay, Joe States, Christopher Jackson, and Bryan Bewick. 2014. "Crumb Rubber Concrete Performance under Near-Field Blast and Ballistic Demands." *Journal of Materials in Civil Engineering* 26 (9): 1–10. https://doi.org/10.1061/(ASCE)MT.1943-5533.0000957.

Olmati, Pierluigi, Francesco Petrini, and Konstantinos Gkoumas. 2014. "Fragility Analysis for the Performance-Based Design of Cladding Wall Panels Subjected to Blast Load." *Engineering Structures* 78: 112–20. https://doi.org/10.1016/j.engstruct.2014.06.004.

Piotrowska, E., P. Forquin, and Y. Malecot. 2016. "Experimental Study of Static and Dynamic Behavior of Concrete under High Confinement: Effect of Coarse Aggregate Strength." *Mechanics of Materials* 92: 164–74. https://doi.org/10.1016/j.mechmat.2015.09.005.

Quiel, Spencer E., Takayuki Yokoyama, Lynne S. Bregman, Kevin A. Mueller, and Shalva M. Marjanishvili. 2015. "A Streamlined Framework for Calculating the Response of Steel-Supported Bridges to Open-Air Tanker Truck Fires." *Fire Safety Journal* 73 (April): 63–75.

Riedel W. 2000. "Beton Unter Dynamischen Lasten : Meso- Und Makromechanische Modelle Und Ihre Parameter." Universiẗat der Bundeswehr.

Riedel, Werner, Nobuaki Kawai, and Ken ichi Kondo. 2009. "Numerical Assessment for Impact Strength Measurements in Concrete Materials." *International Journal of Impact Engineering* 36 (2): 283–93. https://doi.org/10.1016/j.ijimpeng.2007.12.012.

Riedel, Werner, Markus Wicklein, and Klaus Thoma. 2008. "Shock Properties of Conventional and High Strength Concrete: Experimental and Mesomechanical Analysis." *International Journal of Impact Engineering* 35 (3): 155–71. https://doi.org/10.1016/j.ijimpeng.2007.02.001.

Robert McNeel & Associates. 2014. *Grasshopper*.

———. 2017. *Rhinoceros*.

Root, Kyle. 2018. "Development and Verification of a Confined Discretized Solid Flame Model for Calculating Heat Flux on Concrete Tunnel Liners." Bethlehem, PA: Lehigh University.

Root, Kyle, Qi Guo, Spencer Quiel, and C. J. Naito. 2018. "Calculating Fire-Induced Heat Flux Contours on Concrete Tunnel Liners to Evaluate Structural Consequences." In *10th International Conference on Structures in Fire: Structures in Fire*, 17–24. Belfast, UK: Ulster University.

Schwer, Len. 2010. "An Introduction to the Winfrith Concrete Model." *Schwer Engineering & Consulting Services*, no. April: 1–28.

Schwer, Leonard E., and Yvonne D. Murray. 1994. "A Three-invariant Smooth Cap Model with Mixed Hardening." *International Journal for Numerical and Analytical Methods in Geomechanics* 18 (10): 657–88. https://doi.org/10.1002/nag.1610181002.

Shorter, G. W., and T. Z. Harmathy. 1961. "Discussion on the Fire Resistance of Prestressed Concrete Beams." *Proceedings of the Institution of Civil Engineers* 20 (2): 313–315.

Siddapureddy, Sudheer. 2013. "Characterization of Open Pool Fires and Study of Heat Transfer in Bodies Engulfed in Pool Fires." Indian Institute of Technology Dharwad.

Soheyli, Mohamad Reza, A. H. Akhaveissy, and S. M. Mirhosseini. 2016. "Large-Scale Experimental and Numerical Study of Blast Acceleration Created by Close-in Buried Explosion on Underground Tunnel Lining." *Shock and Vibration* 2016. https://doi.org/10.1155/2016/8918050.

Sudeep, Kota, and V. Narasimha Rao. 2019. "Structures to Resist the Effects of the Accidental Explosions." *International Journal of Trend in Scientific Research and Development* Volume-3 (Issue-3): 1528–30. https://doi.org/10.31142/ijtsrd23455.

Tabatabaei, Zahra S., Jeffery S. Volz, Jason Baird, Benjamin P. Gliha, and Darwin I. Keener. 2013. "Experimental and Numerical Analyses of Long Carbon Fiber Reinforced Concrete Panels Exposed to Blast Loading." *International Journal of Impact Engineering* 57: 70–80. https://doi.org/10.1016/j.ijimpeng.2013.01.006.

The Japan Times NEWS. 2012. "Blast Rips through Niigata Tunnel." The Japan Times NEWS. 2012. https://www.japantimes.co.jp/news/2012/05/25/national/blast-rips-through-niigata-tunnel/#.Xl3XZqhKiUl.

Tu, Zhenguo, and Yong Lu. 2009. "Evaluation of Typical Concrete Material Models Used in Hydrocodes for High Dynamic Response Simulations." *International Journal of Impact Engineering* 36 (1): 132–46. https://doi.org/10.1016/j.ijimpeng.2007.12.010.

———. 2010. "Modifications of RHT Material Model for Improved Numerical Simulation of Dynamic Response of Concrete." *International Journal of Impact Engineering* 37 (10): 1072–82. https://doi.org/10.1016/j.ijimpeng.2010.04.004.

Vorechovská, Dita. 2019. "RELATION BETWEEN SPALLING BEHAVIOUR AND WATER CONTENT OF CONCRETE," June.

Vu, Xuan Hong, Yann Malecot, Laurent Daudeville, and Eric Buzaud. 2009. "Experimental Analysis of Concrete Behavior under High Confinement: Effect of the Saturation Ratio." *International Journal of Solids and Structures* 46 (5): 1105–20. https://doi.org/10.1016/j.ijsolstr.2008.10.015.

Wang, Yongdong, Alexandros Vouros, Jianping Zhang, and Michael A. Delichatsios. 2017. "Numerical and Experimental Validation Study of Flame Extent of a Pool Fire under the Ceiling." *Journal of Loss Prevention in the Process Industries* 49 (September): 652–59. https://doi.org/10.1016/j.jlp.2017.04.029.

Wu, Chengqing, Gianni Fattori, Andrew Whittaker, and Deric John Oehlers. 2010. "Investigation of Air-Blast Effects from Spherical-and Cylindrical-Shaped Charges." *International Journal of Protective Structures* 1 (3): 345–62. https://doi.org/10.1260/2041-4196.1.3.345.

Wu, Chengqing, Ratni Nurwidayati, and Deric John Oehlers. 2009. "Fragmentation from Spallation of RC Slabs Due to Airblast Loads." *International Journal of Impact Engineering* 36 (12): 1371–76. https://doi.org/10.1016/j.ijimpeng.2009.03.014.

Wu, J., and S. H. Chew. 2014. "Field Performance and Numerical Modeling of Multi-Layer Pavement System Subject to Blast Load." *Construction and Building Materials* 52: 177–88. https://doi.org/10.1016/j.conbuildmat.2013.11.035.

Wu, Jun. 2012. "DEVELOPMENT OF ADVANCED PAVEMENT MATERIALS SYSTEM FOR BLAST LOAD." *Dissertation*. DEVELOPMENT OF ADVANCED PAVEMENT MATERIALS SYSTEM FOR BLAST LOAD WU JUN NATIONAL UNIVERSITY OF SINGAPORE.

Wu, Youcai, John E Crawford, and Joseph M Magallanes. 2012. "Concrete Constitutive Models." *12th International LS-DYNA Users Conference*, no. 1: 1–14.

Xu, Kai, and Yong Lu. 2006. "Numerical Simulation Study of Spallation in Reinforced Concrete Plates Subjected to Blast Loading." *Computers and Structures* 84 (5–6): 431–38. https://doi.org/10.1016/j.compstruc.2005.09.029.

Yamaguchi, Makoto, Kiyoshi Murakami, Koji Takeda, and Yoshiyuki Mitsui. 2011. "Blast Resistance of Double-Layered Reinforced Concrete Slabs Composed of Precast Thin Plates." *Journal of Advanced Concrete Technology* 9 (2): 177–91. https://doi.org/10.3151/jact.9.177.

Yang, Yubing, Xiongyao Xie, and Rulu Wang. 2010. "Numerical Simulation of Dynamic Response of Operating Metro Tunnel Induced by Ground Explosion." *Journal of Rock Mechanics and Geotechnical Engineering* 2 (4): 373–84. https://doi.org/10.3724/SP.J.1235.2010.00373.

Yi, Liang, Ran Huo, Jing-yan Zhang, Yuan-zhou LI, and He-ping ZHANG. 2006. "Characteristics of Heat Release Rate of Diesel Oil Pool Fire." *Journal of Combustion Science and Technology* 2: 015.

Yi, Na Hyun, Jang Ho Jay Kim, Tong Seok Han, Yun Gu Cho, and Jang Hwa Lee. 2012. "Blast-Resistant Characteristics of Ultra-High Strength Concrete and Reactive Powder Concrete." *Construction and Building Materials* 28 (1): 694–707. https://doi.org/10.1016/j.conbuildmat.2011.09.014.

Yonhap News Agency. 2017. "Yonhap News." Yonhap News. 2017.

Yu, Haitao, Yong Yuan, Guangxi Yu, and Xian Liu. 2014. "Evaluation of Influence of Vibrations Generated by Blasting Construction on an Existing Tunnel in Soft Soils." *Tunnelling and Underground Space Technology* 43: 599–566. https://doi.org/10.1016/j.tust.2014.04.005.

Zhang, L., S. S. Hu, D. X. Chen, Z. Q. Yu, and F. Liu. 2009. "An Experimental Technique for Spalling of Concrete." *Experimental Mechanics* 49 (4): 523–32. https://doi.org/10.1007/s11340-008-9159-8.

Zhang, Shu, Yubin Lu, Xing Chen, Xiao Teng, and Shuisheng Yu. 2016. "Further Investigation on the Real Rate Effect of Dynamic Tensile Strength for Concrete-like Materials." *Latin American Journal of Solids and Structures* 13 (1): 201–23. https://doi.org/10.1590/1679-78251973.

Zhao, C. F., and J. Y. Chen. 2013. "Damage Mechanism and Mode of Square Reinforced Concrete Slab Subjected to Blast Loading." *Theoretical and Applied Fracture Mechanics* 63–64: 54–62. https://doi.org/10.1016/j.tafmec.2013.03.006.

Zhou, Kuibin, Naian Liu, Linhe Zhang, and Koyu Satoh. 2014. "Thermal Radiation from Fire Whirls: Revised Solid Flame Model." *Fire Technology* 50 (6): 1573–87.

Zhou, X. Q., V. A. Kuznetsov, H. Hao, and J. Waschl. 2008. "Numerical Prediction of Concrete Slab Response to Blast Loading." *International Journal of Impact Engineering* 35 (10): 1186–1200. https://doi.org/10.1016/j.ijimpeng.2008.01.004.

Zukas, Jonas a. 2004. *Introduction to Hydrocodes. Studies in Applied Mechanics*. Vol. 49. https://doi.org/10.1016/S0922-5382(04)80009-6.

Appendix A: Technology Transfer Activities

1 Accomplishments

An extensive numerical evaluation of concrete lining under blast loading was conducted. LS-DYNA was employed to develop a deeper understanding of the failure mechanisms that develop in response to close-in blast loading. Parameters effecting damage for a given charge size were numerically evaluated: backfill material, liner thickness and strength. The behavior of concrete lining under fire conditions was investigated both numerically and experimentally. An experimental program was initiated to investigate the effect of pertinent parameters on the propensity of thermal spalling, including rebar density, applied axial stress, and magnitude of thermal exposure. Fabrication of an experimental test fixture was completed. The test setup has been calibrated, and preliminary tests have been performed. Preliminary spalling evaluations have been integrated with the total damage mapping tool developed utilizing the confined discretized solid flame model allowing conservative prediction of tunnel liner damage for a given fire event.

1.1 What was done? What was learned?

For blast:

(1) Blast effects in tunnels can result in localized failure of the concrete tunnel liner as a result of spall or breach of the concrete from close-in detonations.

(2) The spalling mechanism of concrete slab in blast has been theoretically and numerically studied, the reflection of stress waves at the free surface causes the occurrence of tensile stress and concrete spall. Hence, changing the backfill impedance is an efficient method to mitigate the spalling.

(3) The stress wave propagation is analyzed numerically based on accepted approaches used in the literature.

(4) Appropriate concrete model are selected using finite element software LS-DYNA to simulate the behavior of concrete slab as well as concrete tunnel lining subjected to blast. The simulated the results fit the past experimental observations of damage formation well.

(5) The spalling of tunnel liners is alleviated by changing the property of backfill. By increasing the backfill impedance, the tensile stress in concrete become compression.

(6) Damage due to blast events on backed tunnel liners can be mitigated by utilizing grout with comparable density and elastic modulus as the concrete tunnel liner. This will move any reflected damage to the outer region of the grout, away from the structural liner.

For Fire

(1) An equivalent diesel pool fire was proposed to represent vehicle fire with the same HRR to simplify the modeling of varying material composition and flame shape in realistic vehicle fires.

(2) A confined discretized solid flame model (CDSF) is proposed to provide an accurate and robust assessment of incident heat fluxes on circular tunnel cross sections.

(3) Fire-induced spalling damage is mapped using simplified predictive models that utilize the thermal demands calculated by the CDSF model, thereby providing a visual, holistic evaluation of direct consequences from large tunnel fires.

(4) The damage to the tunnel liner can be significant for large fire events. Given that vehicular accidents and subsequent fires are much more prevalent than accidental or intentional blast events a focused research effort on determination of the fire resistance of concrete liners is conducted.

(5) The preliminary experimentation was successful in establishing the capabilities of the refined testing apparatus to evaluate performance near the ASTM E1529 hydrocarbon fire thermal loading intensities. Concrete material behavior under thermal loading can be evaluated in a consistent and repeatable fashion for variation in axial load/restraint, heat flux intensity, moisture conditions, mix designs, and reinforcement details.

(6) The observation of a threshold between 70 and 80 kW/m^2 was required to exhibit spalling behavior. This observation is contingent upon the specific experimental apparatus discussed herein and requires additional focused experimentation to verify for different concrete mix designs and heating rates.

(7) Internal concrete temperatures far exceeding the boiling point of water were observed in specimens that did not exhibit spalling behavior. Therefore, the observation that peak temperature and heating rate must be considered to assess the likelihood of concrete spalling behavior.

1.2 How have the results been disseminated?

- The results were presented at *1st Annual UTC-UTI Workshop*, Colorado School of Mines, Golden, February 2018.

- The results were presented at *Tunneling Fundamentals, Practice and Innovations Short Course*, Colorado School of Mines, Golden, October 2018.

- The results were presented at *Transportation Research Board (TRB) 98th Annual Meeting*, Washington DC, 2019.

2 Participants and Collaborating Organizations

Name: Lehigh University

Location: Bethlehem, PA

Contribution: (1) A semi-empirical solid flame model (CDSF model) was developed for rapid and accurate prediction of steady-state incident heat flux received by the tunnel linings due to vehicle fire. (2) Numerical modeling approach in FDS for the tunnel fire analyses was validated against full-scale tunnel fire tests with various tunnel geometry and fire sizes. (3) Simple spall prediction criteria were implemented with the CDSF model to illustrate the evaluation of structural damage in the proposed framework for fire hazard consequences for tunnel structures.

3 Outputs

Journal publications

- Qi Guo "Streamlined Calculation of Fire-Induced Heat Flux and Resulting Spalling Damage for Concrete Tunnel Liners" at *Transportation Research Board (TRB) 98th Annual Meeting, Washington DC*, Jan 2019

Workshops

- Qi Guo, Kyle Root "Tunnel Liner Damage due to Fire and Blast: Fast-Running Predictions and Upcoming Test Programs" at *Tunneling Fundamentals, Practice and Innovations Short Course*, Colorado School of Mines, Golden, 2018

4 Outcomes

- The behavior of concrete slab subjected to blast can be analytically and numerically studied. Appropriate concrete model is chosen (RHT model) to represent the dynamic behavior of concrete with high stain rate.

- Stress waves in concrete can become tensile only when the backfill impedance is lower than the concrete itself and if the backfill impedance is higher than the concrete the transmitted waves become compressive.

- The equivalent diesel pool fire is proposed for vehicle fire modelling as a simplification of the various materials on the vehicle which result in complex combustion behaviors. The HRR is used as the key factor to represent the intensity of the fire while achieving equivalence between the pool fire and the vehicle fire.

- The CDSF model can predict the spatial distribution of the steady-state heat flux received by the tunnel linings in a fire event with very high computational efficiency, which makes it able to do preliminary and stochastic analyses. The fast-running tool evaluate the vulnerability of the tunnel linings to fire-induced heating based on the specific case such as the geometry of the tunnel.

5 Impacts

- The CDSF model can be used to supplement the current tools for tunnel fire analyses which provides conservatively accurate results with high computational efficiency. Fire risk assessment for tunnel structure which might require stochastic analyses would be much more practical to perform with the CDSF model as well as parametric investigation of fire vulnerability for a tunnel inventory.
- A fire testing fixture has been developed and is available for experimental evaluation of spall mechanisms in concrete liners.

Appendix B: Data from the Project

Figure 39 *Comparison of experimental and FDS ceiling temperatures during the 20 MW and 50 MW diesel test fires in the Memorial Tunnel*				
	20MW Fire		50MW Fire	
Longitudinal distance from fire (m)	Ceiling Temperature Measured (°C)	Ceiling Temperature in FDS (°C)	Ceiling Temperature Measured (°C)	Ceiling Temperature in FDS (°C)
-62	149	195	316	323
-29	204	233	482	412
-20	NA	277	NA	552
-15	NA	294	NA	628
-11	260	323	704	722
-5	NA	340	NA	862
-1.5	260	353	760	793
5	NA	304	NA	560
12	316	267	427	428
15	NA	256	NA	397
20	NA	240	NA	356
30	204	194	260	287
66	93	100	149	155

Figure 45-46

CDSF (30MW)								
	CEILING			SIDEWALL			CROSS SECTION		
x (m)	TOTAL	RADI	CONV	TOTAL	RADI	CONV	TOTAL	RADI	CONV
-54	0	0	0	0	0	0	9	9	0
-52	0	0	0	0	0	0	10	10	0
-50	0	0	0	0	0	0	11	11	0
-48	0	0	0	0	0	0	12	12	0
-46	0	0	0	0	0	0	13	13	0
-44	0	0	0	0	0	0	14	14	0
-42	0	0	0	0	0	0	15	15	0
-40	0	0	0	0	0	0	16	16	0
-38	0	0	0	0	0	0	17	17	0

CDSF (30MW)									
	CEILING			**SIDEWALL**			**CROSS SECTION**		
x (m)	**TOTAL**	**RADI**	**CONV**	**TOTAL**	**RADI**	**CONV**	**TOTAL**	**RADI**	**CONV**
-36	0	0	0	0	0	0	19	19	0
-34	0	0	0	0	0	0	22	21	1
-32	0	0	0	0	0	0	26	23	3
-30	0	0	0	0	0	0	31	28	3
-28	0	0	0	0	0	0	44	41	3
-26	0	0	0	0	0	0	31	28	3
-24	0	0	0	0	0	0	26	23	3
-22	1	0	1	0	0	0	22	21	1
-20	1	0	1	0	0	0	19	19	0
-18	1	0	1	0	0	0	17	17	0
-16	1	0	1	1	1	0	16	16	0
-14	1	1	0	1	1	0	15	15	0
-12	2	1	1	1	1	0	14	14	0
-10	2	1	1	2	2	0	13	13	0
-8	4	2	2	3	3	0	12	12	0
-6	6	4	2	5	5	0	11	11	0
-4	10	7	3	8	8	0	10	10	0
-2	19	16	3	11	11	0	9	9	0
0	44	41	3	13	13	0			
2	19	16	3	11	11	0			
4	10	7	3	8	8	0			
6	6	4	2	5	5	0			
8	4	2	2	3	3	0			
10	2	1	1	2	2	0			
12	2	1	1	1	1	0			
14	1	1	0	1	1	0			
16	1	0	1	1	1	0			
18	1	0	1	0	0	0			
20	1	0	1	0	0	0			
22	1	0	1	0	0	0			
24	0	0	0	0	0	0			
26	0	0	0	0	0	0			
28	0	0	0	0	0	0			
30	0	0	0	0	0	0			
32	0	0	0	0	0	0			
34	0	0	0	0	0	0			
36	0	0	0	0	0	0			
38	0	0	0	0	0	0			

CDSF (30MW)

x (m)	CEILING TOTAL	CEILING RADI	CEILING CONV	SIDEWALL TOTAL	SIDEWALL RADI	SIDEWALL CONV	CROSS SECTION TOTAL	CROSS SECTION RADI	CROSS SECTION CONV
40	0	0	0	0	0	0			
42	0	0	0	0	0	0			
44	0	0	0	0	0	0			
46	0	0	0	0	0	0			
48	0	0	0	0	0	0			
50	0	0	0	0	0	0			
52	0	0	0	0	0	0			
54	0	0	0	0	0	0			

FDS (30MW)

x (m)	CEILING UB	CEILING MEAN	CEILING LB	SIDEWALL UB	SIDEWALL MEAN	SIDEWALL LB	CROSS SECTION UB	CROSS SECTION MEAN	CROSS SECTION LB
-55	2.06	1.75	1.43	0.56	0.53	0.51	10.52	9.20	7.89
-50	2.17	1.84	1.50	0.57	0.54	0.51	11.41	9.97	8.53
-45	2.31	1.96	1.61	0.58	0.55	0.52	13.94	12.27	10.61
-40	2.47	2.09	1.71	0.59	0.56	0.54	11.89	10.33	8.77
-35	2.64	2.23	1.82	0.61	0.58	0.55	13.64	11.71	9.78
-30	2.83	2.38	1.93	0.63	0.60	0.57	13.26	11.34	9.41
-25	3.12	2.60	2.08	0.68	0.64	0.61	13.95	11.67	9.40
-20	3.48	2.86	2.25	0.84	0.80	0.75	11.85	9.99	8.13
-18	3.66	2.99	2.32	1.01	0.94	0.88	9.46	7.55	5.64
-16	3.87	3.13	2.39	1.25	1.17	1.08	13.08	9.04	5.01
-15	3.98	3.20	2.42	1.40	1.30	1.20	20.64	12.66	4.68
-14	4.10	3.27	2.45	1.55	1.44	1.32	34.86	19.72	4.57
-12	4.38	3.44	2.50	1.85	1.69	1.53	53.84	30.96	8.09
-10	4.64	3.58	2.53	1.87	1.69	1.51	71.51	42.63	13.74
-8	6.04	4.33	2.63	3.64	3.19	2.74	61.69	36.72	11.74
-6	8.88	5.77	2.65	5.27	4.58	3.90	39.74	23.41	7.08
-5	11.78	7.19	2.60	6.41	5.55	4.69	19.97	12.90	5.84
-4	15.73	9.10	2.48	7.31	6.34	5.37	12.53	9.21	5.88
-2	44.32	24.26	4.21	11.39	9.78	8.16	9.35	7.70	6.04
0	71.51	42.63	13.74	13.64	11.71	9.78	11.87	10.15	8.44
2	36.31	20.34	4.37	11.12	9.53	7.94	14.01	11.85	9.70
4	15.62	9.63	3.63	7.74	6.73	5.72	13.36	11.53	9.69
5	10.38	6.61	2.84	6.19	5.38	4.56	13.76	11.92	10.09
6	7.98	5.44	2.90	5.07	4.44	3.80	12.01	10.53	9.04
8	5.74	4.24	2.74	3.51	3.11	2.70	14.06	12.50	10.94

	CEILING			SIDEWALL			CROSS SECTION		
FDS (30MW)									
x (m)	UB	MEAN	LB	UB	MEAN	LB	UB	MEAN	LB
10	4.95	3.81	2.67	2.61	2.34	2.07	11.53	10.17	8.82
12	4.39	3.46	2.53	1.79	1.65	1.51	10.65	9.44	8.23
14	4.12	3.30	2.47	1.48	1.38	1.28			
15	4.00	3.22	2.44	1.32	1.24	1.16			
16	3.89	3.15	2.41	1.18	1.11	1.04			
18	3.68	3.02	2.35	0.96	0.91	0.86			
20	3.51	2.90	2.28	0.81	0.77	0.73			
25	3.16	2.64	2.12	0.67	0.64	0.61			
30	2.91	2.45	2.00	0.64	0.61	0.57			
35	2.67	2.26	1.86	0.61	0.58	0.55			
40	2.49	2.11	1.74	0.59	0.56	0.54			
45	2.33	1.98	1.64	0.58	0.55	0.53			
50	2.21	1.88	1.55	0.57	0.54	0.52			
55	2.08	1.76	1.45	0.56	0.53	0.51			

	CEILING			SIDEWALL			CROSS SECTION		
CDSF (70MW)									
x (m)	TOTAL	RADI	CONV	TOTAL	RADI	CONV	TOTAL	RADI	CONV
-54	3	0	3	0	0	0	11	11	0
-52	3	0	3	0	0	0	12	12	0
-50	3	0	3	0	0	0	14	14	0
-48	3	0	3	0	0	0	16	16	0
-46	3	0	3	0	0	0	17	17	0
-44	3	0	3	0	0	0	19	19	0
-42	4	0	4	0	0	0	22	22	0
-40	4	0	4	0	0	0	25	25	0
-38	4	0	4	0	0	0	43	31	12
-36	4	0	4	0	0	0	63	40	23
-34	5	0	5	0	0	0	83	52	31
-32	5	0	5	0	0	0	102	65	37
-30	5	0	5	0	0	0	123	82	41
-28	6	0	6	0	0	0	138	96	42
-26	6	0	6	0	0	0	123	82	41
-24	7	0	7	0	0	0	102	65	37
-22	8	0	8	0	0	0	83	52	31
-20	9	0	9	0	0	0	63	40	23
-18	10	1	9	1	1	0	43	31	12

CDSF (70MW)									
	CEILING			**SIDEWALL**			**CROSS SECTION**		
x (m)	**TOTAL**	**RADI**	**CONV**	**TOTAL**	**RADI**	**CONV**	**TOTAL**	**RADI**	**CONV**
-16	12	1	11	1	1	0	25	25	0
-14	14	1	13	1	1	0	22	22	0
-12	18	2	16	2	2	0	19	19	0
-10	23	3	20	3	3	0	17	17	0
-8	31	5	26	5	5	0	16	16	0
-6	49	13	36	9	9	0	14	14	0
-4	78	36	42	12	12	0	12	12	0
-2	117	75	42	16	16	0	11	11	0
0	138	96	42	17	17	0			
2	117	75	42	16	16	0			
4	78	36	42	12	12	0			
6	49	13	36	9	9	0			
8	31	5	26	5	5	0			
10	23	3	20	3	3	0			
12	18	2	16	2	2	0			
14	14	1	13	1	1	0			
16	12	1	11	1	1	0			
18	10	1	9	1	1	0			
20	9	0	9	0	0	0			
22	8	0	8	0	0	0			
24	7	0	7	0	0	0			
26	6	0	6	0	0	0			
28	6	0	6	0	0	0			
30	5	0	5	0	0	0			
32	5	0	5	0	0	0			
34	5	0	5	0	0	0			
36	4	0	4	0	0	0			
38	4	0	4	0	0	0			
40	4	0	4	0	0	0			
42	4	0	4	0	0	0			
44	3	0	3	0	0	0			
46	3	0	3	0	0	0			
48	3	0	3	0	0	0			
50	3	0	3	0	0	0			
52	3	0	3	0	0	0			
54	3	0	3	0	0	0			

FDS (60MW)								
	CEILING			**SIDEWALL**			**CROSS SECTION**		
x (m)	**UB**	**MEAN**	**LB**	**UB**	**MEAN**	**LB**	**UB**	**MEAN**	**LB**
-55	4.93	4.26	3.58	0.73	0.68	0.64	17.77	16.32	14.88
-50	5.32	4.59	3.87	0.75	0.71	0.66	19.42	17.72	16.01
-45	5.88	5.08	4.28	0.80	0.75	0.69	25.86	23.81	21.77
-40	6.51	5.60	4.69	0.84	0.79	0.73	22.43	20.54	18.66
-35	7.28	6.24	5.19	0.90	0.84	0.78	26.50	24.05	21.59
-30	8.17	6.94	5.70	0.97	0.90	0.83	25.13	22.65	20.16
-25	9.62	8.05	6.48	1.10	1.03	0.95	30.73	25.16	19.58
-20	11.57	9.45	7.33	1.44	1.35	1.26	39.71	29.49	19.26
-18	12.61	10.15	7.70	1.73	1.63	1.53	41.37	27.95	14.54
-16	13.86	10.96	8.06	2.16	2.04	1.91	54.21	36.72	19.23
-15	14.62	11.42	8.22	2.44	2.29	2.15	82.91	55.97	29.02
-14	15.47	11.92	8.36	2.76	2.59	2.42	131.84	89.07	46.30
-12	17.73	13.13	8.54	3.50	3.27	3.04	179.78	126.59	73.40
-10	20.13	14.39	8.64	3.74	3.48	3.21	209.37	150.45	91.53
-8	29.59	19.48	9.36	7.62	7.00	6.37	191.89	135.88	79.86
-6	43.02	26.57	10.13	11.00	10.04	9.08	153.37	102.82	52.27
-5	54.35	33.14	11.94	13.20	12.03	10.87	88.51	58.31	28.11
-4	67.53	41.63	15.73	15.24	13.91	12.58	58.13	38.57	19.02
-2	154.40	102.88	51.36	22.66	20.57	18.48	43.85	29.37	14.89
0	209.37	150.45	91.53	26.50	24.05	21.59	40.71	30.29	19.87
2	146.88	98.20	49.52	22.10	20.15	18.19	31.53	25.73	19.93
4	76.29	47.92	19.55	16.24	14.90	13.55	25.45	22.88	20.31
5	53.71	32.43	11.15	12.80	11.75	10.69	26.87	24.34	21.81
6	42.80	26.27	9.75	10.70	9.83	8.96	22.70	20.79	18.89
8	29.67	19.32	8.97	7.45	6.87	6.30	26.14	24.07	22.00
10	22.72	15.91	9.09	5.53	5.13	4.72	19.70	17.96	16.23
12	17.61	13.06	8.51	3.35	3.14	2.94	18.03	16.57	15.11
14	15.50	11.91	8.32	2.62	2.47	2.32			
15	14.63	11.41	8.19	2.32	2.19	2.06			
16	13.86	10.95	8.04	2.06	1.94	1.83			
18	12.56	10.13	7.70	1.66	1.56	1.47			
20	11.50	9.42	7.34	1.40	1.31	1.22			
25	9.54	8.01	6.48	1.10	1.02	0.94			
30	8.31	7.07	5.82	0.99	0.91	0.84			
35	7.21	6.18	5.15	0.90	0.84	0.77			
40	6.44	5.54	4.65	0.84	0.78	0.72			
45	5.82	5.02	4.23	0.80	0.74	0.69			
50	5.36	4.63	3.90	0.76	0.71	0.67			

FDS (60MW)									
	CEILING			**SIDEWALL**			**CROSS SECTION**		
x (m)	**UB**	**MEAN**	**LB**	**UB**	**MEAN**	**LB**	**UB**	**MEAN**	**LB**
55	4.89	4.22	3.54	0.73	0.68	0.64			

CDSF (200MW)									
	CEILING			**SIDEWALL**			**CROSS SECTION**		
x (m)	**TOTAL**	**RADI**	**CONV**	**TOTAL**	**RADI**	**CONV**	**TOTAL**	**RADI**	**CONV**
-54	24	0	24	0	0	0	23	23	0
-52	25	0	25	0	0	0	30	30	0
-50	25	0	25	0	0	0	34	34	0
-48	27	0	27	0	0	0	38	38	0
-46	28	0	28	0	0	0	41	41	0
-44	29	0	29	0	0	0	43	43	0
-42	30	0	30	0	0	0	83	47	36
-40	32	0	32	0	0	0	123	54	69
-38	33	0	33	0	0	0	175	76	99
-36	35	0	35	0	0	0	227	104	123
-34	37	0	37	0	0	0	267	124	143
-32	39	0	39	0	0	0	295	137	158
-30	42	0	42	0	0	0	308	142	166
-28	45	0	45	0	0	0	321	152	169
-26	49	1	48	1	1	0	308	142	166
-24	53	1	52	1	1	0	295	137	158
-22	57	1	56	1	1	0	267	124	143
-20	63	1	62	1	1	0	227	104	123
-18	70	2	68	2	2	0	175	76	99
-16	80	3	77	3	3	0	123	54	69
-14	92	5	87	5	5	0	83	47	36
-12	109	8	101	7	7	0	43	43	0
-10	137	15	122	12	12	0	41	41	0
-8	190	39	151	19	19	0	38	38	0
-6	263	94	169	27	27	0	34	34	0
-4	296	127	169	34	34	0	30	30	0
-2	309	141	168	39	39	0	23	23	0
0	321	152	169	41	41	0			
2	309	141	168	39	39	0			
4	296	127	169	34	34	0			
6	263	94	169	27	27	0			
8	190	39	151	19	19	0			

CDSF (200MW)

x (m)	CEILING TOTAL	CEILING RADI	CEILING CONV	SIDEWALL TOTAL	SIDEWALL RADI	SIDEWALL CONV	CROSS SECTION TOTAL	CROSS SECTION RADI	CROSS SECTION CONV
10	137	15	122	12	12	0			
12	109	8	101	7	7	0			
14	92	5	87	5	5	0			
16	80	3	77	3	3	0			
18	70	2	68	2	2	0			
20	63	1	62	1	1	0			
22	57	1	56	1	1	0			
24	53	1	52	1	1	0			
26	49	1	48	1	1	0			
28	45	0	45	0	0	0			
30	42	0	42	0	0	0			
32	39	0	39	0	0	0			
34	37	0	37	0	0	0			
36	35	0	35	0	0	0			
38	33	0	33	0	0	0			
40	32	0	32	0	0	0			
42	30	0	30	0	0	0			
44	29	0	29	0	0	0			
46	28	0	28	0	0	0			
48	27	0	27	0	0	0			
50	25	0	25	0	0	0			
52	25	0	25	0	0	0			
54	24	0	24	0	0	0			

FDS (200MW)

x (m)	CEILING UB	CEILING MEAN	CEILING LB	SIDEWALL UB	SIDEWALL MEAN	SIDEWALL LB	CROSS SECTION UB	CROSS SECTION MEAN	CROSS SECTION LB
-55	18.6	15.7	12.7	1.4	1.2	1.0	31.8	25.9	19.9
-50	20.8	17.5	14.1	1.5	1.3	1.1	40.2	32.5	24.9
-45	24.2	20.2	16.2	1.6	1.4	1.3	52.2	42.3	32.4
-40	28.1	23.3	18.6	1.8	1.6	1.4	43.5	35.5	27.5
-35	33.2	27.4	21.6	2.0	1.8	1.6	48.0	40.8	33.7
-30	39.8	32.4	25.1	2.2	2.0	1.8	73.5	59.8	46.2
-25	51.7	41.4	31.1	2.6	2.4	2.2	149.7	121.2	92.7
-20	70.6	55.1	39.7	3.4	3.1	2.9	146.3	121.2	96.1
-18	82.5	63.5	44.6	3.9	3.6	3.3	157.4	129.3	101.2
-16	98.5	74.8	51.0	4.8	4.3	3.8	188.2	156.1	124.1

FDS (200MW)									
	CEILING			**SIDEWALL**			**CROSS SECTION**		
x (m)	**UB**	**MEAN**	**LB**	**UB**	**MEAN**	**LB**	**UB**	**MEAN**	**LB**
-15	108.4	81.8	55.1	5.3	4.7	4.1	242.9	203.7	164.5
-14	119.9	89.9	59.8	5.9	5.2	4.5	303.3	258.3	213.2
-12	147.8	109.7	71.7	7.6	6.6	5.6	343.2	292.9	242.6
-10	172.1	127.2	82.3	8.5	7.3	6.2	378.6	323.6	268.7
-8	223.4	166.4	109.5	17.5	14.9	12.3	355.4	305.1	254.7
-6	267.2	206.0	144.7	24.9	21.1	17.3	325.3	278.9	232.5
-5	298.8	237.1	175.5	29.3	25.0	20.6	246.3	208.6	170.9
-4	325.5	265.9	206.3	33.0	28.2	23.3	191.5	160.4	129.4
-2	367.6	325.1	282.6	43.9	37.3	30.6	160.5	132.5	104.4
0	378.6	323.6	268.7	48.0	40.8	33.7	150.1	124.3	98.6
2	372.3	324.9	277.5	42.9	36.6	30.2	150.8	123.3	95.8
4	333.8	278.3	222.9	34.7	29.4	24.0	71.4	58.9	46.4
5	287.2	229.8	172.5	28.3	23.9	19.5	48.3	40.9	33.5
6	258.2	201.6	145.0	24.2	20.4	16.6	43.9	35.3	26.7
8	216.7	164.0	111.4	17.0	14.4	11.7	52.7	42.1	31.4
10	179.9	135.5	91.1	12.0	10.3	8.5	40.6	32.3	24.0
12	133.9	100.8	67.7	7.3	6.2	5.1	32.2	25.7	19.1
14	108.8	83.0	57.1	5.7	5.0	4.2			
15	99.1	76.0	52.9	5.1	4.5	3.8			
16	90.8	70.0	49.3	4.6	4.1	3.5			
18	77.0	60.2	43.4	3.8	3.5	3.1			
20	66.5	52.6	38.7	3.3	3.0	2.7			
25	49.1	39.7	30.3	2.5	2.3	2.2			
30	39.6	32.5	25.3	2.2	2.0	1.8			
35	31.9	26.4	20.9	1.9	1.7	1.6			
40	27.0	22.5	18.0	1.7	1.6	1.4			
45	23.2	19.5	15.7	1.6	1.4	1.3			
50	20.6	17.3	14.1	1.4	1.3	1.2			
55	17.9	15.2	12.4	1.3	1.2	1.1			

Figure 52: Heat Flux to Standoff Distance Power Curve Comparison

MALUK			30.5 cm x 30.5 cm - 240V w/Screen			25.4 cm x 25.4 cm 208V		
STANDOFF	STANDOFF	HEAT_FLUX	STANDOFF	STANDOFF	HEAT_FLUX	STANDOFF	STANDOFF	HEAT_FLUX
mm	inches	kW/m2	mm	inches	kW/m2	mm	inches	kW/m2
50.0	1.9685	10.0	1.9	0.750	80.9	1.9	0.750	82.6
40.0	1.5748	17.0	5.1	2.000	57.0	5.1	2.000	49.6
32.5	1.2795	21.5	10.2	4.000	39.3	10.2	4.000	31.1

MALUK			30.5 cm x 30.5 cm - 240V w/Screen			25.4 cm x 25.4 cm 208V		
STANDOFF	STANDOFF	HEAT_FLUX	STANDOFF	STANDOFF	HEAT_FLUX	STANDOFF	STANDOFF	HEAT_FLUX
mm	inches	kW/m2	mm	inches	kW/m2	mm	inches	kW/m2
27.0	1.0630	26.7	15.2	6.000	27.7	20.3	8.000	13.8
21.0	0.8268	36.0	20.3	8.000	19.1			
15.0	0.5906	65.0	25.4	10.000	13.8			
10.0	0.3937	96.0						
6.0	0.2362	120.0						

Figure 53: Heat Flux Time History Summary

Metal Foam @ 15.2 cm		Metal Foam @ 18.7 cm		Metal Fiber @ 15.2 cm		Metal Fiber 2 @ 15.2 cm	
Time	Heat Flux	Time	Heat Flux	Time	Heat Flux	Time	Heat Flux
[min]	[kW/m^2]	[min]	[kW/m^2]	[min]	[kW/m^2]	[min]	[kW/m^2]
0	0	0	0	0	0	0	0
0.6075	66.2829	0.6	32.28037	0.6	100.4484	0.604167	95.59922
0.715833	75.58941	0.7	36.80806	0.7	102.6634	0.704167	97.63451
0.8075	80.01846	0.8	38.90254	0.8	104.7953	0.804167	99.33743
0.9075	83.95279	0.9	40.47279	0.904167	106.0522	0.904167	101.0097
1.0075	86.99176	1	41.74078	1.004167	107.9708	1.004167	102.3344
1.1075	89.33118	1.1	42.7593	1.104167	109.3388	1.104167	103.8046
1.2075	91.18932	1.2	43.58748	1.204167	110.6336	1.204167	105.4707
1.3075	92.99988	1.3	44.29282	1.304167	111.497	1.304167	106.8276
1.4075	94.64993	1.4	44.91106	1.404167	112.6755	1.404167	107.9756
1.5075	96.23153	1.5	45.58617	1.504167	113.481	1.504167	109.106
1.6075	97.76516	1.6	46.2248	1.604167	114.1729	1.604167	110.2213
1.7075	99.25815	1.7	46.86542	1.704167	114.9903	1.704167	111.3144
1.8075	100.7291	1.8	47.43871	1.804167	115.6477	1.804167	112.5003
1.9075	102.0453	1.9	47.95979	1.904167	116.008	1.904167	113.925
2.0075	103.3941	2	48.44916	2.004167	116.593	2.004167	114.9706
2.1075	104.6945	2.1	48.90095	2.104167	117.264	2.104167	115.9593
2.2075	106.0496	2.2	49.27332	2.204167	117.8734	2.204167	116.7349
2.3075	107.1212	2.3	49.58192	2.304167	118.2654	2.304167	117.6124
2.4075	108.193	2.4	49.89462	2.404167	118.5737	2.404167	118.2256
2.5075	109.3045	2.5	50.24382	2.504167	119.0121	2.504167	118.832
2.6075	110.2203	2.6	50.61391	2.604167	119.395	2.604167	119.2206
2.7075	110.9592	2.7	51.00088	2.704167	119.7138	2.704167	119.5426
2.8075	111.7697	2.8	51.34577	2.804167	120.3032	2.804167	119.9807
2.9075	112.4285	2.9	51.65165	2.904167	120.7111	2.904167	120.2985
3.0075	113.0178	3	51.91231	3.004167	120.9291	3.004167	120.7303

Metal Foam @ 15.2 cm		Metal Foam @ 18.7 cm		Metal Fiber @ 15.2 cm		Metal Fiber 2 @ 15.2 cm	
Time	Heat Flux	Time	Heat Flux	Time	Heat Flux	Time	Heat Flux
[min]	[kW/m^2]	[min]	[kW/m^2]	[min]	[kW/m^2]	[min]	[kW/m^2]
3.1075	113.4588	3.1	52.12228	3.104167	121.3063	3.104167	121.0645
3.2075	113.8352	3.2	52.31468	3.204167	121.7605	3.204167	121.6806
3.3075	113.8498	3.3	52.49751	3.304167	122.0437	3.304167	122.3289
3.4075	113.8697	3.4	52.74685	3.404167	122.1467	3.404167	123.0755
3.5075	114.131	3.5	52.9982	3.504167	122.4719	3.504167	123.5285
3.6075	114.299	3.6	53.26419	3.604167	122.5897	3.604167	123.87
3.7075	114.4144	3.7	53.5681	3.704167	122.7488	3.704167	124.114
3.8075	114.2141	3.8	53.85316	3.804167	123.0064	3.804167	124.7271
3.9075	114.219	3.9	54.1041	3.904167	123.3819	3.904167	125.4188
4.0075	114.1946	4	54.28229	4.004167	123.5951	4.004167	125.9383
4.2075	114.8097	4.2	54.41736	4.204167	124.1556	4.204167	126.9219
4.4075	115.2015	4.4	54.70524	4.404167	124.6378	4.404167	127.9265
4.6075	115.7823	4.6	55.12223	4.604167	124.8154	4.604167	129.2618
4.8075	116.6676	4.8	55.59047	4.804167	124.9434	4.804167	130.0345
5.0075	117.5073	5	55.90961	5.004167	124.8721	5.004167	130.712
5.2075	118.4393	5.2	56.23519	5.204167	125.0812	5.204167	132.0889
5.4075	119.5276	5.4	56.50148	5.404167	125.4827	5.404167	133.226
5.6075	120.3407	5.6	56.76248	5.604167	125.6152	5.604167	134.0236
5.8075	121.2008	5.8	56.94548	5.804167	126.0329	5.804167	135.0776
6.0075	121.8988	6	57.00912	6.004167	126.2194	6.004167	135.5187
6.2075	122.3831	6.2	57.18438	6.204167	126.5505	6.204167	135.7326
6.4075	123.1953	6.4	57.51446	6.404167	126.8163	6.404167	136.2637
6.6075	123.8404	6.6	57.83404	6.604167	126.9754	6.604167	136.828
6.8075	124.4447	6.8	58.11818	6.804167	127.2995	6.804167	137.3859
7.0075	125.2937	7	58.44314	7.004167	127.4308	7.004167	137.8952
7.2075	125.755	7.2	58.54182	7.204167	127.621	7.204167	138.3702
7.4075	126.2653	7.4	58.5346	7.404167	127.5988	7.404167	139.2974
7.6075	126.6527	7.6	58.48163	7.604167	127.5611	7.604167	139.4378
7.8075	126.9334	7.8	58.70476	7.804167	127.6857	7.804167	139.7905
8.0075	127.327	8	59.33764	8.004167	127.7781	8.004167	140.3879
8.2075	127.3059	8.2	59.75432	8.204167	128.0958	8.204167	140.4164
8.4075	127.598	8.4	59.81371	8.404167	128.5107	8.404167	140.8311
8.6075	128.1713	8.6	59.59075	8.604167	128.6651	8.604167	141.0699
8.8075	128.4339	8.8	59.39997	8.804167	128.6777	8.804167	141.4753
9.0075	129.2104	9	59.45351	9.004167	129.0363	9.004167	141.7719
9.2075	129.7839	9.2	59.66898	9.204167	128.7967	9.204167	142.2968
9.4075	130.6234	9.4	59.87579	9.404167	129.0505	9.404167	142.6585

Metal Foam @ 15.2 cm		Metal Foam @ 18.7 cm		Metal Fiber @ 15.2 cm		Metal Fiber 2 @ 15.2 cm	
Time	Heat Flux	Time	Heat Flux	Time	Heat Flux	Time	Heat Flux
[min]	[kW/m^2]	[min]	[kW/m^2]	[min]	[kW/m^2]	[min]	[kW/m^2]
9.6075	131.4583	9.6	60.15738	9.604167	129.5863	9.604167	142.7302
9.8075	131.8954	9.8	60.23496	9.804167	129.5106	9.804167	142.8027
10.0075	132.5044	10	60.35494	10.00417	129.7111	10.00417	142.642
11.0075	135.5611	11	61.03946	11.00417	129.5221	11.00417	143.1368
12.0075	138.7607	12	62.61579	12.00417	129.5502	12.00417	144.1414
13.0075	139.9004	13	62.38896	13.00417	130.2852	13.00417	145.6567
14.0075	143.8101	14	62.64293	14.00417	131.457	14.00417	147.2978
15.0075	144.121	15	62.07712	15.00417	129.9715	15.00417	146.1621
16.0075	144.7859	16	61.21876	16.00417	132.8217	16.00417	146.9755
17.0075	146.0869	17	60.29484	17.00417	132.8652	17.00417	148.4167
18.0075	147.3136	18	60.34513	18.00417	133.0675	18.00417	147.5815
19.0075	148.1626	19	60.06855	19.00417	133.2007	19.00417	148.7713
20.0075	148.8233	20	60.12311	20.00417	136.4684	19.62917	149.0076